DREAMS OF MOLECULAR BEAMS: INDIUM GALLIUM ARSENIDE TENSILE-STRAINED QUANTUM DOTS AND ADVANCES TOWARDS DYNAMIC QUANTUM DOTS (MOLECULARE RADIORUM SOMNIA: INDII GALLII ARSENICUS TENSA QUANTA PUNCTA ET AD DINAMICAE QUANTAE PUNCTAE PROGRESSUS)

by

Kevin Daniel Vallejo

A dissertation

submitted in partial fulfillment

of the requirements for the degree of

Doctor of Philosophy in Materials Science and Engineering

Boise State University

December 2021

© 2021
Kevin Daniel Vallejo
ALL RIGHTS RESERVED

BOISE STATE UNIVERSITY GRADUATE COLLEGE

DEFENSE COMMITTEE AND FINAL READING APPROVALS

of the dissertation submitted by

Kevin Daniel Vallejo

Dissertaiton Title: Dreams of Molecular Beams: InGaAs Tensile-Strained Quantum Dots and Advances towards Dynamic Quantum Dots (Moleculare Radiorum Somnia: Indii Gallii Arsenicus Tensa Quanta Puncta et ad Dinamicae Quantae Punctae Progressus)

Date of Final Oral Examination: 19 October 2021

The following individuals read and discussed the dissertation submitted by student Kevin Daniel Vallejo, and they evaluated the student's presentation and response to questions during the final oral examination. They found that the student passed the final oral examination.

Paul J. Simmonds Ph.D. — Chair, Supervisory Committee

Dmitri Tenne Ph.D. — Member, Supervisory Committee

Bernard Yurke Ph.D. — Member, Supervisory Committee

David Hurley Ph.D — Member, Supervisory Committee

The final reading approval of the dissertation was granted by Paul J. Simmonds Ph.D., Chair of the Supervisory Committee. The thesis was approved by the Graduate College.

DEDICATION

Dedicated to those who deserve the kingdom of photons.

ACKNOWLEDGMENT

First of all I want to acknowledge the Janos, Suma, Manso, Apache, Raramuri, Ysleta, Shoshone-Bannock, and Tepehuan peoples, whose sacred land was stolen, and who were themselves displaced and relegated from the different cities in which this work was carried out. The land is theirs and as their descendant I carry their memory in the work I do.

Secondly I want to acknowledge my family. Their relentless love, motivation, and cheers made it impossible to even consider quitting. Each and everyone of you is always in my mind. It is humbling to realize that from the beginning of this work to today, my great-grandmother Socorro, my grandmother Martha, my uncle Carlos, and a great number of people have left us to partake in the kingdom of photons. I assure you, we all feel your kind gaze as you guide us.

I acknowledge as well everything I was fortunate to share with those who stayed until love ran its course.

To my friends, I am blessed to have an long list of people that have tolerated my ramblings over the years. Be sure that even *in absentia* memories of our times together always flood my mind and motivate me to be the best version of myself.

The wonderful staff at Boise State University has shown me nothing but kindness, support, and genuine interest in the work I do. I appreciate all your work, especially the staff at the Physics department, the Micron School of Materials Science and

Engineering, the Graduate College, and the Health Services.

Lastly, all the faculty and network of collaborators that have taught me so much during these years. Dr. Keith Pannell gave me my first chance to be educated in a U.S. university through the recommendation of soon-to-be Dr. Miguel Veleta. Dr. Vivian Incera pushed me to finish all the coursework I needed to be a part of her high energy physics research group. And then Dr. Leobardo Bañuelos adopted me in his group as a brand new faculty member and showed me how to be a great experimentalist.

Closer to home, Dr. Christopher Schuck taught me by example what the definition of hard-work and determination is. Robin McCown gave me the first lessons in what it is to work in MBE. Dr. Katie Sautter showed me the importance of establishing a network of friends. Current and previous graduate students I have had the privilege to work with: Simon Roy has mastery of nature and control to learn new languages and make them work, Ariel Weltner is nothing but resilience and passion for work, Trent Garrett is drive to do your very best, and Maddy Drake is precision engineering like no one else I have ever met. Undergraduate students who have the invaluable gift of a world of possibilities have taught me how to keep my feet in the ground: Austin Mello was nothing but smiles in the middle of a work day, Ashley Hush showed me how to be excited about brand new results from a lab, Matthew Abramson is resilience in the face of adversity, Jorge Perez is dedication and love for new things, Patrick Eusepi is enjoyment and kindness in the midst of hard work, and Alessia Molino is a much needed ray of sunshine in a life that is constantly looking into the night.

Specially, I recognize the unending emotional labor that my friend, soon-to-be colleague, mentor, and advisor Dr. Paul Simmonds put into permitting me to apply my

energy in pursuing this work. I aim to provide future generations with the same inspiration of being a well rounded human being: academic, gentleman, family-oriented, and overall a great friend to be around.

In addition, I want to acknowledge all the wonderful people who have put their faith in me over the years. With school over, I can finally begin to pay you all back.

Also, I want to acknowledge the American Vacuum Society, MDPI, and American Institute for Physics Publishing for their permission to use my previously published research.

ABSTRACT

Through the operation of a molecular beam epitaxy (MBE) machine, I worked on developing the homoepitaxy of high quality InAs with a (111)A crystallographic orientation. By tuning substrate temperature, we obtained a transition from a 2D island growth mode to step-flow growth. Optimized MBE parameters (substrate temperature = 500 °C, growth rate = 0.12 ML/s and V/III ratio $\geqslant 40$) lead to growth of extremely smooth InAs(111)A films, free from hillocks and other 3D surface imperfections. We see a correlation between InAs surface smoothness and optical quality, as measured by photoluminescence spectroscopy. This work establishes InAs(111)A as a platform for future research into other materials from the 6.1 Å family of semiconductors grown with a (111) orientation.

Continuing this work, we also have determined a reproducible set of growth conditions for the self-assembly of tensile-strained $In_{1-x}Ga_xAs$ quantum dot nanostructures on InAs(111)A surfaces. During molecular beam epitaxy, $In_{1-x}Ga_xAs$ islands form spontaneously on InAs(111)A when the Ga content $x \geq 50$ %. We analyze the structure and composition of InGaAs/InAs(111) samples using atomic force microscopy, transmission electron microscopy, electron energy loss spectroscopy, and photoluminescence spectroscopy. We demonstrate control over the size and areal density of the islands as a function of $In_{1-x}Ga_xAs$ coverage, $In_{1-x}Ga_xAs$ composition, and substrate temperature.

Furthermore, we also present a study aimed to determining the growth conditions of $In_{1-x}Ga_xAs$ self-assembled tensile-strained QDs on GaSb(111)A surfaces. From previous work we determined that a larger band gap barrier was necessary to ensure the confinement of charge carriers in the InGaAs nanostructures. Through a series of temperature, V/III ratio, and growth rate we determined the best parameters for GaSb(111) homoepitaxy. We then studied the nucleation of optimal-morphology $In_{1-x}Ga_xAs$QDs by locking the compositions at $In_{0.5}Ga_{0.5}As$, studying the critical pause for group V element transition and V/III ratio prior and post QD growth. Several photoluminescence techniques are employed to determine the light emission properties of these structures.

Finally, we did preliminary studies on how to achieve the dynamic lateral confinement of charge carriers in 2D and 3D using near-THz surface acoustic phonon pulses in polar semiconductors. Using the acousto-electrical effect, we measure the degree to which surface acoustic waves (SAWs) confine electrons and holes limiting the number of recombination processes. Applications for this technological development include the external modulation of lateral confinement size in the SAWs and subsequent photon emission wavelength, as well as potential quantum logical gate design using acoustic pulses to drive electrons in a circuit.

TABLE OF CONTENTS

DEDICATION iv

ACKNOWLEDGMENT v

ABSTRACT viii

LIST OF FIGURES xv

LIST OF TABLES xxvi

1 INTRODUCTION 1

2 FUNDAMENTALS OF MOLECULAR BEAM EPITAXY 5

2.1 Physics of Molecular Beam Epitaxy 5

2.1.1 Experimental Setup 5

2.1.2 Thermodynamics 8

2.1.3 Kinetics 10

2.2 Physics of Semiconductors 12

2.2.1 Crystallography 12

2.2.2 Band Engineering 15

2.2.3 Quantum Effects 19

2.3 Growth of Solid-State Quantum Dots 21

2.4 Characterization Techniques 21
2.4.1 X-ray Diffraction 21
2.4.2 Atomic Force Microscopy 24
2.4.3 Transmission Electron Microscopy 25
2.4.4 Scanning Electron Microscopy 27
2.4.5 Photoluminescence 28
2.4.6 Raman Spectroscopy 31
2.4.7 Nomarski Imaging 31
2.4.8 Reflection High Energy Electron Diffraction 31
2.4.9 Residual Gas Analysis 32

3 DYNAMIC QUANTUM DOT GENERATION VIA SURFACE ACOUSTIC WAVES USING TRANSIENT GRATING SPECTROSCOPY 34
3.1 Introduction 34
3.2 Methods 36
3.2.1 Elastodynamics 37
3.2.2 Deformation Potential and Piezoelectricity 39
3.2.3 Transient Grating Spectroscopy 40
3.2.4 Sample Growth 42
3.3 Results and Discussion 44
3.3.1 X-ray diffraction 44
3.3.2 Raman spectroscopy 45
3.3.3 Photoluminescence 45
3.3.4 Transmission Electron Microscopy 46
3.4 Conclusions and Future Work 47

4 INDIUM ARSENIDE (111)A HOMOEPITAXY 49
4.1 Introduction 49
4.2 Methods 51
4.3 Results 53
4.3.1 Substrate Temperature Variation 53
4.3.2 Growth Rate Variation 55
4.3.3 V/III Ratio Variation 55
4.3.4 Summary of growth conditions 60
4.4 Conclusions 60

5 TENSILE-STRAINED SELF-ASSEMBLY OF INDIUM GALLIUM ARSENIDE ON INDIUM ARSENIDE (111)A 61
5.1 Methods 64
5.2 Results and Discussion 65
5.2.1 $In_{0.5}Ga_{0.5}As$/InAs(111)A coverage series 67
5.2.2 $In_{1-x}Ga_xAs$/InAs(111)A composition series 68
5.2.3 $In_{0.5}Ga_{0.5}As$/InAs(111)A substrate temperature series 69
5.2.4 Transmission Electron Microscopy of $In_{0.5}Ga_{0.5}As$ 70
5.2.5 Electronic structure of $In_{1-x}Ga_xAs$/InAs(111)A QDs 72
5.3 Conclusions 74

6 TENSILE-STRAINED INDIUM GALLIUM ARSENIDE QUANTUM DOTS ON GALLIUM ANTIMONIDE (111)A 81
6.1 Introduction 81
6.2 Methods 84

6.3 Results and Discussion 85
6.3.1 GaSb Homoepitaxy 85
6.3.2 $In_{1-x}Ga_xAs$ Quantum Dots 86
6.4 Conclusions 94
7 COLLABORATIONS AND FUTURE WORK 97
7.1 Collaboration Efforts 97
7.1.1 Tensile-Strained Quantum Dots on InAlAs 97
7.1.2 Review of Self-Assembled Quantum Dots via MBE 98
7.1.3 Superconduction of Al on InAs(111) Quantum Well 98
7.1.4 Influence of the arsenic flux on the performance of infrared photodetectors based on InAs submonolayer quantum dots 100
7.1.5 Interfacial structure and luminescence properties of epitaxial PbSe films on (111)A InAs 101
7.2 Future Work 102
REFERENCES 104
APPENDICES 121
A DERIVATIONS AND PROGRAMMING CODE 122
A.1 Phonon Dispersion Relation Derivation 123
A.2 Surface Acoustic Wave Theory 126
A.3 Energy Quantization in Quantum Wells 132
A.3.1 Energy Levels in Quantum Dots 139
A.3.2 Computational QD Energy Levels Calculation 140

A.4 Piezoelectric Tensor 142

A.5 Quantum Well Energy Calculation Code 144

A.6 XRD Simulation and Fitting Code 147

A.6.1 Code for XRD simulation 147

A.6.2 Code for Scaling and Plotting Data 148

LIST OF FIGURES

2.1 Schematic of MBE chambers and external vacuum devices. Inset shows incidence of beams on substrate. 7

2.2 Phase diagram of GaAs. Reproduced with permission from [1] 8

2.3 Phase diagram of GaSb. Reproduced from [2] 9

2.4 Kinetic processes present during the nucleation and growth of 2D thin films via (a) layer-by-layer growth and (b) step-flow growth. Different growth modes during MBE growth resulting from a thermodynamic interaction of surface energies: (c) the FM layer-by-layer growth mode, (d) the Volmer–Weber (VW) growth mode, which produces 3D islands directly on a substrate; and (e) the SK growth mode in which 3D islands form on top of a complete 2D wetting layer. 10

2.5 Schematics of crystallogrphic characteristics of the zincblende structure. (a) atomic arrangement of a unit cell (b) location of planes in a cubic unit cell (c) planes and axes of symmetry with their corresponding symbols and symmetries on the group $F\bar{4}3m$ stereograph (d) . . . 13

2.6 Schematics of electronic bands and their types. (a) depicts the different types of band gaps in materials. (b) different between direct and indirect band gap. (c) types of band gap alignments. 16

2.7 Band gap vs. lattice constant diagram for semiconductors. Adapted from Ref. [3] 18
2.8 (a) Schematic of energy level quantization in a quantum well. The dashed lines correspond to the energy levels, while the blue solid lines correspond to the wavefunctions of each level. (b) schematic of a quantum well (c) Schematic of a quantum wire, and (d) schematic of a quantum dot. 20
2.9 (a) Schematic of reflection of x-rays off a series of atomic planes. (b) Schematic of XRD setup with associated scanning angles. 22
2.10 (a) Schematic of surface analysis using in an AFM setup. (b) Profile of a scan used to generate surface topology data. 24
2.11 (a) Schematic of a transmission electron microscopy setup. The electron beam is aligned through a series of magnetic lenses before and after interacting with the sample. (b) Schematic of layers used to mechanically fabricate a TEM sample, (c) shows the geometry of integrated sample layers in a copper tube, before being sliced into a sample as shown in (d). 26
2.12 Schematic of a scanning tunneling microscopy setup. An electron beam is aligned through a series of magnetic lenses before hitting the sample, where data is acquired through a series of detectors for backscattered electrons, secondary electrons, and x-rays. 28

2.13 (a) Schematic of a photoluminescence setup. The laser beam used to stimulate the sample electrons goes through a series of lenses and mirrors to focus and align the correct geometry for the beam, after which emitted light is directed towards a detector. (b) PL spectra of a GaAs/AlGaAs multiple quantum well (details provided in chapter 3). 30
2.14 Plot of the RHEED intensity pattern 32
2.15 Plot of an RGA signal analysis. The x-axis represents the weight of the atoms detected, while the y-axis is a logarithmic scale of the pressure for each value. 33

3.1 Schematic of charge carrier trapping in potential wave generated by a SAW in a piezoelectric semiconductor. 36
3.2 Schematic of a transient grating spectroscopy laser splitting setup. Using two lasers of different wavelengths the excitation of the carriers and the SAW train can be generated and measured within the same region. 42
3.3 Schematic of the multiple quantum well structure used for this study. Gray sections correspond to GaAs and white sections to AlGaAs. The $Al_{0.3}Ga_{0.7}As$ composition is determined using RIOs, XRD, and Raman spectroscopy. 43
3.4 XRD pattern of a $Al_{0.3}Ga_{0.7}As$ MQW. 44
3.5 Spectrum of a Raman spectroscopy study of the same GaAs/AlGaAs MQW. We used a 532 nm laser to measure the sample at 8 K. The position of each peak is determined by the composition of the alloy, and measuring the peak's center provides us with a measurement of Al content. 45

3.6 Photoluminescence spectrum of the multiple quantum well structure used in this study. The sample was measured at 7 K and measured with a 532 nm laser wavelength. 46

3.7 Plot of emission wavelength from the MQW sample calculated from expected values (green), calculated from measured well thickness in TEM (blue) and experimental values taken from PL (red). 47

3.8 (Color online) Transmission electron micrograph of the multiple quantum well structure. 48

4.1 (a)-(f) 1μm × 1μm AFM micrographs showing the effect of T_{sub} on InAs(111)A surface morphology. Height for (a)-(c) is 3 nm while for (d)-(f) it is 1 nm. All samples were grown at 0.12 ML/s, with a V/III ratio of 24. A dramatic decrease in R_q surface roughness above T_{sub} = 440 °C, is accompanied by a transition from island growth to step-flow growth. (g) InAs(111)A PL spectra as a function of T_{sub}. PL is brighter for samples grown at higher temperature, consistent with improved material quality. (h) Triangles show R_q (over a 1 μm^2 area) as a function of T_{sub}, with roughness minimized at 470–500 °C. Squares show the integrated intensity of the PL spectrum for each T_{sub} sample. We see a sharp increase in light emission intensity above T_{sub} = 410 °C. 54

4.2 (Color online) (a)-(c) AFM micrographs showing the effect of InAs(111)A growth rate on surface morphology. All samples were grown at 500 °C, with a V/III ratio of 24. Large figures are 5×5 μm^2 scans with a height of 3 nm, with insets of 1×1 μm^2 and height of 1 nm. (d) InAs(111)A PL spectra as a function of sample growth rate. These spectra are similar in intensity, indicating that InAs(111)A optical quality is only weakly dependent on growth rate. (e) Triangles show R_q (over a 1 μm^2 area) as a function of InAs(111)A growth rate, with the lowest roughness occurring at 0.12 ML/s. Squares show the integrated intensity of the PL spectrum for each growth rate. PL intensity decreases at the highest growth rate, and the surface becomes rougher. 56

4.3 5×5 μm^2 AFM micrographs showing the effect of V/III ratio on surface morphology. All samples were grown at 500 °C, with a growth rate of 0.12 ML/s. Large images have a height of 6 nm, with insets of 1×1 μm^2 and height of 1 nm. For V/III $\geqslant 12$, we see smooth InAs(111)A surfaces and the formation of regularly spaced terraces aligned perpendicular to the $[\bar{1}10]$ direction. (d) InAs(111)A PL spectra as a function of V/III ratio. The spectra are reasonably close in intensity, indicating limited dependence of V/III ratio on InAs(111)A optical quality. (e) Triangles show R_q (over a 1 μm^2 area) as a function of V/III ratio, showing that ratios above 24 result in the smoothest film growth. Squares show the integrated intensity of the PL spectrum for each V/III ratio sample. Although there is a small downward trend with increased V/III ratio, the magnitude of the change is almost within the measurement error. 58

4.4 (Color online) Contour plots of R_q roughness as function of (a) growth rate and T_{sub}, (b) V/III ratio and T_{sub}. Contour plots of integrated PL intensity as function of (c) growth rate and T_{sub}, and (d) V/III ratio and T_{sub}. Deeper color hues indicate improved material parameters: darker magenta and blue indicate smoother surface and higher PL intensity, respectively. 59

5.1 500 nm × 500 nm AFM micrographs showing the evolution of surface morphology after deposition of 2 − 4 ML $In_{1-x}Ga_xAs$, with Ga concentrations of $x = 0.25, 0.5, 0.75$ and 1.0. We grew all samples at $T_{sub} = 410$ °C. The z-scale is 3 nm for all images. The dashed outline highlights the ML coverage series for $In_{0.5}Ga_{0.5}As$ (Sec. 5.2.1). The solid outline highlights the $In_{1-x}Ga_xAs$ composition series for 3 ML coverage (Sec. 5.2.2). 66

5.2 1 μm × 1 μm AFM micrographs showing the evolution of surface morphology after deposition of (a) 2 ML, (b) 3 ML, and (c) 4 ML $In_{0.5}Ga_{0.5}As$. All samples were grown at $T_{sub} = 410$ °C. The z-scale is 3 nm for all images. 75

5.3 (a)-(d) 500 nm × 500 nm AFM micrographs showing the effect of Ga content on the morphology of 3 ML $In_{1-x}Ga_xAs$/InAs(111)A. (a) For $x = 0.25$, the InGaAs forms a smooth 2D layer with formation of only occasional QDs. (b) Self-assembled QDs appear for $x \geq 0.50$. As the Ga concentration is increased to (c) $x = 0.75$, and (d) $x = 1.00$, we see QD size and density increase. (e) Areal density of $In_{1-x}Ga_xAs$/InAs(111)A QDs as a function of x. (f) Average QD height (left axis) and diameter (right axis) against x. All samples grown at $T_{sub} = 410$ °C, from a coverage of 3 ML InGaAs. The z-scale for AFM images (a)-(c) is 2 nm, and 5 nm for (d) for clarity. The z-scale for AFM images is 4 nm 76

5.4 500 nm × 500 nm AFM micrographs showing how the morphology of 3 ML $In_{0.5}Ga_{0.5}As$/InAs(111)A changes as T_{sub} is increased: (a) 410 °C, (b) 440 °C, (c) 470 °C, and (d) 500 °C. QD size increases as we raise T_{sub}, accompanied by a decrease in QD areal density. (e) Areal density of 3 ML $In_{0.5}Ga_{0.5}As$/InAs(111)A QDs versus T_{sub}. (f) Graph of average QD height (left axis) and diameter (right axis) versus T_{sub}. 77

5.5 Cross-sectional TEM image montages taken at low magnification of $In_{0.5}Ga_{0.5}As$/InAs(111)A samples containing (a) 3 ML and (b) 4 ML InGaAs layers. In (a) we can resolve two distinct strained regions: at the interface between the substrate and the homoepitaxial InAs(111)A, and in the 3 ML InGaAs QD layer. In (b) we see the same features, but the contrast for the $In_{0.5}Ga_{0.5}As$ layer is enhanced due to the larger 4 ML QDs in this sample. In addition, dislocations in the InAs cap indicate tensile strain relaxation in these larger 4 ML InGaAs QDs. . 78

5.6 Cross-sectional TEM characterization of capped QD samples grown at 410 °C and containing (a)−(c) 3 ML or (d)−(f) 4 ML $In_{0.5}Ga_{0.5}As$. BF STEM images of the (a) 3 ML and (d) 4 ML InGaAs QD layers, and corresponding Ga L-edge EELS maps taken from the boxed areas for 3 ML (c) and 4 ML (f). High-resolution TEM images of (b) 3 ML and (e) 4 ML InGaAs QDs from the same area as the EELS maps in (a) and (c), respectively. For ease of comparison, we have numbered corresponding QD locations in the EELS maps and high-resolution TEM images. 79

5.7 Simulation of the bulk band gap of $In_{1-x}Ga_xAs$ (black curves) under biaxial tensile strain on InAs(111)A substrates. The darker orange color signifies the experimentally derived thickness of the 2D wetting layer, showing its reduction with increasing strain. For samples with $x \geq 0.5$, the lighter yellow color represents the average QD height measured with AFM. The red lines show the electron ground states for the wetting layer (solid line) and QDs (dashed line), calculated by solving the Schrödinger equation in the effective mass approximation. 80

6.1 5 μm x 5μm AFM micrographs showing the evolution of the surface quality of GaSb with varying quantities of Sb overpressure. The images have a vertical scale of 6 nm. We grew (a) at 1.5x10^{-6} Torr BEP and several large "wedding cake" structures are visible, the structures are significantly flattened in (b) which we grew at 1.9x10^{-9} Torr. (c) shows a large structure with step-flow growth product of its 2.5×10^{-6} Torr BEP Sb overpressure, and finally (d) shows large terraces of 500 nm, which we grew at 3.1x10^{-6} Torr. Inset is a 1 μm x 1 μm section with a vertical scale of 1 nm. (e) shows the relationship between Rq and Sb overpressure where we obtained a significant improvement of the surface by increasing the V/III ratio. 87

6.2 Sample growth structure. Buried QD layer is used for PL studies, while the top layer is used for AFM characterization. 88

6.3 RHEED patterns obtained during the various stages of growth of buffer, QD layer, capping layer, and top QD layer. 89

6.4 (a) Shutter sequence during growth of samples. (b) Relation between GaSb capping layer surface reconstruction time as a function of InGaAs deposition amount, and As-to-Sb time pause during growth. 90

6.5 (a)-(f) 1 μm x 1 μm AFM scans of $In_{1-x}Ga_xAs$QDs grown at 420 °C (640 °C on our thermocouple) at 0.1 ML/s. The pause between group V switch was 0 seconds (no pause). (g) Photoluminescence spectra obtained from samples with 0.7 to 2.5 ML using an InGaAs detector. The three emission peaks are identified with their corresponding transitions in the GaSb buffer layer. 91

6.6 (a)-(c) 1 μm x 1 μm AFM scans of $In_{1-x}Ga_xAs$QDs grown at 450 °C (670 °C on our thermocouple) at 0.4 ML/s. The pause between group V switch was 10 seconds. (d) Shows the density of these TSQDs as a function of deposition amount. (e) Plot of diameter and height of TSQDs as a function of deposition amount. 94

6.7 Transmission electron microscopy images of an $In_{0.5}Ga_{0.5}As$ QD layer, 3 ML in thickness buried under 75 nm of GaSb. (a) shows the strain to be focused to the $In_{0.5}Ga_{0.5}As$ layer with no directly visible defects forming. (b) Shows a series of individual QDs evidenced by the strain contrast. (c) Closer images of two differently sized QDs. (d) Single QD seen with atomic resolution, and (e) shows the atomic arrangement in the QD. 95

6.8 Schematic of band alignment in the InGaAs/GaSb TSQD system with biaxial strain. It is notable that at all concentrations this system exhibits a type III band alignment. 96

7.1 SEM of the surface of an Al epilayer deposited on InAs(111) grown homoepitaxially on InAs(111)A. 99
7.2 Schematic of sub-monolayer quantum dot superlattice structure for infrared photodetectors. The active region is marked as the substructure that repeats six times. 100
7.3 (a) Photoluminescence spectra of the different SMLQDIP samples. (b) Plot of the specific detectivity of the samples. The samples are A (2 $\times$ 4 with low As), B (c(4 $\times$4 with low As), and C (c(4 $\times$4 with high As) grown with different surface reconstructions prior to the SMLQDs deposition. 101
7.4 PbSe/InAs interfacial structures: High-resolution HAADF-STEM cross sections of two PbSe/InAs interfaces with proposed structures. 102

LIST OF TABLES

2.1 Lattice Constant for III-V Semiconductors used in this study at 300 K. 14

2.2 Spectral Detection Range for PL Detectors 29

6.1 Light emission studies of InGaAs on GaSb 83

6.2 GaSb PL Peaks 92

A.1 Effective masses used for calculation of energy levels, from Nakwaski[4] 138

LIST OF PUBLICATIONS

Main authored publications

1. Vallejo, Kevin D., Trent A. Garrett, Kathryn E. Sautter, Kevin Saythavy, Baolai Liang, and Paul J. Simmonds. "InAs (111) A homoepitaxy with molecular beam epitaxy." Journal of Vacuum Science & Technology B, Nanotechnology and Microelectronics: Materials, Processing, Measurement, and Phenomena 37, no. 6 (2019): 061810.

2. Vallejo, Kevin D., Trent A. Garrett, Carlos I. Cabrera, Baolai Liang, Kevin G. Grossklaus, and Paul J. Simmonds. "Tensile-strained self-assembly of InGaAs on InAs(111)A" Journal of Vacuum Science & Technology B, Nanotechnology and Microelectronics: Materials, Processing, Measurement, and Phenomena, (2021): *In review*

3. Vallejo, Kevin D., Trent A. Garrett, Carlos I. Cabrera, Madison D. Drake, Baolai Liang, Kevin G. Grossklaus, and Paul J. Simmonds. "Tensile-strained self-assembly of InGaAs Quantum Dots on GaSb(111)A" *In Preparation*

Reviews and Tutorials

1. Vallejo, Kevin D., Kathryn E. Sautter, and Paul J. Simmonds. "Strain-driven quantum dot self-assembly by molecular beam epitaxy." Journal of Applied

Physics 128, no. 3 (2020): 031101.

Collaboration Publications

1. Sautter, Kathryn E., Christopher F. Schuck, Trent A. Garrett, Ariel E. Weltner, Kevin D. Vallejo, Dingkun Ren, Baolai Liang, Kevin A. Grossklaus, Thomas E. Vandervelde, and Paul J. Simmonds. “Self-assembly of tensile-strained Ge quantum dots on InAlAs (111) A.” Journal of Crystal Growth 533 (2020): 125468.

2. Haidet, Brian B., Leland Nordin, Aaron J. Muhowski, Kevin D. Vallejo, Eamonn T. Hughes, Jarod Meyer, Paul J. Simmonds, Daniel Wasserman, and Kunal Mukherjee. “Interface structure and luminescence properties of epitaxial PbSe films on InAs (111) A.” Journal of Vacuum Science & Technology A: Vacuum, Surfaces, and Films 39, no. 2 (2021): 023404.

3. Schuck, Christopher F., Kevin D. Vallejo, Trent Garrett, Qing Yuan, Ying Wang, Baolai Liang, and Paul J. Simmonds. “Impact of arsenic species on self-assembly of triangular and hexagonal tensile-strained GaAs (111) A quantum dots.” Semiconductor Science and Technology 35, no. 10 (2020): 105001.

4. Sautter, Kathryn E., Christopher F. Schuck, Justin C. Smith, Kevin D. Vallejo, Trent A. Garrett, Jake Soares, Hunter J. Coleman et al. “Self-Assembly of Ge and GaAs Quantum Dots under Tensile Strain on InAlAs (111) A.” Crystal Growth & Design 21, no. 3 (2021): 1674-1682.

5. Alzeidan, Ahmad, Tiago F. Cantalice; Kevin D. Vallejo; Raja S.R. Gajjela; Arthur L. Hendriks; Paul J. Simmonds; Paul M. Koenraad; Alain A. Quivy

“Effect of As flux on InAs submonolayer quantum dot formation for infrared photodetectors.” Sensors and Actuators A: Physical, (2021) *In review.*

CHAPTER 1:
INTRODUCTION

Physics is the study of the world and everything in it. It can show us a meaningful representation of what our senses are able to perceive and our minds to interpret. It is also a noble endeavor few are privileged enough to adventure into. By trying to answer questions that a five year old child would be proud of, I joined a research team looking to participate in the creation of self-assembled nanostructures with single-photon emitting capabilities for photonics applications. In this introduction I will try to bridge the gap between this particular scientific endeavor and the very old questions of what is real, where do we come from, what is stuff made of, and what is out there.

Reality is often a compromise between three things: what we are ready to accept, what we perceive, and the way things really are. Through the exercise of science we aim to increase the agreement between these three areas in two complementary ways: by finding out the way things really are, and training our perception and reason to accept them. We do so by separating our understanding and reasoning from the everyday common sense that helps us survive as biological entities.

If and when we decide to engage with these questions seriously, we stand on the shore of the self and the other. We have the option to look inward (a journey maturity requires) or start our contemplation of the external world. Let us focus temporarily

on this second option, and we now have a new decision to make. The world in time and space extends in scales that greatly challenge not only our human perception but our understanding. Different realms of physics focus their effort on the different combinations of scales available. I believe it is fair to say many of us first get attracted to the study of physics through space (where time is measured in millions of years and space in billions of kilometers), the focus of this dissertation will be the very small spatial scales (in the order of a few atomic lengths) and timescales that range from millionths of a second to a few hours.

What happens at these specific scales and why this work focuses on them begs the question of why leave so much outside. First of all, because so much work has been done trying to understand the dance of atoms and their bonds, that it is necessary to focus the scope even further to a specific set of elements and their properties. Gallium (Ga), aluminum (Al), indium (In), arsenic (As), and antimony (Sb) are three metals and two semi-metals that when combined precisely can form an energetic landscape which reveals the quantum nature of their charge carriers.

The structure and reality of atoms is a non-trivial subject. It is not only an issue that armchair philosophers discuss in the basement of the ivory tower, but it is a rather important aspect of pedagogical importance [5]. In the spatial scales at which I carry out this study we can take a pragmatic approach and consider an entity-based ontology where atoms and electrons have an axiomatic reality. In plain words, we will follow the easy path of considering these particles as taught in current science curricula and not worry about their true nature.

Future studies I consider worth pursuing will no longer take this approach, and process-related ontologies, isotope-based epitaxy, and social aspects of the MBE com-

munity as a scientific community are addressed in chapter 7.

With all this in mind, I can now provide the motivation as to why the focus of this work is on this particular set of atoms and growth modes. The human scale technology that has facilitated computation (itself providing us a higher quality of life and comfort) currently relies on us taking advantage of the information processing abilities of semiconductor devices. Although most of the big multinational companies dealing with semiconductors are focused on silicon (Si) and germanium (Ge) this work focuses on the more expensive materials described above because of the advantages provided by their physical properties (discussed in detail in the following chapters).

Naturally occurring atoms, primordial constituents of matter that participate of the same chemical properties, have an electronic structure that dictates the color of light they can emit. Aggregates of these atoms can provide a geometry suitable for new, custom-made energy levels from which we can extract light. In contrast to chemical approaches, where several steps and large compounds in strict configurations are required to obtain certain light wavelengths, creating quantum dots in a solid state environment is comparatively fast and simple to implement.

Former members of my research team selected specific combinations of elements to create these quantum dots: GaAs on InAlAs, and not very differently Ge on InAlAs. In order to increase the pool of available QDs (and by extension, the palette of colors available for light emission) I focus this study on InGaAs grown on InAs and GaSb. This combination allows for a larger selection of band gap differences to study detailed physics on light emission and the effects of strain.

Where does the strain come into play, then? Energy conservation induces all differences in potentials to reduce to a minimum. This is the case with electromagnetic

forces contained in atoms. Water droplets that accumulate on a repelling surface (like a newly waxed car, or certain tree leaves) will form small lens-like structures. The same principles apply for small quantities of certain semiconductors on crystalline surfaces. The difference in the equilibrium distance between atoms for different materials produces the formation of droplets, whose geometry depends of various factors explored later in this work.

In chapter 2 I guide the reader through the physics, technology, and nuances of the techniques used throughout this work, with emphasis on molecular beam epitaxy. In addition, I provide a quick summary of the main mechanisms for each characterization technique I have used during this work.

In chapter 3 I will explain the initial hypothesis and findings of the project in which we tried to create dynamic quantum dots using mechanical waves on semiconductors. In chapter 4 I will explain the journey by which we established a reliable and reproducible recipe on how to grow InAs on top of more InAs oriented in the (111) crystallographic direction. In chapter 5 I will explain our attempt to create self-assembled islands (which we expected to turn into quantum dots) on the InAs(111) layer we developed in the previous chapter. In chapter 6 I will explain our journey to crown this work by creating InGaAs self-assembled QDs of different compositions on GaSb barriers in the (111) crystallographic orientation.

In chapter 7 I contribute some concluding remarks, including future work and potential follow-up projects for this dissertation, and how some of it has already provided collaborators around the continent with material for new projects.

CHAPTER 2: FUNDAMENTALS OF MOLECULAR BEAM EPITAXY

2.1 Physics of Molecular Beam Epitaxy

Molecular beam epitaxy is the state-of-the-art technique for the growth of high quality semiconductor, metallic, and compound thin film materials. In essence, MBE consists of the interaction of one or more molecular beams (hence the name) with a crystalline substrate in ultra-high vacuum conditions [6]. Four main factors determined the success of MBE over the past 51 years: understanding of surface morphology, substrate preparation, versatility of the experimental setup, and vacuum conditions. I will discuss the first two in the next couple subsections since they rely heavily on an understanding of thermodynamics and crystal growth kinetics.

2.1.1 Experimental Setup

The versatility of the experimental MBE setup comes from the minimum (if at all necessary) changes required to grow different types of semiconductors: there are elemental semiconductors (Si and Ge), and compound semiconductors made of elements located on different groups of the periodic table such as III-V (GaAs), II-VI (ZnO), and IV-VI (PbSe). Generally, an MBE setup consists of two to three stainless steel

vacuum chambers with increasing vacuum levels. These are achieved by a system of pumps fitted to each individual chamber needs. Substrate surfaces can be chemically treated (for example Si wafer requiring HF etching prior to growth) or simply placed on a substrate heater mounted inside the main chamber to remove impurities, moisture, and the protective native oxide layer from the surface. Very high purity (99.99999%, or 7N) elements are placed inside effusion cells, which essentially are small ovens from where the elements are vaporized or sublimated in order to direct the beam of atoms or molecules towards the very clean substrate surface. In the case of nitride or oxide materials, these efussion cells are replaced with plasma sources for oxygen and nitrogen. Also, refractory metals that need very high temperatures to produce large enough quantities of materials for growth usually require an electron beam source, which instead of heating the whole container to produce the beam, it rasters a high energy electron beam on the surface of the material in order to locally heat and produce a molecular beam.

The vacuum conditions for most MBE setups are quite similar, with the main difference being the pressures required inside the growth chamber that depends on the type of sources used. Plasma sources typically raise the pressure of the growth chamber to levels in the 10^{-6} Torr, which makes the pump requirements for this chamber to be different from those which only use solid sources. Extra care is required with oxide-based chamber, as the O plasma can cause various components to burn out rapidly due to its high reactivity. The load-lock chamber is where we introduce the clean substrates into the vacuum system. This chamber is pumped down from atmospheric pressure down to levels on 10^{-6} Torr using a scroll pump (which avoids the use of oil potentially contaminating the system) coupled to a turbomolecular

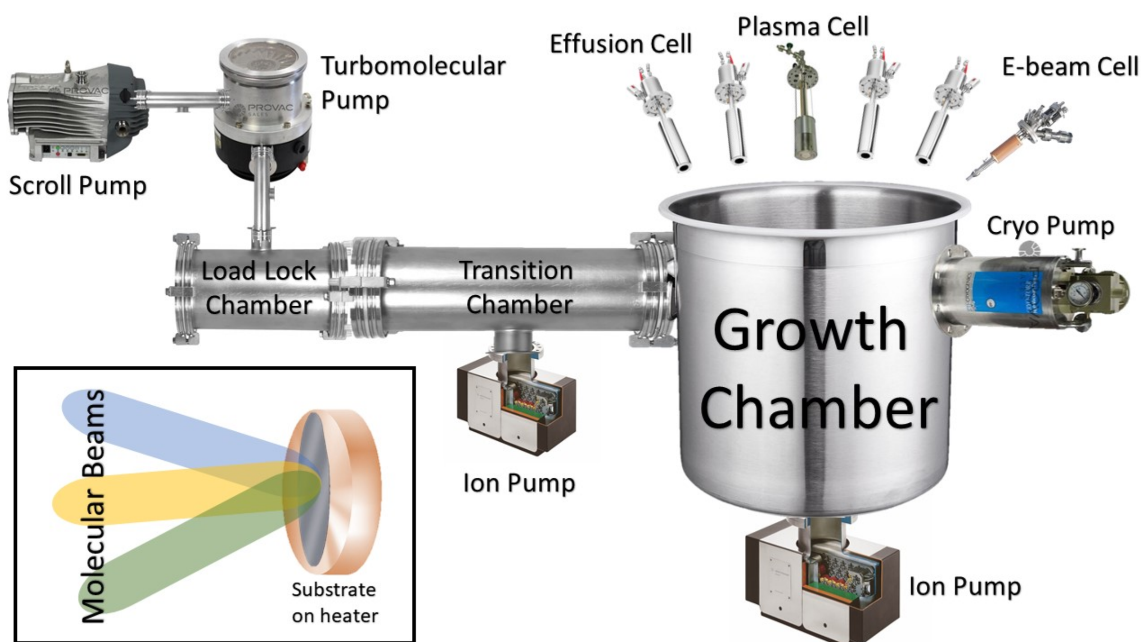

Figure 2.1: Schematic of MBE chambers and external vacuum devices. Inset shows incidence of beams on substrate.

pump. Together they provide the vacuum level required to pump down further to 10^{-8} Torr using an ion pump. Once at this level, the substrates can be moved to the transition chamber, where they remain in ultra-high vacuum conditions (10^{-9} Torr) until growth occurs. Because the process to reduce the pressure in the load-lock chamber takes between 5 and 8 hours, several substrates are loaded at once. The day an actual growth is scheduled to happen, 60 gallons of liquid nitrogen (LN2) are made to flow through a vacuum jacket installed in the growth chamber in order to cryogenically capture any particles floating inside the chamber, further reducing the background pressure. We measure the presence of certain gases inside the chamber using a residual gas analyzer (RGA) and monitor the surface morphology during growth using reflection high energy electron diffraction (RHEED) both of which I will discuss in further detail below.

Using a system of magnetic manipulation devices, we can transport the substrate from the trolley in which they are kept under vacuum to the actual growth chamber, to be placed in the substrate heater where growth will occur. Once here, a system of high pressure air lines (located entirely outside of the vacuum system) controls the shutters that allow or interrupt the flow of molecules from the effusion cells. All heating elements in the system are controlled using power supplies connected to PID controllers, which regulate the power output based on the derivative, absement, and thermocouple reading on each heating filament. Once the substrate is mounted on the heater, thermo-kinetic processes on the surface of the sample begin to occur that allow the desorption of oxide layers provided to protect the substrate during transport, and the growth of material itself. I will discuss these process in the following two subsections.

2.1.2 Thermodynamics

As pointed out by Tsao MBE can be thermodynamically characterized as an exceedingly precise phase transformation from vapor to a solid phase [1]. The physically inclined will then ask themself what are the driving forces for this phase transformation, and why does it happening in an MBE system make it so special? A consequence of the second law of thermodynamics states that in order for a system to never have a decrease

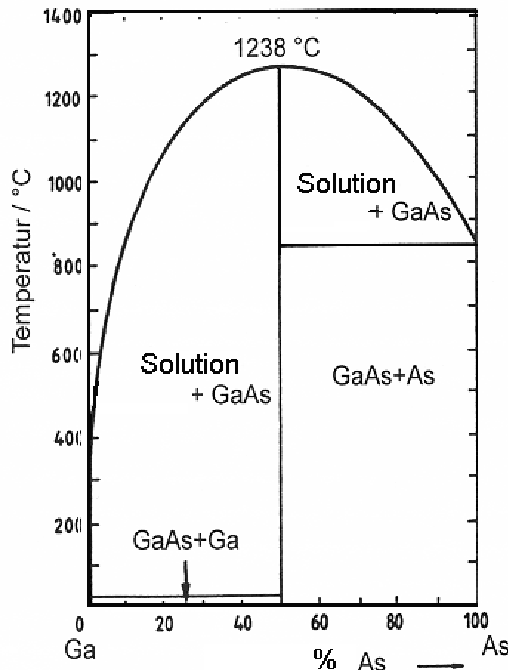

Figure 2.2: Phase diagram of GaAs. Reproduced with permission from [1]

in irreversible entropy (and thus, prevent it from minimizing its total internal energy) processes must advance towards a state in which entropy increases in lieu of a loss of energy between the system and its environment.

For a binary solid solution such as a III-V semiconductor material (the main materials for the present study) there are 6 potential phases present in the growth chamber taking as an example GaAs: Ga_{solid}, Ga_{vapor}, As_{solid}, As_{vapor}, GaAs_{solid}, GaAs_{vapor}. The phase diagram and Gibbs free energy diagram illustrated in Fig. 2.2 show these different phases at a pressure of 10^{-9} Torr and 850 K. There is a very precise "region" where GaAs can grow without aggregates of either Ga or As.

This is exactly at a 50% concentration of both elements. Taking into account experimental values for the heat capacity parameters of the condensed phases, and the translational, vibrational, and rotational heat capacity parameters for the vapor phases we can explain this by noting that Ga is the limiting factor in the growth process. As will be adsorbed and desorbed at roughly the same rate from the surface of the crystal unless it encounters sites in which to bind with Ga [1]. A similar story unfolds for our materials of interest InAs and GaSb. Fig. 2.3 shows the phase diagram of GaSb, where again Ga is the limiting factor for growth, and we only have a narrow "region" for growth without either Ga or Sb aggregates.

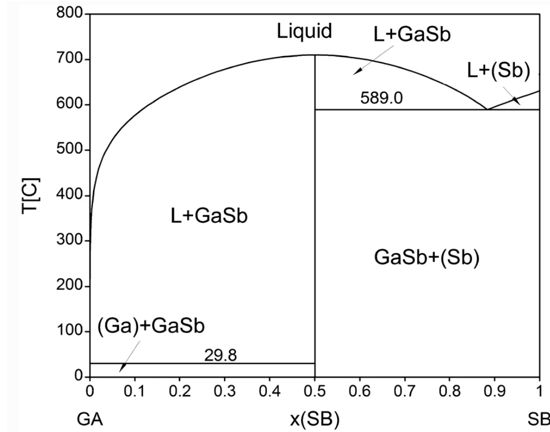

Figure 2.3: Phase diagram of GaSb. Reproduced from [2]

2.1.3 Kinetics

The kinetics of MBE mainly deal with the way layers grow and atoms impinge on the surface, physisorb, chemisorb, or desorb in the process of new layer formation.

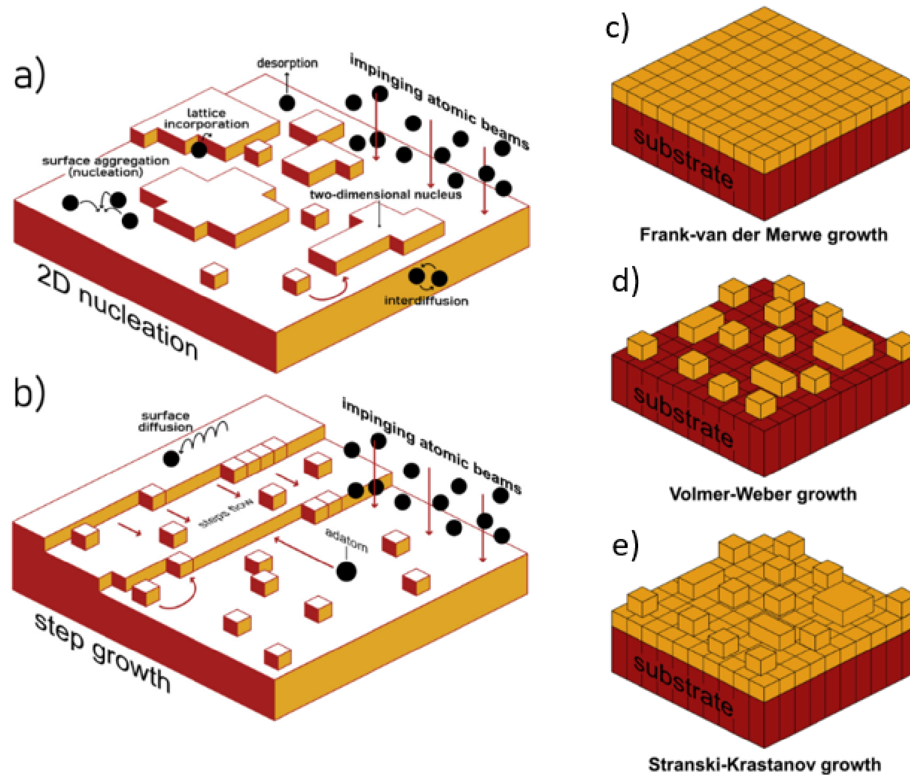

Figure 2.4: Kinetic processes present during the nucleation and growth of 2D thin films via (a) layer-by-layer growth and (b) step-flow growth. Different growth modes during MBE growth resulting from a thermodynamic interaction of surface energies: (c) the FM layer-by-layer growth mode, (d) the Volmer–Weber (VW) growth mode, which produces 3D islands directly on a substrate; and (e) the SK growth mode in which 3D islands form on top of a complete 2D wetting layer.

Figure 2.4 shows these processes as they unfold during growth. Impinging atoms can either be physisorbed onto the surface where they can still travel until they fall into an energetically favorable site and they become chemisorbed to be part of the

growing layer. The process by which these layers form can take different forms that depend on the chemistry of the atoms and the surface. Imagining a Kossel crystal (i.e. a surface that has not reconstructed and has dangling bonds on it [7]) the atoms can aggregate to form islands, incorporate into already formed islands, interdiffuse, or desorb (Fig. 2.4a). We call this 2D nucleation. When we instead observe a growth of different layers forming at the same time and a kind of "cascading" growth we have a step growth and adatoms (atoms that have already physisorbed but not chemisorbed) incorporate to these growing layers (Fig. 2.4b). Depending on the free energies and contact angles of the forming islands, we can then have three distinct growth modes: the Frank-van der Merwe (FM) where flat layers grow, Volmer-Weber growth where islands form and are stable on the surface, and finally the Stranski-Krastanov mode (SK), where after a critical thickness of layer growth, 3D islands form on top of it (Fig. 2.4c-e).

There are some mechanical considerations that are important to consider with respect to the epitaxial growth of these materials. As we will see below in section 2.2.2 the strain, lattice constant, and defect density of a material are intrinsically tied to their optical and electronic properties, which in turn affect and are affected by its kinetics and thermodynamics. In order to provide a pedagogically active description of the physics behind this project, I have separated this aspects in different sections, but let the reader be aware of the close ties between them. After all, the system is one and the physics are all the same, it is only our limited understanding and affinity for classification that requires this partition to occur.

2.2 Physics of Semiconductors

In addition to the study of physics and kinetics that occurs within the experimental setup of MBE, there is a wealth of phenomena that unfolds within the semiconductor crystals themselves once they have been removed from the UHV environment that characterizes MBE. Besides typical corrosion processes such as oxidation, cleavage, and dusting, we can manipulate the sample to exploit and study the properties that ideally motivated its growth.

2.2.1 Crystallography

Solid materials can be separated and classified in many different ways. The advent of atomic theory and microscopy has allowed us to look deep into their internal structure and classify them according to the way their atoms arrange. From this point of view, we can visualize an abstract mathematical entity: a crystal. This concept defines an infinite array of points in space that repeats a motif in all three dimensions. We call the series of points in space a lattice and the motif a basis. Swapping which atoms go in the motif should not change the structure of the lattice and viceversa. Luckily for me, all materials studied in the present project share the same crystal structure with only different atoms forming its basis.

GaAs, AlAs, InAs, GaSb, AlGaAs, and InGaAs are all part of the cubic crystal system. They are part of a subsystem called the zincblende structure, which esentially looks like two cubes with atoms in each corner and in at the center of each face, and that have been displaced by 1/4 in the (111) direction. Incidentally, this is the same structure that carbon atoms hold when forming diamonds! From a crystallographic point of view, this structure is numbered 216/230 out of all the available space

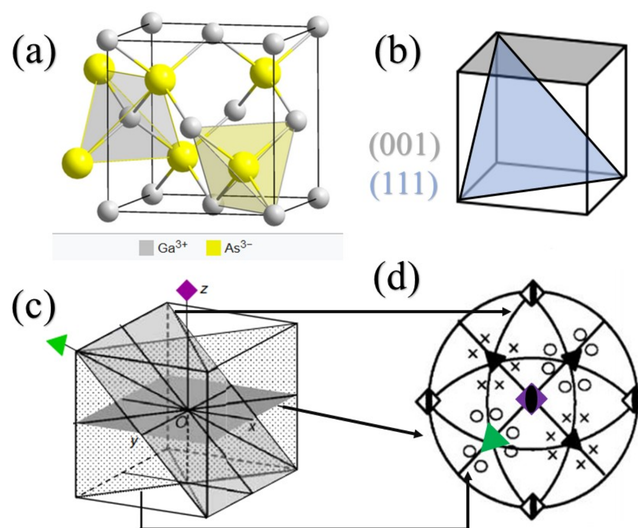

Figure 2.5: Schematics of crystallogrphic characteristics of the zincblende structure. (a) atomic arrangement of a unit cell (b) location of planes in a cubic unit cell (c) planes and axes of symmetry with their corresponding symbols and symmetries on the group F$\bar{4}$3m stereograph (d)

groups, and is labeled as F$\bar{4}$3m because of its face-centered cubic structure (German *Flächenzentriert*), a rotoinversion 4-fold symmetry, a 3-fold symmetry (characteristic of the cubic system) and a mirror plane.

It is important to highlight that this combination of symmetries leaves out the possibility of centro-symmetry (existing in C, Si, and Ge that share this structure) providing these materials with the properties of piezoelectricity to be discussed below. Within the cubic system we can identify several ways to look at *planes* of atoms. This is a way to visualize which atoms would be resting on a table where we to slash perfectly the sample along different directions. We can name these planes depending on where they would intersect with the sides of the cube. The Miller indices for planes in the cubic system serve this very purpose, and we can use them by observing that a plane called (001) would intersect the three sides of the cube that touch the origin

at lengths $(\frac{1}{x},\frac{1}{y},\frac{1}{z})$.

So in this example, the plane would intersect x at ∞, i.e. never. It would only intersect the z-axis at 1 unit of distance. These family of planes is then similar to the faces of the cube. the plane (111) would similarly intersect all axes at 1, making it coplanar with the cube's diagonal. The distances between atoms is not necessarily the same even if the atomic lattice is identical, owing to the chemistry of each atom. The lattice constants for each component are essentially the side length for the cube unit cell. Table 2.1 shows the lattice constants for the main materials and alloys used in this study.

Material	GaAs	AlAs	InAs	GaSb	$Al_{0.3}Ga_{0.7}As$	$In_{0.5}Ga_{0.5}As$
a ($\mathring{A}$)	5.6535	5.6611	6.0583	6.0959	5.6769	5.8558

Table 2.1: Lattice Constant for III-V Semiconductors used in this study at 300 K.

The difference in lattice constants usually imposes a limit to epitaxial growth due to the stress generated at the interface of two dissimilar materials (heteroepitaxy). The strain in these films can be calculated using the formula strain = a_{sub}/a_{sub}-a_{epi}. The thickness of the film that can be grown on a substrate with different lattice constant can be calculated using the Matthews-Blakeslee approach [8]. As an example, InAs on GaAs can only grow $\leq$ 1.7 ML before it forms small islands on the surface [9]. In order for two materials to grow coherently we can imagine that they both get distorted to an intermediate value. However, from Hooke's law we know that the restoration force that system experiences is proportional to the amount of compression applied to it. From this seemingly simple principle, we can generalize to three-dimensional arrangement of particles like our atomic lattice. Because of the

large thickness difference between substrate and epilayer, most of the strain will be located on the epilayer in the form of strain. Compressive and tensile strain are present when the lattice constant of the substrate is smaller than the epilayer, and larger than the epilayer respectively. The way strain is relaxed can take the form of defects. There are several situations in which atoms arrange themselves in ways that disrupt the crystalline uniformity. Among these defects we find interstitial impurities (small atoms finding their way in space between the lattice points), edge dislocations (where two lattice points accommodate a third one between them), self-interstitial atoms, vacancies, substitutional impurity atoms, and aggreates of impurities. Structual defects can include edge and screw dislocations, where atoms end up disrupting the surface of the crystal by adding a row of atoms or a slip plane, respectively.

2.2.2 Band Engineering

According to some ideas proposed during the last 130 years (at the time of writing) it is generally accepted that the structure of atoms consists of a nucleus with heavy baryons (particles made of quarks and gluons) and an electronic cloud surrounding them. In the previous subsections I discussed the behavior of these particles as a unit, and how ensembles of them provide a means to observe the emergent structural properties of the material. Now I will focus on the behavior of their electronic clouds, how the energy states get occupied and emptied, as well as simple considerations of the oscillations of the nucleons. What makes a semiconductor, well, semi-conduct? It is useful to think here of the two different cases surrounding semiconduction: insulators and conductors.

Trying to pass a large current through a piece of wood will irreversibly damage the cellular arrangement of the material, rendering it into a burnt piece of charcoal.

This happens because there is little room for the electrons in the wood to travel to neighboring atoms: the organic nature of the cells (carbons and hydrogens) make it hard for electrons to really separate from their nucleons without huge amounts of energy. In contrast, a conductor such as a metal will conduct electricity and heat without difficulty. In this case, atoms live in an electronically socialist society, with all exterior electrons (this is, the electrons that occupy the highest electronic states and are the least bonded to the nucleus) shared. Semiconductors live in between these two regimes and require only small amounts of energy to allow charge carriers to travel across the material.

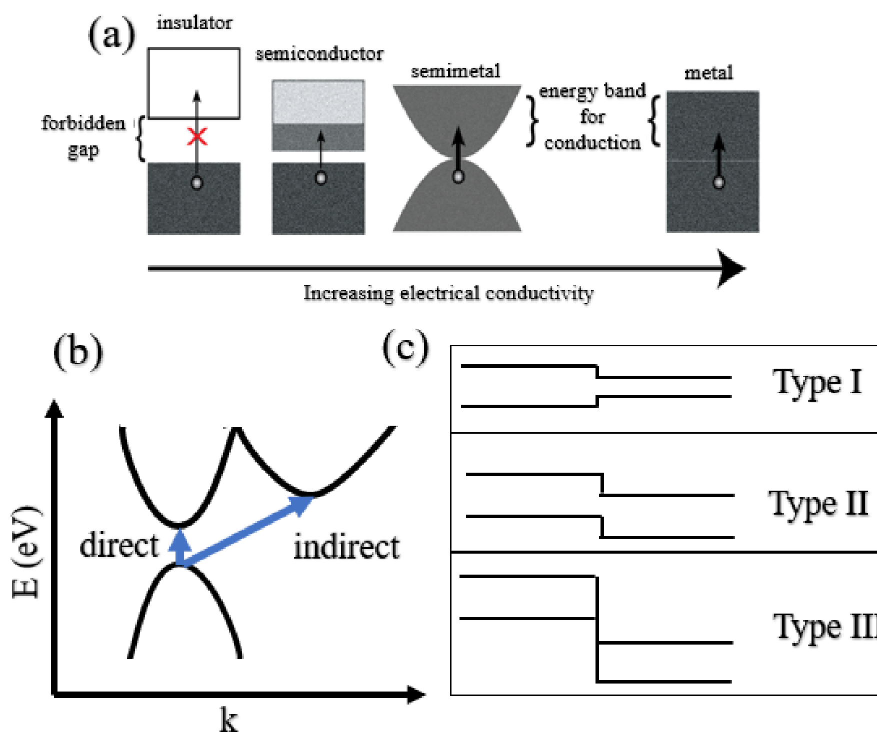

Figure 2.6: Schematics of electronic bands and their types. (a) depicts the different types of band gaps in materials. (b) different between direct and indirect band gap. (c) types of band gap alignments.

Considering a particular property of electrons will now allow me to form the basis

for what is considered the modern theory of solids. While the particles that form the nucleus can all have the exact same properties when they are interacting in the same system (same energy, momentum, mass...) this is not the case for fermions such as electrons. Due to the Pauli exclusion principle, these particles are prevented from sharing the same energy level in a system. The quickest way to visualize this phenomenon is by imagining an object that requires two full rotations, i.e. 720°, to come back to its original position. The geometric implications of this property give rise to an antisymmetric wavefunction that allows for ordering and discretization of energy levels in atomic systems.

Using this knowledge, we can graphically visualize an ensemble of atoms in very close physical proximity, such that their electrons' wavefunctions begin to overlap and now energy states begin to split into many different energies to accommodate the irreconcilable particles. A natural arrangement of the energy levels for electrons in materials like Si, Ge, GaAs, InAs, and GaSb makes it so that there is a certain range of energies in which no electron can live. We call this the band gap (Fig. 2.7)

When all electrons are in their lowest energy configuration in a semiconductor, they are statistically most likely to be living in the lower band of the forbidden energy region (the valence band). When the lowest excited state requires only energy to be reached (i.e. no momentum) we call the band gap a direct one (Fig. 2.7(b)). In the opposite case, when both energy and momentum are needed to reach the next available energy state across the band gap we call it an indirect band gap. The way electrons interact with bosons (such as photons and phonons) gives rise to several phenomena worthy of their own treatise, and there are several out there already written and detailing the minutiae of these processes. I will now summarize the most

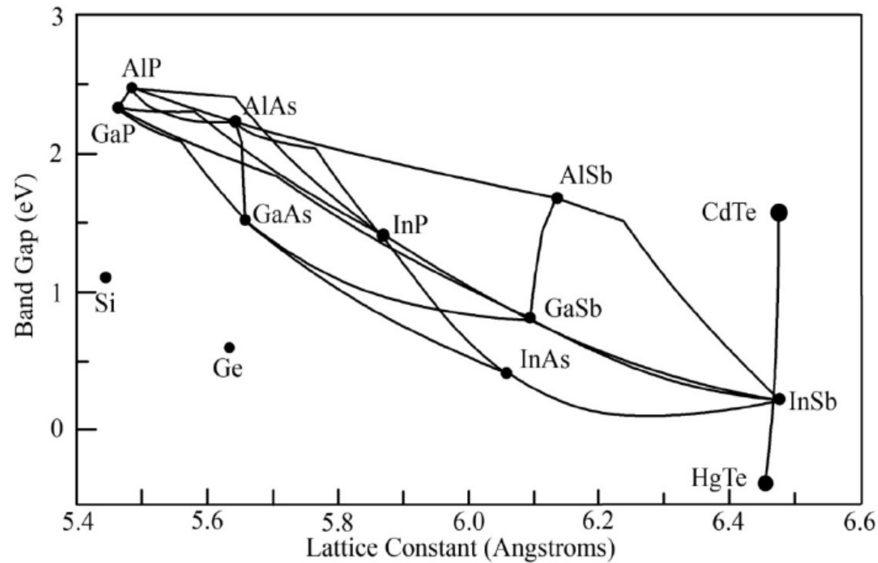

Figure 2.7: Band gap vs. lattice constant diagram for semiconductors. Adapted from Ref. [3]

important aspects of these interactions and how they relate to the present study.

When an electron absorbs the energy of an incoming photon, and this energy is larger than that of the band gap, the electron accesses a higher energy state. This leaves behind an absence of an electron with a lower energy, and this absence is called as its own particle, a hole. Much like vacuum, a shadow, and gas bubbles in beer it is easier to bundle their properties and treat them as an entity on their own. The resistance to acceleration (i.e. the "mass") of the hole is usually larger than that of the electron. Because it is essentially the absence of a negative charge, we can treat it as a "positive" charge that moves opposite to the flow of electrons. The opposite process, in which an electron loses energy and relaxes to a lower energy state is accompanied by the emission of thermal or luminal particles. It is by virtue of this process that we can motivate this study, and obtain light with tunable properties out of the the alignment of these electronic bands (see Fig. 2.7).

2.2.3 Quantum Effects

For this study there are three main areas of the dispersion relation between energy and momentum that manifest themselves in semiconductor materials. These are the maximum of the valence band, and the minima of the conduction band, specifically the Γ, X, and L points (corresponding to the 001, 110, and 111 symmetry planes). When we seamlessly integrate two semiconductor materials with one another -this is, we grow them epitaxially with abrupt atomic-level interfaces- their band gaps will not necessarily align (Fig. 2.7). Here is where we can began to take advantage of the quantum mechanical nature of the charge carriers and design our nanostructures.

For all the systems studied in this dissertation, we can simplify two of them (InGaAs/InAs and InGaAs/GaSb) to a one-dimensional band alignment system. This approach allows us a clearer understanding of the physics involved, and more details are provided in the corresponding chapters below. Let us bring in close proximity a small band gap material and "sandwich" it between two regions of larger band gap. Because of the structural discontinuity of how the charge carriers are able to move within the lattice, a sort of energetic well is formed (Fig. 2.8(b)). Tuning the dimensions of this structure to be in the order of a few nanometers provides solutions to the Schrödinger equation that predict the *quantization* of the carriers' energy [10].

The energy levels which the carriers can occupy can be calculated using the effective mass approximation (described below in Chapter 3) and numerically calculated using the program in Appendix A. This is not the end of the story, however. This work further relies in not only confining carriers to one dimension, but in all three. The effects of confining carriers in 3D using tensile strain adds two important factors to consider when calculating the energy of light emission: 3D confinement increases

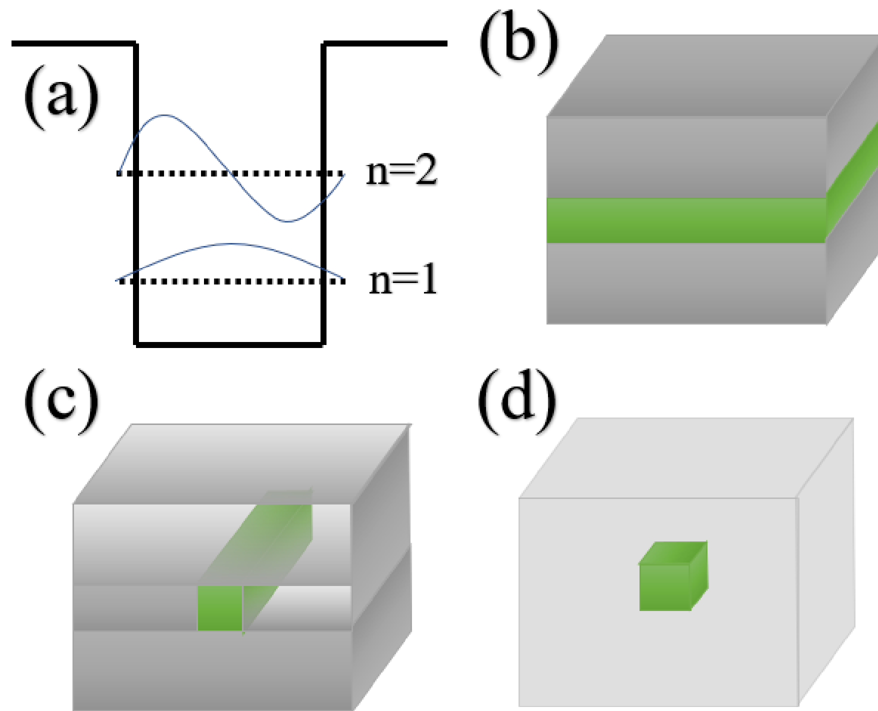

Figure 2.8: (a) Schematic of energy level quantization in a quantum well. The dashed lines correspond to the energy levels, while the blue solid lines correspond to the wavefunctions of each level. (b) schematic of a quantum well (c) Schematic of a quantum wire, and (d) schematic of a quantum dot.

the complexity of the calculations required, while tensile strain alters the shape of the conduction and valence band, pushing the confined states further above the band edge [11].

We should begin with understanding what energy levels are available for the charge carriers. The density of states present for different levels of dimensional confinement can be found solving the Schrödinger equation [12]. It is a combination of the available states and materials properties that allow us to fine tune and engineer the materials in order to produce the desired light out of these structures.

2.3 Growth of Solid-State Quantum Dots

The product of combining all the knowledge of the previous two subsections is the successful fabrication of semiconducting, solid-state self-assembled tensile-strained quantum dots (TSQDs). On a single crystal semiconductor substrate loaded inside the MBE reactor, we fine-tune the temperature, growth rate, elemental pressure ratios, and vacuum levels to create the ideal conditions (or sets of conditions) that give rise to tunable TSQDs.

A tutorial on how to grow the many different quantum dot systems using MBE is published from Vallejo, Sautter and Simmonds [3]. I will summarize the main steps and focus on the tensile-strained aspects used in the present study.

2.4 Characterization Techniques

In most physical science research programs once an idea is put forward, there are several ways to turn the idea into scientific knowledge. While debate still exists on the nature and defining characteristics of this type of knowledge [13], the steps involved have been refined over centuries of practice. Scientific imagination [14], computation modelling [15], and experimentation all play an important role in today's complex research projects. In this section I will briefly describe the physical and mathematical tools involved in providing us with a much more complete picture of the nature of each sample.

2.4.1 X-ray Diffraction

As mentioned earlier, our study of solids is systematically well defined when we consider the atomic arrangement of their nanostructures. In order to be able to resolve the distances between planes of atoms we need rays of light whose wavelength is com-

parable to the size of atoms. This is mainly due to the phenomenon of diffraction, where light encounters and interacts with an obstacle. When the spacing of the obstacle is of approximately the same length scale as the wavelength of the light each point from which light comes after the interaction can be treated as a source point. this process gives rise to diffraction patterns and various dynamic interplays between light and matter can be exploited to study the structure of the sample.

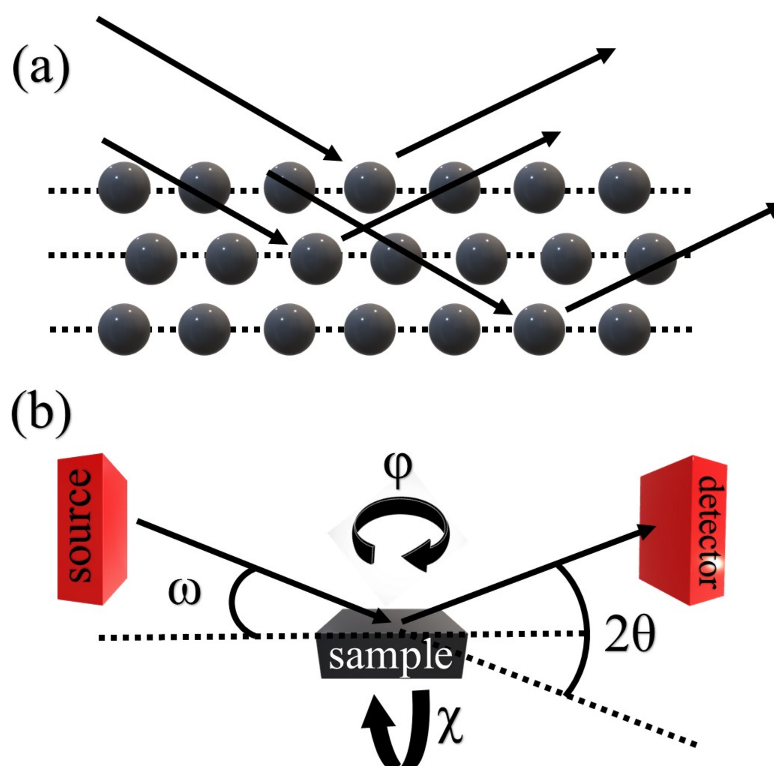

Figure 2.9: (a) Schematic of reflection of x-rays off a series of atomic planes. (b) Schematic of XRD setup with associated scanning angles.

The spacing between the atomic planes that form the “faces” of the cubic struc-

ture of our materials of interest can be measured as the lattice constant of the material along the (001) direction. Table 2.1 summarizes these distances. I performed the x-ray diffraction analysis of our samples using a Bruker AXS D8 Discover x-ray diffractometer, housed in the Boise State Center for Materials Characterization. This diffractometer has a Cu source that emits Kα1 x-rays . The resulting photon has a wavelength of 1.5406 Å. Each sample is measured individually by placing it on a goniometer (a device to very precisely measure angles along different directions) and detecting the intensity of the diffracted x-rays coming from the sample. Alignments that ensure the best detection include a height (z) scan, an initial rocking curve, followed by a χ-scan, and finally a $2\theta/\omega$ scan.

These sets of measurements provide an estimation of the deviation of the crystal structure of the sample from the ideal Bragg condition $n\lambda = 2d\sin\theta$. The resulting diffraction patterns have a Gaussian distribution whose full-width half-maximum (FWHM) measure tells us about the crystal quality. For samples where more than one material is present, the center intensity of these distribution peaks can tell us the alloy composition, as well as the degree of lattice matching/strain present.

We can do this by analysing a sample of ideally lattice matched InP/InAlAs/InGaAs (system for which I fabricated and characterized dozens of samples). An ideally grown sample would have a single peak, with very narrow FWHM. In reality, we often find three different peaks with different heights and FWHM. By measuring the angular distance between the center of the peaks we can calculate the excess or lack of a certain element based on where its center peak should be according to Bragg's law.

2.4.2 Atomic Force Microscopy

For systems in which the morphology of the surface is an important property, we utilize atomic force microscopy in order to quantify the roughness (often in the order of Å) and presence of self-assembled structures. The way this technique operates is through measuring the laser deflection off a very small cantilever that is in electromagnetic contact with the surface of interest. The cantilever has a natural frequency determined by its material properties.

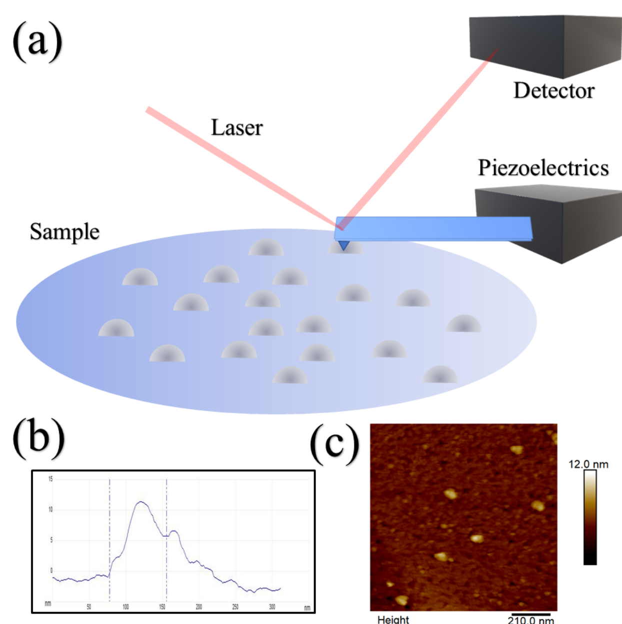

Figure 2.10: (a) Schematic of surface analysis using in an AFM setup. (b) Profile of a scan used to generate surface topology data.

There is a small tip at the end of it, which interacts through van der Waals forces

with the surface of the sample, altering the frequency of oscillations in the cantilever. By scanning the same segment of the sample in both directions (left and right, or up and down) a retracing factor provides a measure of the quality of the scan. For this study, we grew a majority of the samples with a surface layer of QDs or other self-assembled structures that could be studied using AFM. We measured the height, diamater, and overall shape of these structures using AFM.

2.4.3 Transmission Electron Microscopy

Just like AFM allows us to inspect the surface of a sample with atomic precision, TEM can create micrographs which show atomic resolution and different aspects of the crystal lattice or surface morphology, depending on the mode of operation. In this device there is an electron source often located at the top. A high voltage is applied to the electrons which pass through a series of condenser lenses (essentially magnets) that focus the electron beam onto the sample. The wavelength of the electrons (as described by de Broglie's relation $\lambda = h/p$) is around 2.7 pm when the applied voltage is 100 kV (remembering of course that at these voltages, we must take into account relativistic effects when calculating the momentum p of electrons). Arguably the hardest part of imaging a sample in TEM is preparing it.

A focused ion beam (FIB) setup is commonly used to selectively etch and shape a sample into the correct geometry (thickness and shape) required for high focus imaging. This technique uses the same principle of accelerated charged particles by a high voltage which instead of electrons, uses atomic ions such as Ga or Ar. More conventional mechanical preparation of samples is still common among institutions with fewer economic resources. This is the type of sample preparation I used to image the initial GaAs/AlGaAs multiple quantum wells (MQW) used during my studies.

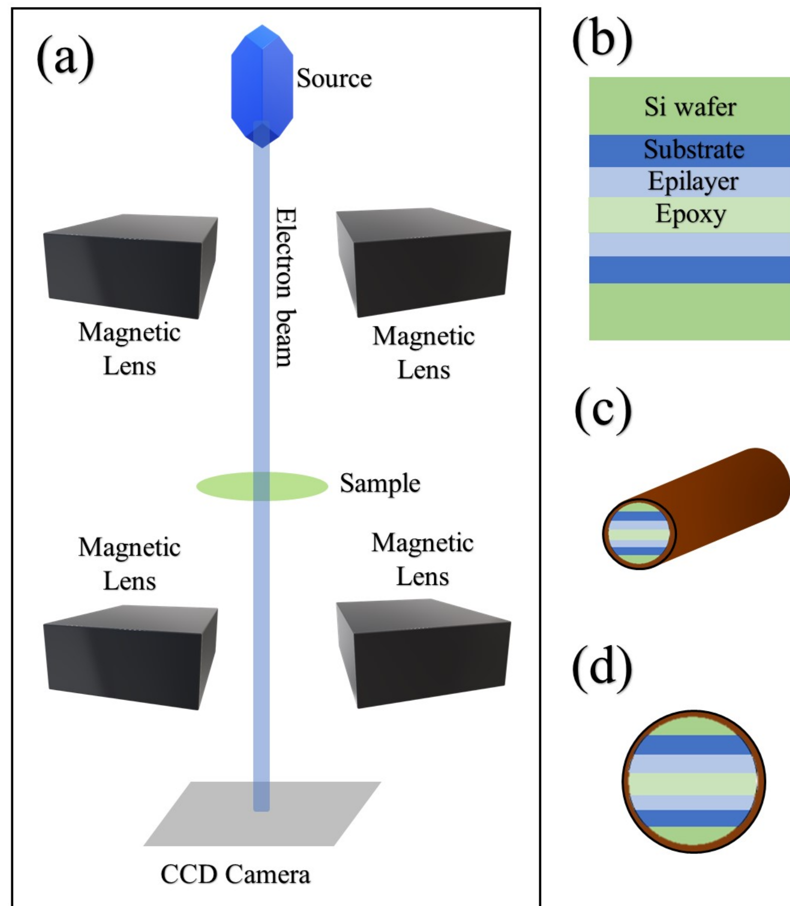

Figure 2.11: (a) Schematic of a transmission electron microscopy setup. The electron beam is aligned through a series of magnetic lenses before and after interacting with the sample. (b) Schematic of layers used to mechanically fabricate a TEM sample, (c) shows the geometry of integrated sample layers in a copper tube, before being sliced into a sample as shown in (d).

The preparation begins by sandwiching two pieces of the same sample with the epilayers facing each other. By gluing them together with thermally-cured epoxy and two thick layers of Si wafer on the outside for structural integrity. Following the curing, a mechanical drill is used to cut a cylinder in the middle of the stack with the

layers of interest right in the middle. This is made possible by a carbon slurry with μm diameter particles in suspension. After this, the cylinder is slid into a copper tube of similar diameter and cured with epoxy again.

Once the copper cylinder is ready, it is sliced into very thin sections with a diamond saw in order to produce several circular samples. These small circles are then thinned with a selection of several sanding paper levels of increasing fineness, until they can be atomically prepared using an ion beam mill. When the sample is finally selectively damaged to atomic levels, it is ready to be inserted into the TEM chamber.

With the sample inside the chamber, a vacuum is produced inside the sample chamber before focusing the electron beam. It is here when through the passing (hence the *transmission* part of the name) of electrons through the sample we can magnify the signal and absorb the electrons onto a CCD camera and observe sub-nanometer features. It is important to highlight that thinning the sample is very important, since it must be in the order of 10 nm in thickness for the electrons to successfully go through it.

2.4.4 Scanning Electron Microscopy

Using a very similar approach to the generation and acceleration of electrons in a TEM, SEM takes advantage of the interaction between the sample's electrons and the way they are ejected to study the surface of interest. When the electrons are focused onto the sample's surface, some of them are simply backscattered, while others generate a shower of secondary electrons that come from the surface atoms. Detection of the energy, momentum, and direction of these electrons is then used to image the surface with nanometer resolution. Sample preparation for SEM requires non-conductive samples (such as the semiconductors used in this study) to be coated

with a thin layer of a conductive material. This is done in order to avoid charge accumulation in the surface of the sample.

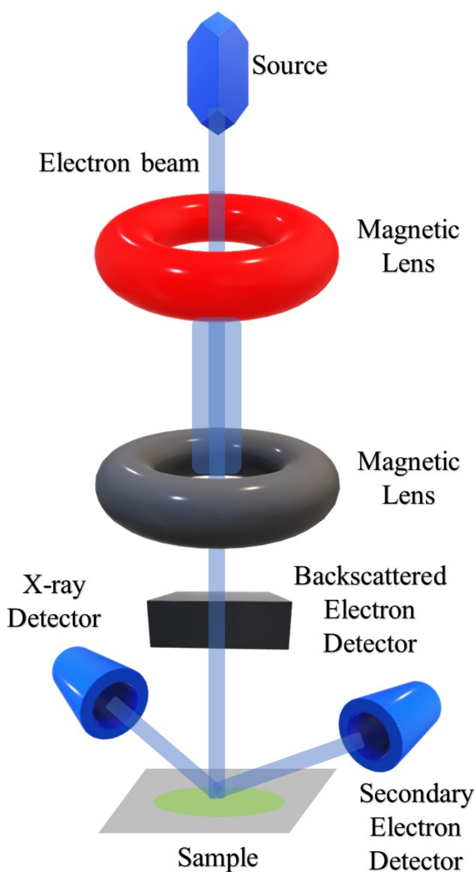

Figure 2.12: Schematic of a scanning tunneling microscopy setup. An electron beam is aligned through a series of magnetic lenses before hitting the sample, where data is acquired through a series of detectors for backscattered electrons, secondary electrons, and x-rays.

2.4.5 Photoluminescence

Photoluminescence is a technique that allows us to measure the intensity and energy of the light emitted by our nanostructures. By exciting the electrons in our samples

using photons with higher energies than those of the semiconductor bandgaps, we stimulate the emission of their characteristic energy levels. As explained in section 2.2.2 we provide energy to the valence electrons of our samples in excess to that of their band gap, which then is released in the form of radiative and non-radiative energy (light and phonons). We can then measure the luminal response and determine what the band alignment and sizes are.

Sample preparation is comparatively simple in this technique, as we can simply coat the back of an as grown sample (being careful to remove any excess indium from the growth process mounting, see section 5.2.1) with silver paint and mount it on a copper plate. This copper plate is then placed inside a cryostat, which through a compressor decreases the temperature to either liquid nitrogen or liquid helium levels (77 K and 7 K, respectively). Through a small viewport, a laser is then shone onto the sample with known power, wavelength, and angle. Emitted light is then collected by a detector and analyzed using specialized software. The wavelength of light emitted by the samples will determine the type of detector used, and this in turn determines the type of PL that is being carried out. These types of detectors will collect different colors of light with varying efficiencies, and are summarized in Table A.1.

Type of Detector	Silicon (Si)	InGaAs	HgCdTe (MCT)
Spectral Range (nm)	350 - 1100	850 - 1700	1000 - 5000

Table 2.2: Spectral Detection Range for PL Detectors

The way the detector records the intensity of light at each of the different wavelengths is done by selectively diffracting the light coming through the sample through a set of different gratings. When non-monochromated light hits the diffraction grating, the zero order light is reflected at an angle similar to the incidence angle; light

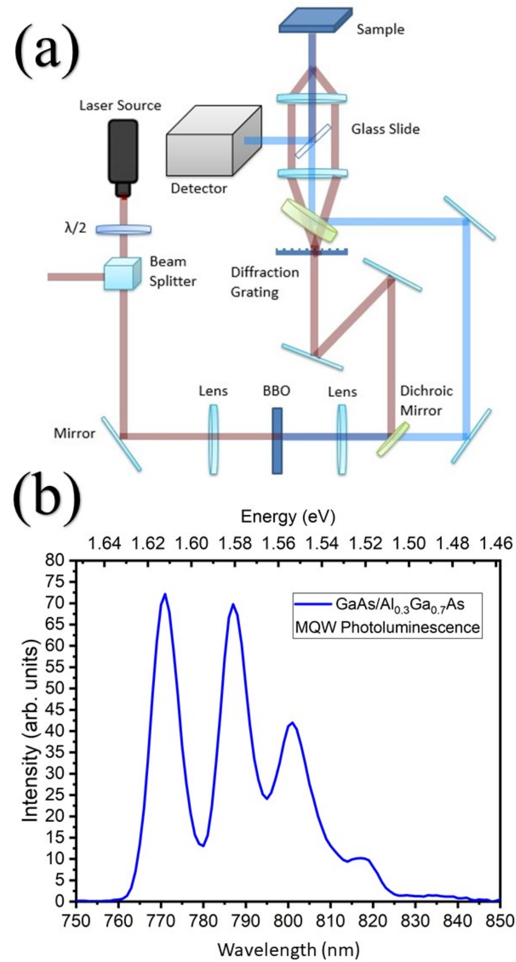

Figure 2.13: (a) Schematic of a photoluminescence setup. The laser beam used to stimulate the sample electrons goes through a series of lenses and mirrors to focus and align the correct geometry for the beam, after which emitted light is directed towards a detector. (b) PL spectra of a GaAs/AlGaAs multiple quantum well (details provided in chapter 3).

that has interacted with the grooves of the diffraction grating travel at angles that depend on the width of the grooves and their wavelength. This light is then collected by rotating the diffraction grating and aligning with the detector.

2.4.6 Raman Spectroscopy

Raman scattering is the process of inelastic light scattering in which the energy of scattered light is different from that of the incident light by the energy of an elementary excitation (molecular or crystal lattice vibration or electronic excitation) participating in the process. The different vibrational states of each atom emit different types of light that can then be collected and analyzed. Energy absorbed by the different vibrational modes can be detected to provide information on the strength and type of bonds in the samples. For this study, I used Raman spectroscopy to verify the composition of the AlGaAs alloy used in Chapter 3.

2.4.7 Nomarski Imaging

Also known as differential interference contrast (DIC) imaging, this technique relies on separating polarized light into orthogonal paths and combining them before detection in order to enhance contrast and increase the resolution of the produced image by analyzing the difference in path lengths. Samples whose surface has features in the order of tens of μm are too rough for AFM. These types of samples can be imaged using Nomarski microscopy in order to get a sense of the surface morphology without damaging more sensitive equipment.

2.4.8 Reflection High Energy Electron Diffraction

RHEED is technique that similar to TEM and SEM, makes use of accelerated electrons to 14 kV which are then directed towards the surface of a sample at very low angles, and then detected on a fluorescent screen. The diffraction pattern that appears is an indication of the amount of order present in the surface in question. Highly ordered surface will show streaky patterns that are the result of the cross-

section between the Ewald sphere and the volume of detection. This makes RHEED a uniquely equipped technique to use during MBE growth in order to analyze the surface reconstructions present *in situ* and *in operando*.

We can determine the quality of the surface using the level of quality in the streaks present in the RHEED pattern. A spotty pattern is the result of irregular structures on the surface of the sample diffracting the electron beam in a disordered manner. Streaky patterns in contrast are the result of the sample's high quality flat surfaces.

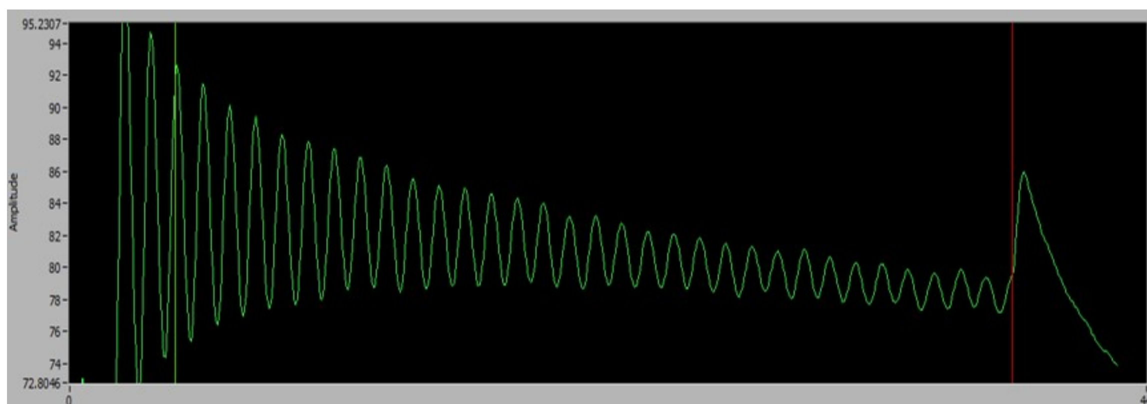

Figure 2.14: Plot of the RHEED intensity pattern

Often we can determine growth rates for different materials using the oscillation of the intensity of the RHEED pattern. These RHEED intensity oscillations (RIOs) have maxima when the the surface is completely smooth (a full layer of coverage) and minima at the point of maximum disorder. We can determine a very accurate growth rate by timing the period of these oscillations.

2.4.9 Residual Gas Analysis

RGA is a technique used to measure impurities in high vacuum systems. The RGA setup produces a beam of ions through the collisions of gas and electrons produced in the cathode, which are then filtered according to their mass to charge ratio (Fig.

2.15). This way pressures in the order of 10^{-14} Torr can be detected. It is here where we really can appreciate the outgassing levels of stainless steel and why it is the choice of material for ultra-high vacuum technologies. Stainless steel is ideal because of its H_2 and H_2O outgassing properties, its strength and relative ease of pumping down to UHV conditions.

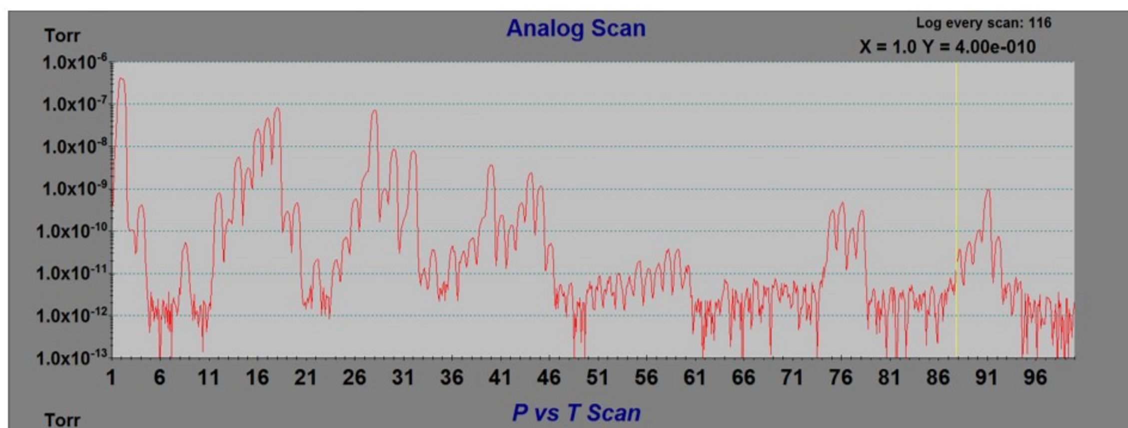

Figure 2.15: Plot of an RGA signal analysis. The x-axis represents the weight of the atoms detected, while the y-axis is a logarithmic scale of the pressure for each value.

CHAPTER 3:
DYNAMIC QUANTUM DOT GENERATION VIA SURFACE ACOUSTIC WAVES USING TRANSIENT GRATING SPECTROSCOPY

Kevin D. Vallejo, Zilong Hua, Amey Khalnokar, David Hurley, and Paul J. Simmonds

3.1 Introduction

This introductory study aims to achieve the dynamic lateral confinement of charge carriers in 2D and 3D using near-THz surface acoustic phonon pulses in polar semiconductors grown using molecular beam epitaxy (MBE). By means of acousto-electrical effects, the final goal of this work was to measure the degree to which surface acoustic waves (SAWs) confine electrons and holes, limiting the number of recombination processes. Applications for this technological development include the external modulation of lateral confinement size in the SAWs and subsequent photon emission wavelength, as well as potential quantum logic gates design using acoustic pulses to drive electrons in a circuit.

New devices based on nanoelectronics are currently in development as potential disruptive technologies in the fields of quantum computing, sensing, energy conversion

and storage, and cryptographic technologies [16]. The manipulation of charge carriers is the common denominator for these technologies, and more efficient ways to achieve on-demand control can lead to reliable qubit networks [17], non-destructive sensors [18], more efficient solar panels [19], and single-photon emitters [20]. Control of the number of electrons that are transported across the devices is a potential avenue for energy optimization and increased frequency of operation, making it an important area of research.

Transport of charge carriers in solid state devices using externally controllable stimuli can be achieved through the coupling of mechanical stresses and electrical properties, such as the deformation potential and the piezoelectric effect [21]. By applying an external mechanical stimulus to the surface of a semiconductor with no center of inversion such as zinc-blende GaAs (group $F\bar{4}3m$) the piezoelectric tensor creates an electric field along certain crystallographic orientations. A simple case to study is applying a stimulus normal to the [001] direction to obtain a piezoelectric response along the [011] direction [22]. This mechanical stimulus will take the form of a surface acoustic wave (SAW) that is mostly confined in depth within one wavelength of the surface, similar to seismic Rayleigh waves [23]. Because the shape of the mechanical wave induced on the sample directly affects the shape of the potential wave, the electric field created can be tailored to trap the excited charge carriers that create excitons (bound electrons and holes, see section 2.2.2) and trap them in the potential travelling wave. The excited carriers come from the quantum wells, where they are confined. Electrons promoted to the conduction band will be trapped in the valleys of the potential wave, while holes will be in the crests (Fig. 3.1), as shown by Rocke *et al.* [24].

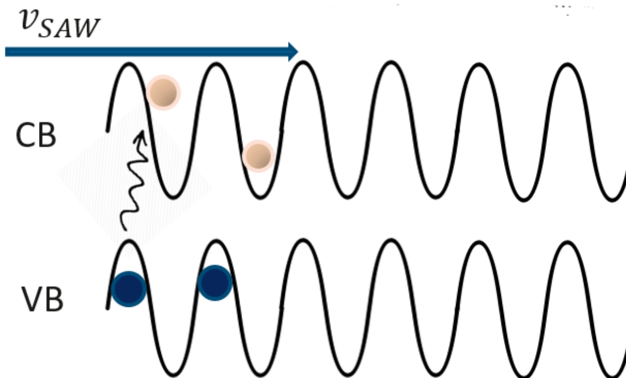

Figure 3.1: Schematic of charge carrier trapping in potential wave generated by a SAW in a piezoelectric semiconductor.

The carriers transported along in these waves have significantly lower recombination rates, extending their lifetime potentially by orders of magnitude, and can be transported across distances of up to 1 mm[24]. The temperature and angular dependence of waves travelling at different angles on GaAs were identified and characterized even for non-piezoelectric directions by Powlowski *et al.* [25].

3.2 Methods

There are several ways of generating elastic waves in solids: using a high-power laser materials can be ablated, which generates a stress perpendicular to the surface, launching the elastic wave. Using lower power lasers, a local thermal gradient can induce a force dipole that generates a lattice expansion that relaxes by phonon emission. Depositing a metallic grating (transducer) with interdigitated fingers (IDT), a radio-frequency voltage can be applied and through the inverse piezoelectric field a set of waves can be generated, whose wavelength corresponds to the period of the IDT gratings. Alternatively, this IDT can be optically excited creating a thermal coupling that in turn launches the waves. Lastly, the approach we propose in this

study relies on the beat created by two lasers of differing frequency (this is the difference in frequency that will be "heard") incident on a semiconductor substrate. Very short wavelength SAWs have been produced with this method [26], down to 45 nm. It is important to highlight that shorter wavelengths provide greater access to the smaller features in samples, opening them to study with non-destructive techniques, in addition to confining the charge carriers in the direction of the wave propagation.

It is our aim to take full advantage of the three-dimensional nature of the SAW generated in a multiple quantum well by calculating the depths of maximum stress created by the travelling wave below the surface and placing a quantum well (QW) that will act as a two-dimensional electron and hole gases (2DEG and 2DHG, respectively) where quantum confinement of the carriers can be probed using optical techniques, such as photoluminescence (PL). Extending this line of thought, three QWs can be grown epitaxiallly using molecular beam epitaxy (MBE) to locate the points where maximum modulation of the conduction and valence band occurs, following Rudolph *et al.* [27]. By using a finely tuned laser beam, split into pump, probe and reference beams as in Fig. 3.2 (following Every *et al.* [28]) we can measure the PL spectra of the three QWs buried below the surface of the sample (as in Fig. 3.6) and see them disappear as the carriers are separated spatially by trapping in the potential wave.

3.2.1 Elastodynamics

A crystal structure is defined as the sum of a uniform arrangement of points in space (lattice) plus a set of atoms occupying that space (basis). This uniformity need not be the same in all directions. Anisotropy is a result of either the atomic basis, the lattice, or both, generating a set of (or lack of) symmetries in the structure (Fig.

2.5(a)). The propagation of sound waves in crystals owes its rich array of anisotropic phenomena to its dependence on a fourth-order elastic constant tensor. Heat and sound conduction, electric conductivity and arguably even water filtration levels are all effects dictated by the arrangement of these atoms [29, 30].

Strain is the displacement a material feels in the direction of propagation of the wave, also known as dilatation. Shear stress is the tension or compression a material feels in a direction normal to the wave propagation direction. Stress is a property akin to pressure where a force acts on area. Strain is defined as the rate of change of displacement with respect to distance, and is often used as a measure of deformation. Following the approach of Farnell [31], I derived the solutions to the wave equation propagating in semi-infinite media (derived in Appendix A) that can then be applied to cubic crystals to extract displacement equations seen in Royer *et al.* [23] (also fully derived in Appendix A):

Velocities along [100]

$$\begin{cases} V_L = \sqrt{\frac{c_{11}}{\rho}} \\ V_T = \sqrt{\frac{c_{44}}{\rho}} \end{cases}$$

Velocity along [110]

$$\begin{cases} V_L = \sqrt{\frac{c_{11}+c_{12}+2c_{44}}{2\rho}} \\ V_T = \sqrt{\frac{c_{44}}{\rho}} \end{cases}$$

where V_L is the longitudinal velocity, V_T is the transverse velocity, C_{ij} corresponde to the stiffness constants, and ρ is the density of the material. Waves travelling

on crystalline media have different velocities that vary because of phonon focusing effects that can be observed in the bulk of materials, as well as in their surfaces due to the angular dependence on the three acoustic polarizations of their phase and group velocities [32]. The study of these waves owes its origin to the work of Lord Rayleigh in 1885, whose contributions made it possible for geophysicists to study the displacement of earthquakes and be able to prevent disasters [33]. A possible interdisciplinary offshoot of the present proposal is to establish a reliable method of generation and detection of waves on semiconductor samples that mimic the physical characteristics of the earth's crust to be used by geophysicists to test earthquake models.

3.2.2 Deformation Potential and Piezoelectricity

The deformation potential interaction results from local changes in the crystal's energy band arising from the lattice distortion created by a phonon [34]. The phonon produces a strain field in the crystal which in turn produces a local change in the band energy. This interaction is one of the major scattering mechanisms in non-polar semiconductors. In polar semiconductors, an external strain produces a polarization which results from the displacement of ions. This is known as piezoelectric coupling. Thus, acoustic phonon modes drive macroscopic polarization in piezoelectric crystals. This property is one of the most important characteristics of our system. The piezoelectricity (*piezo*-, to squeeze) is part of a series of physical responses a material provides given a small stimulus mediated by the intrinsic response of its structure. It is defined as the electric moment per unit volume, or polarization charge per unit area, which in the case of these materials arises from a strain in the crystal lattice.

Symmetry considerations show that to characterize the piezoelectricity of GaAs

we need only define one value, corresponding to the entry in the piezoelectric tensor $d_{14} = 0.16$ C$/m^2$, known as the piezoelectric constant [22]. Shifts in the excitonic photoluminescence spectrum are attributed to the piezoelectric effects that arise when a strain field modifies the samples [35]. Hirakawa and Sakaki [36] calculated the deformation potential constant for a heavily doped GaAs/$Al_xGa_{1-x}As$ heterojunction to be ≈11 eV. They also showed that the piezoelectric potential was only about 10% of this quantity. Researchers have also shown that the deformation potential acts at short range, while the piezoelectric coupling can act at long range and is orientation dependent, allowing us to separate their contributions [21].

Strain plays a big role in the band gap opening as it depends on the deformation potential. A compressive strain will increase the band gap, while a tensile one will generally decrease it. When a series of layers are grown with many periods, an intermediate lattice constant may be adopted by the material where two-dimensional compressive and tensile strain are complemented by a uniaxial distortion perpendicular to the grown layers.

3.2.3 Transient Grating Spectroscopy

Transient grating spectroscopy (TSG) is a time-resolved optical technique that relies on interfering laser beams monitored through diffraction of a third probe laser beam [37]. It uses the optical interference of two or more excitation pulses overlapped at the surface of a sample, where local heating in a geometry defined by the pattern of interference produces acoustic disturbances, usually in a sinusoidal shape, since the surface acoustic modes are the primary contributors to the surface displacement.This technique has been used to analyze the thermal transport and acoustic properties of systems such as thin-film semiconductors, microsphere lattices, and materials under

irradiation [38]. The uniformly distributed wave train can be then measured using the diffraction of a third beam and compared to a fourth beam used as an oscillator reference in a process known as heterodyne amplification [38].

Optical heterodyning is a process where two slightly different wavelengths illuminate a detector and the difference in their frequencies produces an oscillating electrical output. It can be used to precisely measure phase and frequency of light signals relative to a reference light source. A schematic of this setup can be seen in Fig. 3.2. The interfering beams are generated by passing short-pulsed lasers through a phase mask consisting of a volumetric diffraction grating. This phase mask is designed to diffract a big proportion of the light into the ± 1 orders of diffraction while the rest of them are filtered. This is an attractive alternative as it provides a means to generate a wave train of continuous SAWs on the surface of our sample and can accurately and non-destructively characterize these high-frequency acoustic systems. An alternative way of generating the two laser excitation beams is an energy separator cube [39]. Spatial translation of the beams changes the spacing between the beams, in turn changing the crossing angle on the sample. In contrast, the phase mask pattern must be entirely changed to alter the crossing angle and the optical fringe spacing on the sample.

The detection options available for TSG are heterodyne detection, 2D scanning probe with interferometry and using a time-delayed probe. 2D suspension platform interferometer (SPI) uses an ultrafast optical pump and probe technique with a common-path interferometer. By focusing the pump light on a small spot at normal incidence from the sample, out of plane motion is detected interferometrically with pm resolution by using two probe pulses at 510 ps intervals at normal incidence

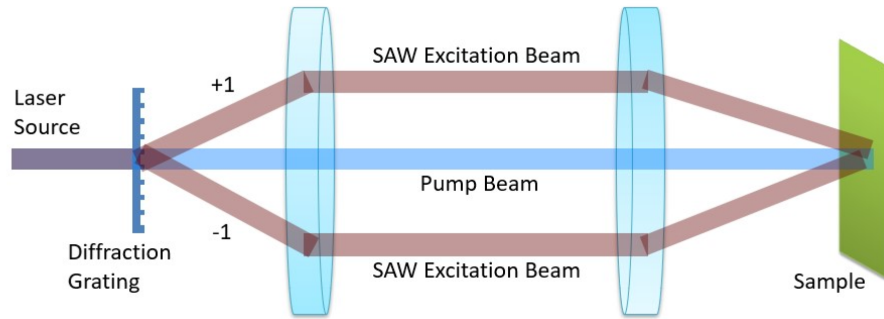

Figure 3.2: Schematic of a transient grating spectroscopy laser splitting setup. Using two lasers of different wavelengths the excitation of the carriers and the SAW train can be generated and measured within the same region.

from the other side of the sample.

This approach also allows for the dynamic, external control of lateral confinement of carriers to "movable" quantum wires (QWi) and quantum dots (QDs). In contrast to the established methods of self-assembly [11], droplet epitaxy or pre-patterning of substrates, where the quantum dot and wire confinement is constrained by the physical dimensions of the structure, trapping charge carriers in dynamic and controllable SAWs parallel to the plane of the substrate (with the last dimensional confinement provided by the quantum well) promises tunable, discrete low-dimensional systems that can be controlled. This opens the door for single-photon emitters with on-demand wavelength, as well as dynamic confinement to transport the exciton along the QW.

3.2.4 Sample Growth

We grew a GaAs/$Al_{0.3}Ga_{0.7}As$ multiple quantum well structure on a GaAs(100) substrate using a GEN 930 MBE system. The structure consisted of three quantum wells of different thicknesses placed at different depths to exploit different stress conditions

and excitonic optical resonances (see Fig. 3.3). Substrates are placed mounted on a molybdenum block using In metal bonding, which provides temperature uniformity across the sample. The samples are then put under vacuum conditions for 16 hours prior to mounting them on a substrate heater inside the growth chamber. Here the temperature is monitored using a thermocouple and a pyrometer, which are both checked against known surface reconstructions for this substrate. After oxide desorption, we decreased the substrate temperature to the growth temperature (580° C). At this point the surface shows a slightly spotty (2 × 4) surface reconstruction, which turns fully streaky after deposition of a few monolayers of epitaxial GaAs.

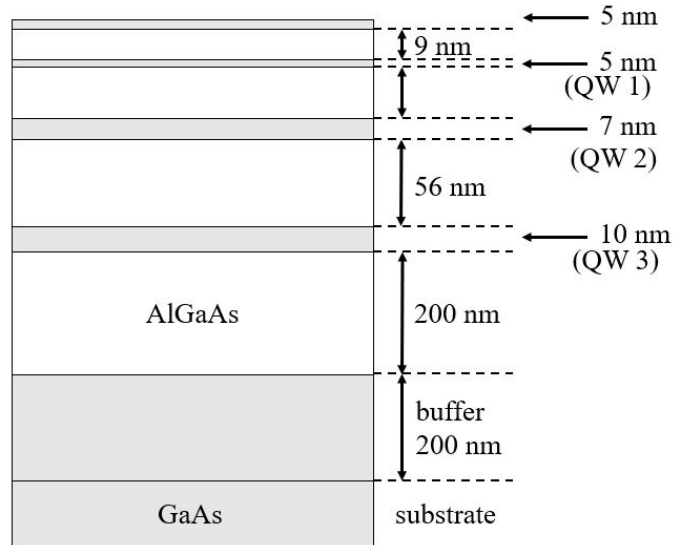

Figure 3.3: Schematic of the multiple quantum well structure used for this study. Gray sections correspond to GaAs and white sections to AlGaAs. The $Al_{0.3}Ga_{0.7}As$ composition is determined using RIOs, XRD, and Raman spectroscopy.

3.3 Results and Discussion

We employed several different characterization techniques that served as hands-on training for the author. The date we acquired showed the high quality sample fabrication level we are able to produce, both structurally and optically.

3.3.1 X-ray diffraction

After calibrating our composition using RHEED intensity oscillations with a couple of samples, we did a $2\theta/\omega$ analysis of the samples to determine the level of agreement in alloy composition. Vegard's law dictates an almost linear dependence of the lattice constant of $Al_{1-x}Ga_xAs$ with concentration x. We determined a very close agreement in the alloy content for x=30% in addition to a high film quality evidenced by the presence of Pendellösung fringes. These fringes are the product of the unpolarized x-rays satisfying electromagnetic boundary conditions for the Bragg condition. [40]

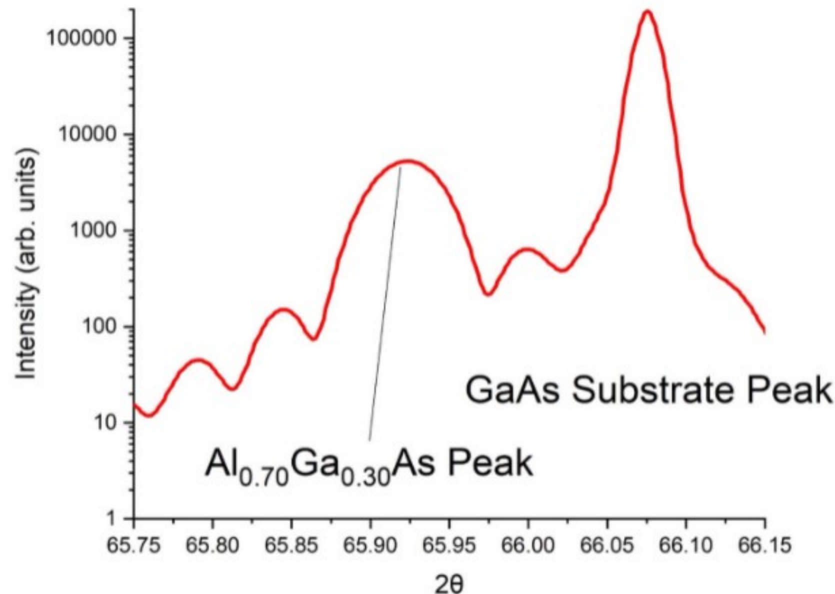

Figure 3.4: XRD pattern of a $Al_{0.3}Ga_{0.7}As$ MQW.

3.3.2 Raman spectroscopy

To make sure our sample composition is accurate, more than one technique was used. Raman allows the measurement of the response from the AlGaAs alloy and comparing the peaks corresponding to both GaAs and AlAs optical phonons provides information on the composition, as calculated by Kim and Spitzer [41].

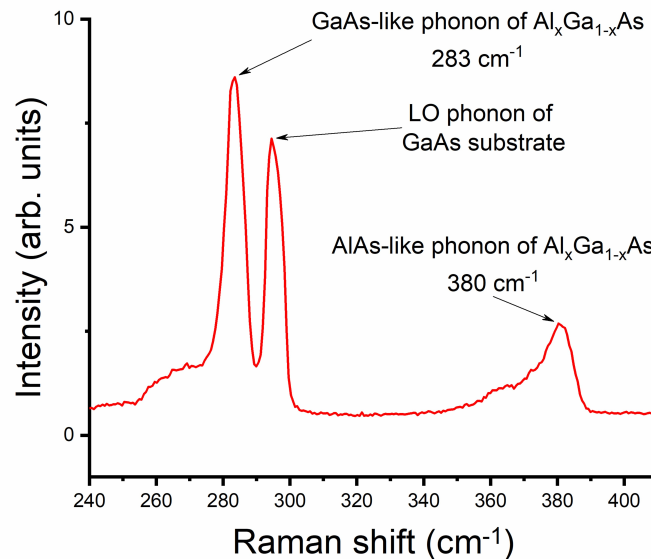

Figure 3.5: Spectrum of a Raman spectroscopy study of the same GaAs/AlGaAs MQW. We used a 532 nm laser to measure the sample at 8 K. The position of each peak is determined by the composition of the alloy, and measuring the peak's center provides us with a measurement of Al content.

3.3.3 Photoluminescence

The structure consisted of three quantum wells of different thicknesses placed at different depths to exploit different stress conditions and excitonic optical resonances (see Fig. 3.3). Each one of these three quantum wells would have a specific confined

state above the band edge that we can calculate and measure.

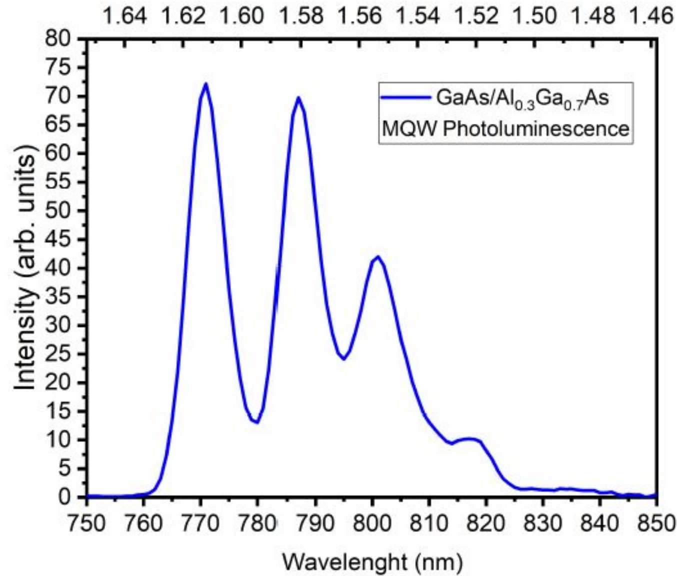

Figure 3.6: Photoluminescence spectrum of the multiple quantum well structure used in this study. The sample was measured at 7 K and measured with a 532 nm laser wavelength.

Figure 3.6 shows four very clear peaks which we can assign to each of the QWs and the GaAs substrate. The optical quality displayed by these samples is indicative of a low-defect level and overall structural integrity, ideal for this project.

Using a simple particle in a box model we calculated the energies for the electronic transitions in these quantum wells in an isolated form at 7 K and obtained values that are within the vicinity of experimental values (Fig. 3.7).

3.3.4 Transmission Electron Microscopy

We verified the structure growth using a JEOL JEM-2100 HR Analytical Transmission Electron Microscope (TEM) as seen on Fig. 3.8. Each of the planned layers is present and GaAs is distinguishable from AlGaAs by the contrast in the image, where darker colors correspond to GaAs. Comparison in expected thicknesses between figures 3.3

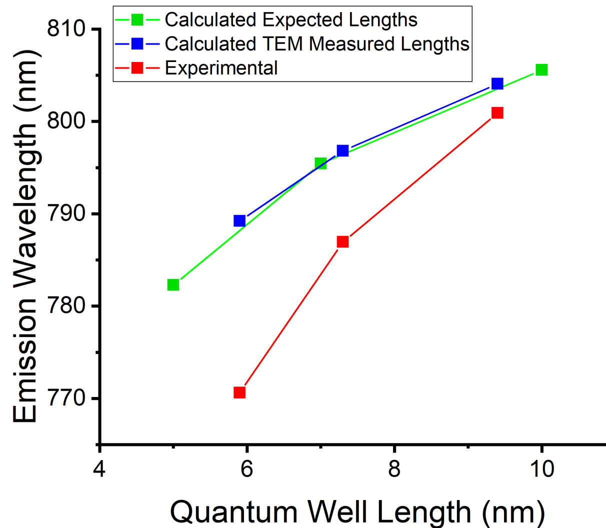

Figure 3.7: Plot of emission wavelength from the MQW sample calculated from expected values (green), calculated from measured well thickness in TEM (blue) and experimental values taken from PL (red).

and 3.8 illustrates an error of $\leq 2\%$ in the nominal calculated value. This confirms the high structural quality we inferred from the PL studies.

3.4 Conclusions and Future Work

In this study we were able to calculate the depths at which GaAs QWs would be aligned with the high stress points of a SAW travellin on the surface of the sample. Using MBE we fabricated a structurally sound and optically active sample ready for future implementation in a TSG setup. Development of this setup requires the implementation of a working PL setup for which advances have been developed. Inclusion of a second and third laser (plus optical equipment required for diffraction) are the following steps. We started the development of quantum logic gates using this technology and will continue to develop this approach as the experimental setup is installed. We attempted this development during the summer of 2019, and were able

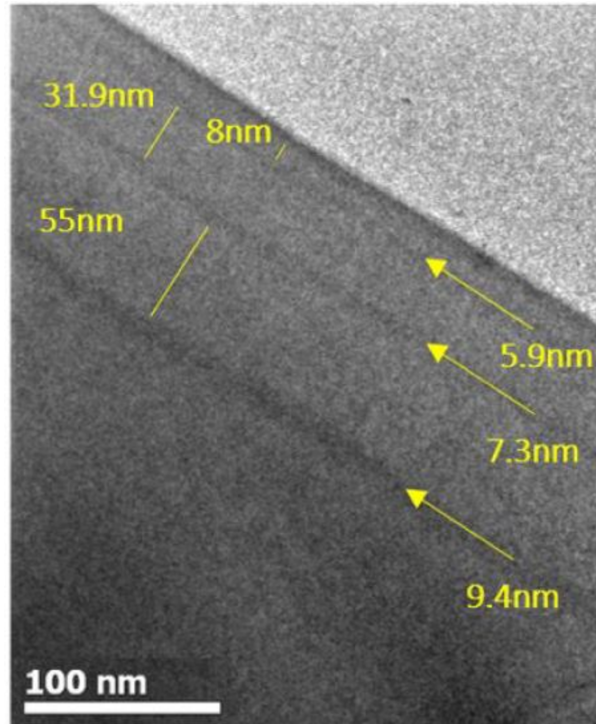

Figure 3.8: (Color online) Transmission electron micrograph of the multiple quantum well structure.

to measure a spectra similar to the one reported in Fig. 3.6 at 77 K. Due to factors outside of the work group the study had to stop in order to focus on other projects. This very promising project is therefore still open to future developments with the initial next steps described here earlier.

Author Contributions

Kevin D. Vallejo was the lead grower for this study. In addition he contributed the literature review, sample preparation and shipping, XRD, TEM sample preparation and imaging, Mathematica code design and implementation, Raman spectroscopy, as well as manuscript writing and data analysis.

CHAPTER 4:

INDIUM ARSENIDE (111)A HOMOEPITAXY

Kevin D. Vallejo, Trent A. Garrett, Kathryn E. Sautter, Kevin Saythavy, Baolai Liang, and Paul J. Simmonds

Reproduced from *J. Vac. Sci. Technol. B (2020), 37(6), 061820-1*, with the permission of AIP Publishing.

4.1 Introduction

We have established a robust set of growth conditions for homoepitaxy of high quality InAs with a (111)A crystallographic orientation by molecular beam epitaxy (MBE). By tuning substrate temperature, we obtain a transition from a 2D island growth mode to step-flow growth. Optimized MBE parameters (substrate temperature = 500 °C, growth rate = 0.12 ML/s and V/III ratio $\geqslant$ 40) lead to growth of extremely smooth InAs(111)A films, free from hillocks and other 3D surface imperfections. We see a correlation between InAs surface smoothness and optical quality, as measured by photoluminescence spectroscopy. This work establishes InAs(111)A as a platform for future research into other materials from the 6.1 Å family of semiconductors grown with a (111) orientation. In recent years, there has been renewed interest in epitaxial growth on the (111) surfaces of III-V semiconductors. This resurgence is driven by the unique properties of this crystallographic orientation, which are attractive for a

range of emerging technologies [42]. High quality, (111)-oriented material is needed for transistors where electron transport occurs in both Γ and L valleys [43]; quantum dots with negligible fine-structure splitting for entangled photon sources [44, 45]; V_2–VI_3 topological insulators whose crystalline quality benefits from the threefold symmetry of the (111) surface [46, 47]; and transition metal dichalcogenides and other 2D materials since the (111) surfaces lend themselves well to van der Waals epitaxy [48, 49].

Before we can unlock the full of potential of (111) surfaces, we must first overcome the challenge of growing semiconductors with this orientation, since growth on (111) is frequently more difficult than growth on traditional (001) substrates. The formation of large 3D hillocks during molecular beam epitaxy (MBE) can impair the optical and electronic properties of these materials [42]. As the result of considerable research efforts, high-quality, (111)-oriented materials can now be grown on some of the most commonly used III-V substrates. Growth conditions have been optimized for the A and B faces of GaAs(111) [50, 51, 52, 53, 54, 55, 56, 57]. Similarly, several papers explore the MBE parameters for homoepitaxy of InP(111), as well as for heteroepitaxy of its technologically relevant lattice-matched alloys, $In_{0.52}Al_{0.48}As$ and $In_{0.53}Ga_{0.47}As$ [45, 58, 59, 11].

In contrast, few studies exist concerning the growth of InAs(111)A [60, 61, 62, 63]. Reference [60] demonstrates rough InAs(111)A surfaces covered in a high density of hillocks, while references [62, 64] grew only very thin films (¡ 30 nm) for low-temperature scanning tunneling microscopy, which would not be thick enough for future device structures. A systematic study of the effects of MBE growth conditions on InAs(111)A morphology and material quality has not yet been reported.

Establishing the MBE growth of InAs(111)A would open up research areas requiring (111)-oriented growth with lower band gaps than can be reached with the GaAs and InP materials systems. In addition, growth of high-quality InAs(111)A would provide access to other (111)-oriented semiconductors in the 6.1 Å materials family [65]. With a lattice constant of 6.058 Å, InAs is almost lattice matched to GaSb and AlSb (6.096Å and 6.136 Å respectively), as well as to several II-VI semiconductors. Monolithic integration of these 6.1Å materials on (111) surfaces would create the opportunity for developing heterostructures with previously unavailable functionalities [65].

In this paper we add InAs(111)A to the list of III-V substrates for which homoepitaxial growth conditions have been comprehensively studied. We determine the MBE growth conditions required for minimizing surface roughness and maximizing material quality. We show that the growth of InAs(111)A is particularly sensitive to careful choice of substrate temperature.

4.2 Methods

Using an indium effusion cell and a valved As_4 source, we use MBE to grow InAs on pieces of undoped InAs(111)A substrate. We use As_4 for consistency with existing literature reports, most of which use this As species [60, 63]. Since (111)A substrates cleave preferentially along the $[\bar{1}10]$, $[10\bar{1}]$ and $[0\bar{1}1]$ directions, the resulting pieces are triangles and parallelograms, which are incompatible with indium-free sample holders. We therefore use high-purity indium metal to mount the cleaved InAs(111)A pieces onto molybdenum blocks, an approach that provides excellent temperature uniformity across the sample. We monitor substrate temperature, T_{sub}, using a thermocouple behind the substrate and an infrared pyrometer, calibrated against known changes

in surface reconstruction using reflection high-energy electron diffraction (RHEED). We remove the InAs surface oxide by heating the substrate under As_4 to $T_{sub} = 495$ °C, annealing it for 600 s, and then annealing at 500 °C for a further 180 s. We then adjust T_{sub} to the required growth temperature. After oxide desorption, RHEED shows a clear (2×2) surface reconstruction. Using RHEED intensity oscillations performed on the (001) surface, we calculate growth rates on (111)A in monolayers per second (ML/s).

To identify optimal MBE conditions for InAs(111)A homoepitaxy, we grew three experimental series, each sample consisting of 100 nm InAs, to explore the effects of: i) T_{sub} from 380–520 °C; ii) InAs growth rate from 0.06–0.24 ML/s; and iii) and As_4/In V/III atomic flux ratio from 12 to 48. For a given In flux in atoms $cm^{-2}s^{-1}$, we find the equivalent atomic As flux by reducing the As until we see a transition from the As-stabilized (2x4) reconstruction to the In-stabilized (4x2) reconstruction on InAs(001). We use multiples of the corresponding As beam equivalent pressure to obtain any desired V/III atomic flux ratio. After growth, we anneal samples under As_4 at the growth temperature for 180 s to promote surface smoothing [63], before cooling under As_4. We characterize InAs surface morphology using atomic force microscopy (AFM), and calculate the root mean square roughness, R_q, from 1×1 μm^2 AFM images (unless otherwise noted). We characterize material quality using room-temperature photoluminescence (PL) spectroscopy. We also explored the use of x-ray diffraction and Raman spectroscopy to measure crystal quality. However, these techniques did not provide sufficient resolution to distinguish between the best and worst of the samples in this study, and so the results are not discussed here. All error bars in this study show the standard deviation across multiple measurements,

divided by the square root of the number of measurements.

4.3 Results

4.3.1 Substrate Temperature Variation

InAs(111)A material quality is strongly dependent on T_{sub}, with both surface morphology and PL intensity optimized in the range 470–500 °C.

We grew a series of InAs(111)A samples at T_{sub} = 380, 410, 440, 470, 500, and 520 °C, while holding the growth rate and V/III ratio constant at 0.12 ML/s and 24 respectively. At $T_{sub} \leq 440$ °C, growth proceeds by the formation of 2D flat, monolayer-high islands that show no preferential growth direction (Figs. 5.1(a)–(c)). Between T_{sub} = 470 °C and 500 °C, we see a transition from layer-by-layer growth to step-flow growth, with the formation of long terraces (Figs. 5.1(d)–(e)). As well as this change in growth mode, raising T_{sub} from 380 °C to 500 °C also smooths the InAs(111)A surface, lowering R_q from 4.9 Å to 1.4 Å . However, increasing T_{sub} further, to 520 °C, has the opposite effect, roughening the InAs(111)A surface, predominantly as a result of step-bunching (Fig. 5.1(f)).

Samples grown at $T_{sub} \geq 440$ °C exhibit a twofold increase in PL intensity, compared to samples grown at lower temperature (Fig. 5.1(g)). Defects such as dislocations and mid-gap trap states can act as non-radiative recombination centers, reducing PL intensity. The brighter PL we see for $T_{sub} \geq 440$ °C, therefore suggests that the material quality is enhanced in samples grown at higher temperature.

Fig. 5.1(h) illustrates that we can obtain extremely smooth InAs(111)A and bright PL emission simultaneously. From these results, one should grow InAs(111)A at T_{sub} = 470–500 °C for optimal material quality.

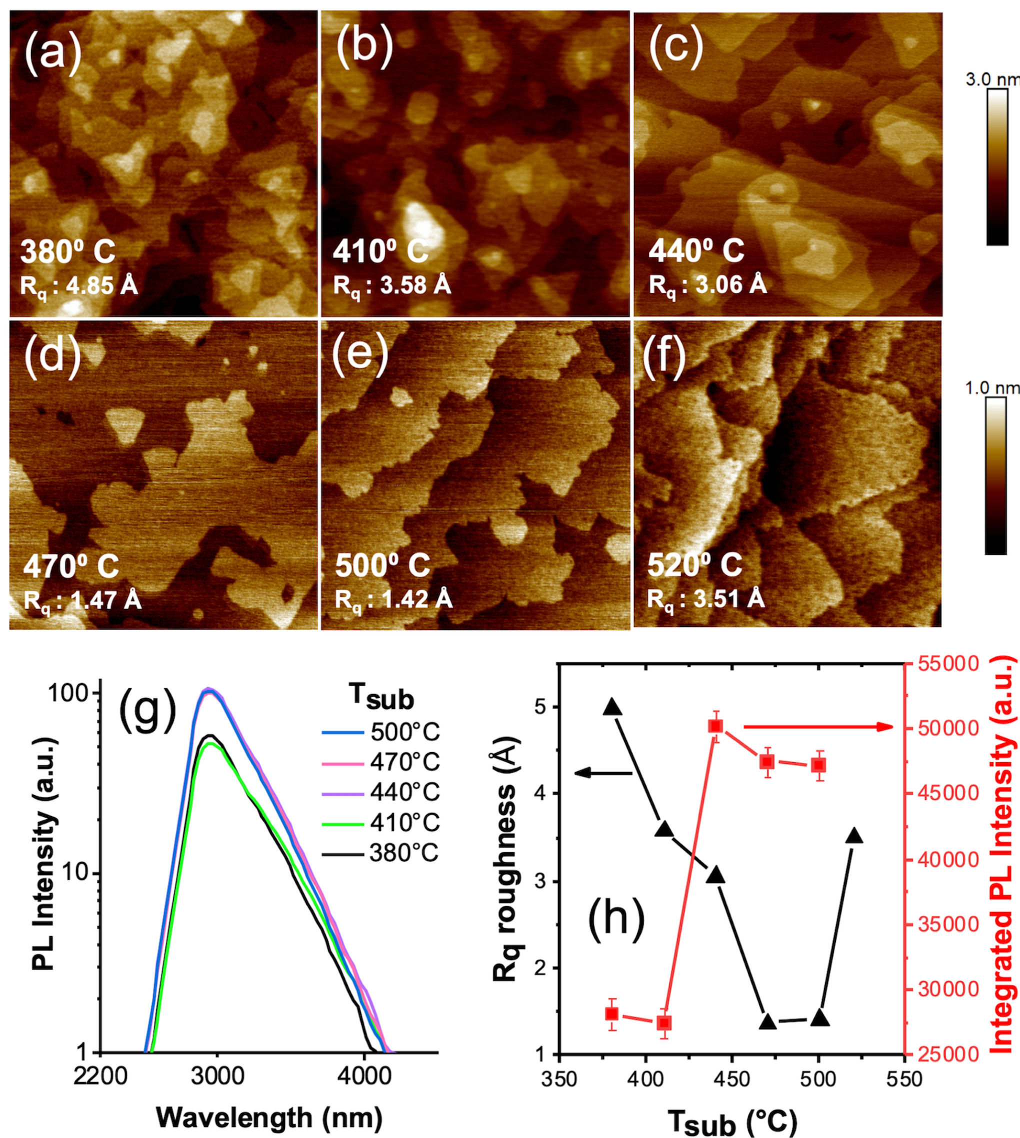

Figure 4.1: (a)-(f) 1μm $\times$ 1μm AFM micrographs showing the effect of T_{sub} on InAs(111)A surface morphology. Height for (a)-(c) is 3 nm while for (d)-(f) it is 1 nm. All samples were grown at 0.12 ML/s, with a V/III ratio of 24. A dramatic decrease in R_q surface roughness above $T_{sub} = 440$ °C, is accompanied by a transition from island growth to step-flow growth. (g) InAs(111)A PL spectra as a function of T_{sub}. PL is brighter for samples grown at higher temperature, consistent with improved material quality. (h) Triangles show R_q (over a 1 μm^2 area) as a function of T_{sub}, with roughness minimized at 470–500 °C. Squares show the integrated intensity of the PL spectrum for each T_{sub} sample. We see a sharp increase in light emission intensity above $T_{sub} = 410$ °C.

4.3.2 Growth Rate Variation

InAs(111)A material quality is weakly dependent on InAs growth rate (GR), with both surface smoothness and PL intensity optimized in the range 0.06–0.12 ML/s.

We grew a series of InAs(111)A samples with growth rates of 0.06, 0.12, and 0.24 ML/s, while holding T_{sub} at 500 °C, based on the results above. For each sample, we adjusted the As_4 flux to maintain a constant V/III ratio of ∼24.

All three samples exhibit a step-flow morphology. Looking at 5×5 μm^2 areas of the samples, R_q roughness decreases monotonically with increasing growth rate (Fig. 5.2(a)-(c)). However, at higher magnification (insets to Fig. 5.2) the sample grown at 0.12 ML/s shows the smoothest surface due to its long terraces, $\sim 1\mu$m wide).

The 0.06 ML/s and 0.12 ML/s samples show almost identical PL emission, with a slight decrease in intensity for the sample grown at 0.24 ML/s (Fig. 5.2(d)). The small reduction in PL intensity suggests that at higher growth rate, shorter adatom migration lengths may introduce point defects, so that material quality starts to suffer.

Fig. 5.2(e) shows that by growing more slowly, we can optimize InAs(111)A surface smoothness and optical quality at the same time. Given that surface morphology of the sample grown at 0.12 ML/s presents the lowest roughness and bright optical emission, we recommend using this growth rate.

4.3.3 V/III Ratio Variation

InAs(111)A material quality is weakly dependent on V/III flux ratio, with surface smoothness and PL intensity optimized in the range 24–48.

We grew a series of InAs(111)A samples with V/III flux ratios of 12, 24, and 48, while holding T_{sub} and growth rate constant at 500 °C and 0.12 ML/s respectively,

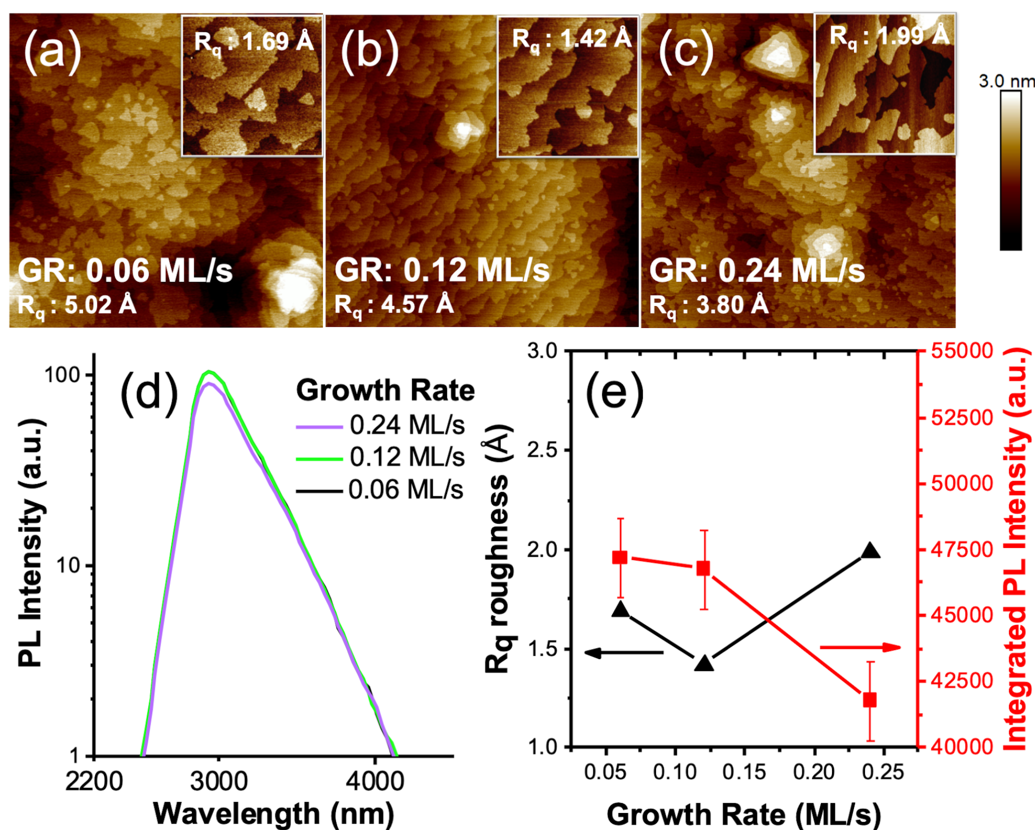

Figure 4.2: (Color online) (a)-(c) AFM micrographs showing the effect of InAs(111)A growth rate on surface morphology. All samples were grown at 500 °C, with a V/III ratio of 24. Large figures are 5×5 μm^2 scans with a height of 3 nm, with insets of 1×1 μm^2 and height of 1 nm. (d) InAs(111)A PL spectra as a function of sample growth rate. These spectra are similar in intensity, indicating that InAs(111)A optical quality is only weakly dependent on growth rate. (e) Triangles show R_q (over a 1 μm^2 area) as a function of InAs(111)A growth rate, with the lowest roughness occurring at 0.12 ML/s. Squares show the integrated intensity of the PL spectrum for each growth rate. PL intensity decreases at the highest growth rate, and the surface becomes rougher.

based on the results above.

At a V/III ratio of 12, we observe the growth of ”wedding cakes” (concentric stacks of 2D islands), $\sim$ 7 nm tall, across the sample surface. Increasing the the V/III ratio to 24 produces a significantly smoother surface, where a step-flow growth can be seen around the wedding cakes. For V/III ratios $\sim$ 48, InAs(111)A growth transitions fully into a step flow mode with atomically flat terraces, $\sim$ 1 μm wide (Fig. 5.3(a)-(c)).

PL intensity declines slightly with increasing V/III ratio, over the range studied here, which could indicate a reduction in material quality, possibly due to the formation of As antisite defects. Alternatively, it is possible that as the InAs becomes extremely smooth (Fig. 5.3(c)), outcoupling of photons from the sample is reduced, lowering the measured PL intensity [66]. The PL intensities of the three samples measured are within 1.5 standard deviations of each other (Fig. 5.3(e)). To put this in context, the standard deviation of the intensity from these three samples' intensity is comparable to the difference in intensity we see between PL measurements done at different locations on the same sample.

Plotting InAs(111)A R_q and integrated PL intensity as a function of V/III ratio (Fig. 5.3(e)), the situation differs from what we saw for T_{sub} (Fig. 5.1(h)) and InAs growth rate (Fig. 5.2(e)). For the V/III ratio series, there does not seem to be an analogous correlation between smoother surfaces and enhanced material quality. However, since the optical quality seems to remain fairly high regardless of the V/III ratio used, it makes sense to optimize V/III ratio in order to achieve the smoothest InAs(111)A, and so we recommend V/III flux ratios of $\sim$ 48.

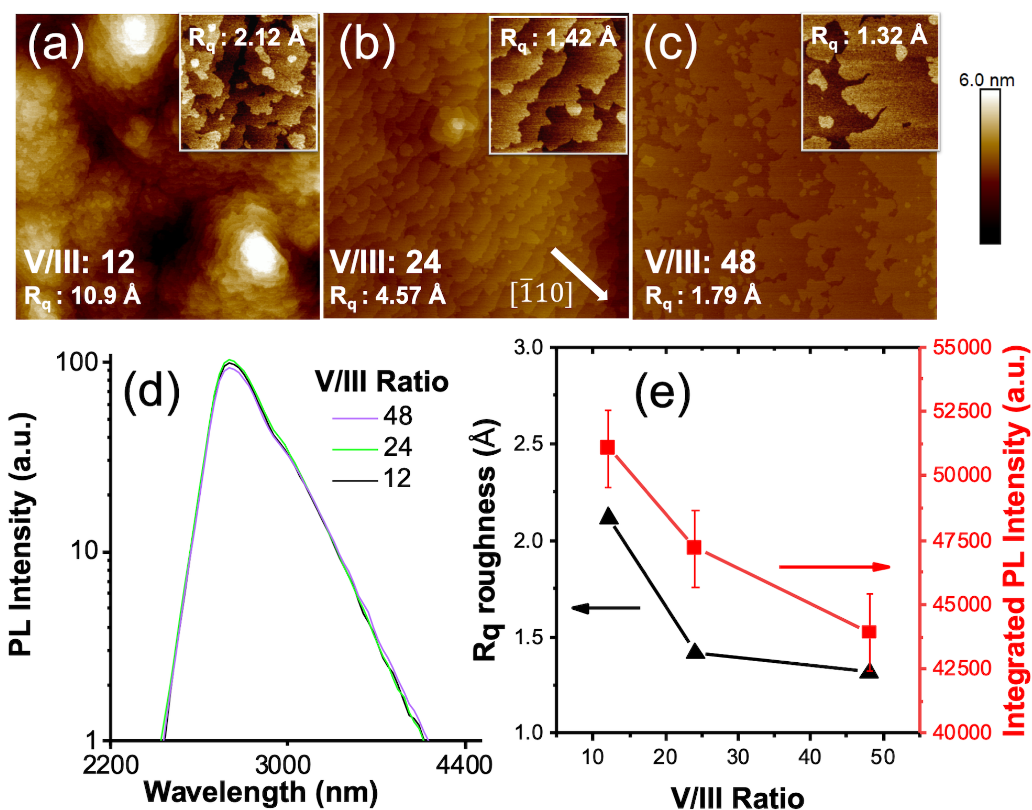

Figure 4.3: 5×5 μm^2 **AFM micrographs showing the effect of V/III ratio on surface morphology. All samples were grown at 500 °C, with a growth rate of 0.12 ML/s. Large images have a height of 6 nm, with insets of 1×1 μm^2 and height of 1 nm. For V/III $\geqslant$ 12, we see smooth InAs(111)A surfaces and the formation of regularly spaced terraces aligned perpendicular to the $[\bar{1}10]$ direction. (d) InAs(111)A PL spectra as a function of V/III ratio. The spectra are reasonably close in intensity, indicating limited dependence of V/III ratio on InAs(111)A optical quality. (e) Triangles show R_q (over a 1 μm^2 area) as a function of V/III ratio, showing that ratios above 24 result in the smoothest film growth. Squares show the integrated intensity of the PL spectrum for each V/III ratio sample. Although there is a small downward trend with increased V/III ratio, the magnitude of the change is almost within the measurement error.**

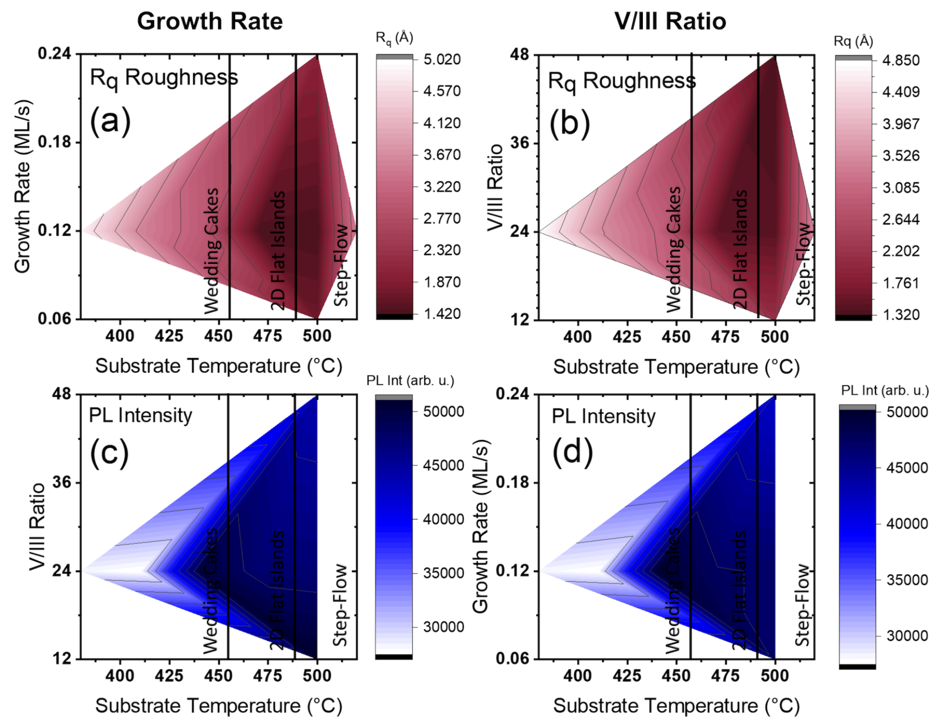

Figure 4.4: (Color online) Contour plots of R_q roughness as function of (a) growth rate and T_{sub}, (b) V/III ratio and T_{sub}. Contour plots of integrated PL intensity as function of (c) growth rate and T_{sub}, and (d) V/III ratio and T_{sub}. Deeper color hues indicate improved material parameters: darker magenta and blue indicate smoother surface and higher PL intensity, respectively.

4.3.4 Summary of growth conditions

Fig. 5.4 summarizes the MBE conditions that lead to smooth, high-quality homoepitaxial InAs(111)A. Figs. 5.4(a)–(b) show how surface roughness is minimized at T_{sub} = 475–500 °C when we use a growth rate of 0.12 ML/s and V/III ratios of 24–48. Figs. 5.4(c)–(d) show that PL intensity is also brightest when these growth conditions are used, confirming that we can simultaneously optimize both InAs(111)A surface morphology and optical quality.

4.4 Conclusions

We have established a set of MBE growth parameters that yields exceptionally smooth InAs(111)A homoepitaxial films with atomically flat terraces, ~ 1 μm in width, and optimal optical quality. The ability to grow smooth, high-quality InAs(111)A films opens up opportunities for research into other 6.1 Å semiconductors that share this technologically relevant surface orientation.

Author Contributions

Kevin D. Vallejo was the lead grower for this study: designing, programming and growing the samples. In addition he contributed the literature review, sample preparation and shipping, XRD, as well as data gathering, analysis, and manuscript preparation.

CHAPTER 5:

TENSILE-STRAINED SELF-ASSEMBLY OF INDIUM GALLIUM ARSENIDE ON INDIUM ARSENIDE (111)A

Kevin D. Vallejo, Trent A. Garrett, Carlos I. Cabrera, Baolai Liang, Kevin Grossklaus, and Paul J. Simmonds

Reproduced from *J. Vac. Sci. Technol. B (2021), XX(X), XXXXX-X*, with the permission of AIP Publishing.

Interest in III-V semiconductors with a (111) orientation has increased in recent years. The unique structural and electronic properties of semiconductors with this crystallographic orientation are the main driver behind this renewed interest [42]. The symmetry of the (111) surface means these III-V materials are well-suited to integration with 2D materials such as transition metal dichalcogenides [48, 49], V_2–VI_3 topological insulators [46, 47], and certain IV-VI rocksalt semiconductors such as PbSe [67]. Transistors with a (111) orientation may offer ballistic electron transport in both Γ and L valleys, to overcome the density of states bottleneck [43]. Quantum dots (QDs) with a (111) orientation have negligible fine-structure splitting, making them ideal entangled photon sources [44, 45].

For this latter application, Stranski-Krastanov (SK) self-assembly of QDs on (111) surfaces must be driven by tensile strain [68]. The specific combination of tensile strain and surface orientation creates an energy barrier to dislocation nucleation and glide, resulting in the spontaneous formation of defect-free QDs [56, 57, 3]. The presence of residual tensile strain in the self-assembled QDs also modifies their properties, lending them some unusual characteristics. Tensile strain breaks the valence band degeneracy, lifting the light-hole band above the heavy-hole band [69], and raising the prospect of light-hole exciton formation in QDs for quantum media conversion applications [70]. Tensile strain also reduces the semiconductor band gap energy (E_g), pushing QD light emission and absorption towards the infrared (IR) [71, 45, 72, 11, 68]. This reduction in E_g typically exceeds the increase in the QD ground state transition energy that comes from quantum confinement. The result is light emission below the band edge of the bulk material from which the QDs are composed [71, 45, 72, 68].

The ability to grow QDs with red-shifted light emission presents us with an opportunity to create novel optoelectronic devices for IR applications. By synthesizing tensile-strained QDs from III-V semiconductors such as $In_{1-x}Ga_xAs$ that have a narrow bulk band gap, we could in principle engineer highly tunable mid-IR light sources. Laser devices based on self-assembled QDs (e.g., Ref. Norman2019) are significantly quicker, easier and cheaper to grow than quantum cascade structures [73].

In this paper we explore the self-assembly of tensile-strained $In_{1-x}Ga_xAs$ QDs by molecular beam epitaxy (MBE) on InAs(111)A. This is a rich material system: changing the Ga content, x, adjusts both the $In_{1-x}Ga_xAs$ band gap and the amount of tensile strain due to lattice mismatch with the InAs matrix. Raising x *increases* E_g in $In_{1-x}Ga_xAs$, but also increases the tensile strain, which serves to simultaneously

reduce E_g. When we combine these composition-related effects with the additional degree of freedom that comes from quantum confinement, it is easy to see just how tunable the band structure of tensile $In_{1-x}Ga_xAs$ QDs could be.

A few research groups have previously explored tensile-strained GaAs and $In_{0.5}Ga_{0.5}As$ QDs and quantum wells (QWs) [74, 75, 76, 77]. Those reports all focused on GaSb(001) as the substrate material. Despite the fact that efficient tensile strain relief can be an issue for achieving defect-free self-assembly on (001) surfaces [57, 78], these researchers were able to demonstrate QD and QW light emission in the $2 - 2.3$ μm range by keeping the nanostructures small [74, 75, 76]. More recent studies show that moving from (001) to (111) substrates will give us more flexibility in QD size, since dislocation formation is retarded in (111)-oriented semiconductors under tensile strain [56, 57].

We therefore use InAs substrates with a (111)A orientation to help minimize plastic relief of the tensile strain. Our choice of InAs instead of GaSb allows us to use arsenic as a common anion for both the QD and matrix. This means we can cap the QDs immediately without the need for complex shutter sequences at the III-As / III-Sb interfaces, which helps minimize any QD annealing effects [79]. We investigate how one can control the size and areal density of the self-assembled $In_{1-x}Ga_xAs$/InAs(111)A QDs as a function of their composition and MBE growth conditions. We use a combination of computational modeling and photoluminescence (PL) to explore the electronic structure of these QDs. This work sets the stage for future studies of the optical properties of tensile-strained $In_{1-x}Ga_xAs$(111) QDs.

5.1 Methods

All samples were grown via solid-source MBE on unintentionally doped, nominally on-axis (± 0.5 °) InAs(111)A substrates. We use high-purity indium metal to mount the InAs(111)A substrates onto molybdenum blocks, which ensures excellent temperature uniformity across each sample. We monitor substrate temperature (T_{sub}) using a thermocouple behind the substrate and an infrared pyrometer, calibrated by reflection high-energy electron diffraction (RHEED) against known changes in surface reconstruction. We calculate growth rates in monolayers per second (ML/s) on (111)A from RHEED intensity oscillations performed on the (001) surface. We calibrate the composition of the $In_{1-x}Ga_xAs$ layers using RHEED intensity oscillations and *ex-situ* X-ray diffraction.

We begin by heating the InAs(111)A substrates under As_4 to T_{sub} = 495 °C to remove the native oxide. We use As_4 for consistency with previous studies of InAs(111)A homoepitaxy [80, 60, 63]. We then anneal the substrate for 600 s at this temperature, followed by a further annealing step at 500 °C for 180 s. After oxide removal and annealing, the RHEED shows a bright (2×2) surface reconstruction. To smooth the substrate surface, we grow a 100 nm InAs buffer at T_{sub} = 500 °C, with a growth rate of 0.12 ML/s and an As_4/In flux ratio of 48. We have optimized these conditions for InAs(111)A homoepitaxy previously [80].

We then adjust T_{sub} and cell temperatures as required for a specific deposition of $In_{1-x}Ga_xAs$/InAs(111)A experiment. In this study, we explore $In_{1-x}Ga_xAs$ coverage from 2–4 ML, $In_{1-x}Ga_xAs$ composition from $x = 0.25 - 1.00$, and T_{sub} from $410 - 500$ °C. Depending on the purpose of the experiment, the $In_{1-x}Ga_xAs$ QDs are either left exposed for atomic force microscopy (AFM), or buried with an InAs capping layer for

photoluminescence (PL) spectroscopy. We grew all $In_{1-x}Ga_xAs$ layers at 0.4 ML/s, adjusting the In and Ga fluxes according to the alloy composition. During the transition between layers there is no change or pause other than the minimum required to change the substrate temperature and Ga, In, or As flux when required by the different growth series.

We use NanoScope software to analyze multiple AFM images of surface $In_{1-x}Ga_xAs$ QDs from each sample to find the average QD height, diameter, and areal density. We calculate error bars for each parameter by dividing the standard deviation of each parameter population by the square root of the number of QDs measured, which amount to the total visible QDs in each AFM scan [81]. We examine the structure, morphology, and compositional distribution of our samples using cross-sectional bright-field transmission electron microscopy (TEM), and scanning TEM (STEM) combined with electron energy loss spectroscopy (EELS) to map material composition. We prepare TEM samples using a focused ion beam lift-out method and characterize them in a JEOL 200F ARM operating at 200 kV. All TEM images, STEM images, and EELS maps were taken with the samples tilted to align the electron beam to a [110] zone-axis.

5.2 Results and Discussion

Fig. 5.1 shows a matrix of AFM images from the full set of $In_{1-x}Ga_xAs$ on InAs(111)A samples we grew. Moving from left to right corresponds to increasing the Ga content (x) of the $In_{1-x}Ga_xAs$ layer, while moving from top to bottom corresponds to increasing the InGaAs coverage. Below we discuss some of the trends revealed in this matrix.

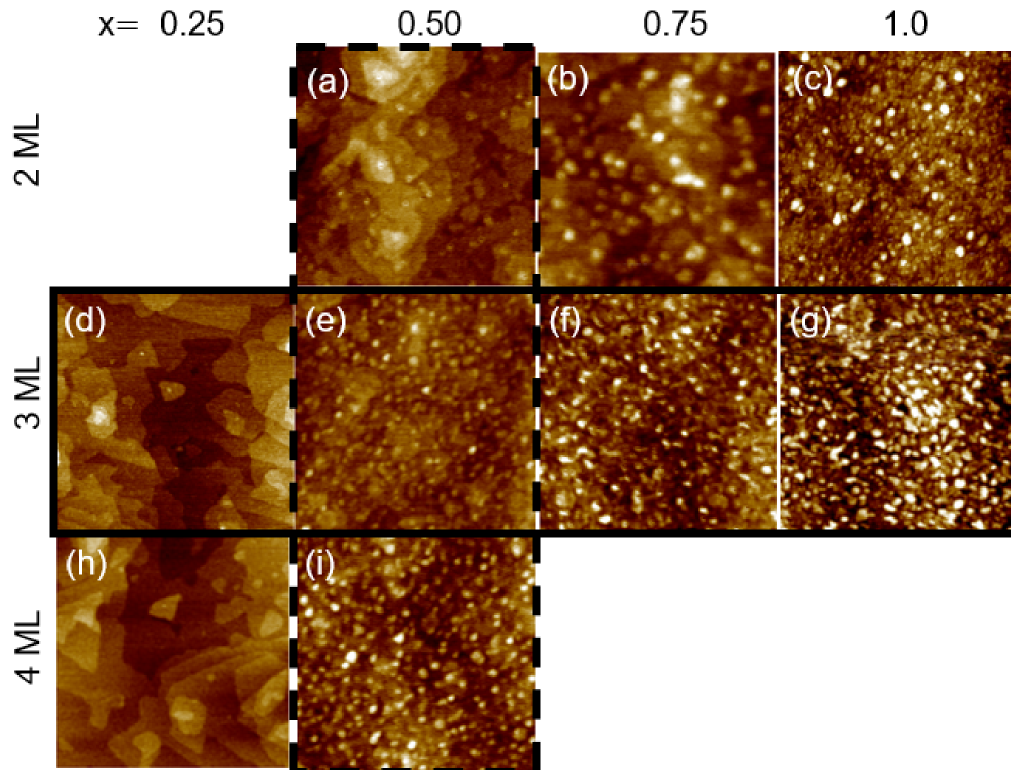

Figure 5.1: 500 nm $\times$ 500 nm AFM micrographs showing the evolution of surface morphology after deposition of $2-4$ ML $In_{1-x}Ga_xAs$, with Ga concentrations of $x = 0.25, 0.5, 0.75$ and 1.0. We grew all samples at $T_{sub} = 410$ °C. The z-scale is 3 nm for all images. The dashed outline highlights the ML coverage series for $In_{0.5}Ga_{0.5}As$ (Sec. 5.2.1). The solid outline highlights the $In_{1-x}Ga_xAs$ composition series for 3 ML coverage (Sec. 5.2.2).

5.2.1 $In_{0.5}Ga_{0.5}As$/InAs(111)A coverage series

The column with the dashed outline in Fig. 5.1 highlights a series of $In_{0.5}Ga_{0.5}As$ samples grown at $T_{sub} = 410°C$ where we increase the coverage from 2 to 4 ML. We focus on this series in Fig. 5.2.

The sample grown with 2 ML $In_{0.5}Ga_{0.5}As$ exhibits a comparatively smooth surface, for which flat 2D islands are the predominant morphological feature (Fig. 5.2(a)). Prohl *et al.* reported previously that nucleation of InAs on GaAs(001) can occur at deposition amounts lower than 1.6 ML on defects and hollow sites of the c(4×4) GaAs reconstruction. The few seemingly already-assembled island visible on Fig. 5.2(a) do not provide enough information to quantify their morphological features with statistical significance. When we raise the coverage to 3 ML, we observe a dramatic change in the morphology, such that the surface is covered in self-assembled 3D InGaAs QDs (Fig. 5.2(b)). This 2D-to-3D transition is a hallmark of the SK growth mode. The tensile lattice mismatch between $In_{0.5}Ga_{0.5}As$ and InAs(111)A is 3.3 %, with the critical thickness for SK growth lying between 2 and 3 ML (Figs. 5.2(a)-(b)). A critical thickness in this range is consistent with the $2 - 2.5$ ML reported for the InAs/InAlAs(001) QD system that has a compressive mismatch of 3.2 % [82, 83]. By staying below this critical thickness, we can therefore produce 2D $In_{0.5}Ga_{0.5}As$ QWs under large tensile strains, with potential IR optoelectronic applications [75]. As we raise the $In_{0.5}Ga_{0.5}As$ coverage from 3 ML to 4 ML, the 3D QDs increase in average height (0.57 ± 0.03 to 0.69 ± 0.14 nm), average diameter (7.9 ± 0.2 to 8.7 ± 1.0 nm), and areal density (2.3 to 6.8×10^{11} cm^{-2}) (Fig. 5.2(c)).

We can tune the critical thickness for the SK growth mode by modifying the magnitude of the tensile strain. The presence of QDs in Figs. 5.1(b)$-$(c) means

that the transition to 3D self-assembly has already occurred by the time we have deposited 2 ML InGaAs. $In_{0.25}Ga_{0.75}As$ and GaAs are lattice mismatched to InAs by 5.0 % and 6.7%, respectively. Compared with the $In_{0.25}Ga_{0.75}As$ sample in Fig. 5.1(a), the resulting increase in tensile strain in these cases has reduced the critical thickness below 2 ML. Again, this is consistent with other highly strained SK systems such as InAs/GaAs(001) QDs where 7.2 % compressive lattice mismatch results in a critical thickness of $\sim$ 1.6 ML [84]. In general, the higher the strain, the lower the critical thickness for SK growth [85, 86]. The ternary nature of the tensile InGaAs QD system gives us a great deal of control in this respect.

5.2.2 $In_{1-x}Ga_xAs$/InAs(111)A composition series

The row with the black outline in Fig. 5.1 highlights a 3 ML $In_{1-x}Ga_xAs$ sample series grown at $T_{sub} = 410°C$, in which we tune the Ga concentration: $x = 0.25$, 0.50, 0.75 and 1.00. We focus on this series in Fig. 5.3.

At $x = 0.25$, the tensile strain resulting from the 1.67 % lattice mismatch between the $In_{0.75}Ga_{0.25}As$ and the InAs(111)A substrate is insufficient to drive QD self-assembly (Fig. 5.3(a)). Similarly to the discussion in the previous section for Fig. 5.2(a) these few islands do not provide enough information to accurately describe their morphology. Indeed, Fig. 5.1(h) shows that the surface remains flat, even after 4 ML $In_{0.75}Ga_{0.25}As$ deposition. As we have already mentioned, the ability to grow smooth tensile-strained InGaAs layers could be useful for QW-based IR optoelectronics [75].

As we raise x, we reduce the $In_{1-x}Ga_xAs$ lattice constant. The result is a greater lattice mismatch with the InAs(111)A substrate and hence higher tensile strain. For a Ga concentration of $x = 0.5$, the tensile strain is large enough to produce spontaneous

QD formation from 3 ML coverage (Fig. 5.3(b)). As we further increase the Ga concentration to $x = 0.75$ (Fig. 5.3(c)) and then $x = 1.0$ (Fig. 5.3(d)), we see that the 3 ML $In_{1-x}Ga_xAs$ QDs become larger and more densely packed. InGaAs QD areal density increases by almost six times (2.32 to 13.6×10^{11} cm^{-2}) as we raise x from 0.5 to 1.0 (Fig. 5.3(e)), with smaller increases in QD height and diameter over the same compositional range (Fig. 5.3(f)).

That we see larger, higher density QDs in Figs. 5.3(e)−(f) for a constant InGaAs coverage of 3 ML confirms our finding from the InGaAs coverage series that critical layer thickness is dependent on the strain. Because tensile strain increases as we raise x, the critical thickness required for the 2D-to-3D SK transition is reduced [86, 85, 3]. A thinner wetting layer means that a greater proportion of the 3 ML InGaAs will end up in the 3D QDs, and so their size and areal density increase accordingly.

5.2.3 $In_{0.5}Ga_{0.5}As$/InAs(111)A substrate temperature series

We use a third set of samples to explore how T_{sub} affects the morphology of 3 ML $In_{0.5}Ga_{0.5}As$ QDs (Figs. 5.4(a)–(d)). As we raise T_{sub} from 410 °C to 500 °C, the areal density of the $In_{0.5}Ga_{0.5}As$ QDs decreases by almost 20× from (2.32 to 0.12×10^{11} cm^{-2}) (Fig. 5.4(e)).

The ability to tune QD density by as much as an order of magnitude with InGaAs composition (i.e., tensile strain) (Fig. 5.3(e)) and T_{sub} (Fig. 5.4(e)) is desirable for future optoelectronic applications. High QD density is suited to high intensity photon emission for LEDs/lasers, while low QD density is appealing for single-photon generation where light collection from individual QDs is needed.

As we raise T_{sub} over the same range, the average diameter of the InGaAs QDs increases monotonically by a factor of three (Fig. 5.4(f)). Average QD height also

initially increases, peaking at $\sim$ 440 °C (Fig. 5.4(f)). These trends are consistent with ripening effects observed in previous studies of both compressive- and tensile-strained QD systems [87, 56]. As we increase T_{sub}, adatom surface diffusion length is enhanced, resulting in the formation of large, low density QDs that are more efficient at minimizing the strain energy than small, high density QDs. However, further raising T_{sub} to 470–500 °C, reduces the average QD height. These observations indicate the formation of larger, flatter InGaAs islands (Fig. 5.4(d)) at high T_{sub}. A similar temperature-dependence of QD aspect ratio has been seen during SK growth of tensile-strained GaAs/InAlAs(111)A QDs [11], and droplet epitaxy of InAs/GaAs(111)A QDs [88], where it was attributed to longer adatom diffusion and an enhanced ability for adatoms to migrate from the tops of islands to the terrace below.

5.2.4 Transmission Electron Microscopy of $In_{0.5}Ga_{0.5}As$

We used cross-sectional TEM to examine 3ML and 4ML $In_{0.5}Ga_{0.5}As$ QDs grown at 410 °C, i.e., equivalent to those in Figs. 5.2(b) and (c) but capped with InAs. We used low magnification TEM to survey wide areas of these samples and examine their film quality (Fig. 5.5), and strain contrast from the presence of the InGaAs QD and wetting layers is visible at the interface between the InAs buffer and cap layers. For the 3 ML sample, we see that the InAs capping layer is free of threading dislocations originating at the $In_{0.5}Ga_{0.5}As$ QD layer (Fig. 5.5(a)). This lack of defects indicates that tensile strain in the 3 ML InGaAs QDs is not high enough to cause widespread relaxation. We do however see several defect types originating in the substrate, in the InAs buffer, and at the interface between the two. These defects and strain contrast visible along that interface are unrelated to the InGaAs QDs and instead suggest

that the quality of the InAs(111)A substrate itself, as well as the pregrowth surface treatment, were not fully optimized for these specific samples.

When we raise the $In_{0.5}Ga_{0.5}As$ coverage to 4 ML (Fig. 5.5(b)), we see more pronounced contrast in the InGaAs layer than for the 3 ML InGaAs sample, consistent with the larger InGaAs QDs in this sample (Fig. 5.2). However, we also observe a high density of defects originating at the InGaAs layer, consistent with increased strain from the larger InGaAs QDs in this sample. This was a high enough stress to cause relaxation via widespread dislocation nucleation and glide [57]. For self-assembly of defect-free $In_{0.5}Ga_{0.5}As$ QDs, one must therefore remain below this upper deposition limit of 4 ML.

Figs. 5.6(a) and (d) show bright-field (BF) STEM images from the 3ML and 4ML InGaAs QD samples, respectively. Figs. 5.6(c) and (f) show corresponding EELS maps of the Ga L-edge signal from the boxed regions of the 3 ML and 4 ML samples in Fig. 5.6(a) and (d). Figs. 5.6(b) and (e) show high-resolution TEM images of QDs from the 3ML and 4ML samples respectively, with numbered QD locations that correspond to positions on the EELS maps.

Figs. 5.6(d)-(e) show that the strain contrast around each 4 ML QD extends much farther than the EELS map in Fig. 5.6(f) shows the actual QD size to be. Conversely, for the 3ML QD sample the apparent QD size in the BF TEM/STEM (Figs. 5.6(a)-(b)) better matches the QD size indicated by EELS mapping (Fig. 5.6(c)) because the QDs are not straining the surrounding InAs lattice as much.

We note that while both the 3ML and 4ML QDs are visible in BF TEM and BF STEM imaging modes due to their strain contrast, they are not readily visible in the annular dark-field (ADF) STEM imaging mode used concurrently with EELS

mapping. Therefore, to allow us to correlate the EELS maps with BF TEM and BF STEM images of the same areas, we intentionally chose EELS mapping locations close to easily identifiable features or defects such as that on the left hand side of Fig. 5.6(a). For the 3 ML InGaAs sample in particular, Fig. 5.5(a) shows that such defects are not representative of the crystal quality of the sample as a whole.

The EELS mapping reveals that in both samples, the InGaAs QDs have low height-to-diameter ratios, and that QD size and density increases when moving from 3 ML to 4 ML coverage. These observations are consistent with our AFM measurements of corresponding uncapped 3ML and 4ML samples in Figs. 5.2(b–c).

5.2.5 Electronic structure of $In_{1-x}Ga_xAs$/InAs(111)A QDs

Having established the MBE conditions required for defect-free growth of these novel, tensile-strained InGaAs(111)A QDs, we moved on to explore their electronic structure. Although the bulk band gap of $In_{1-x}Ga_xAs$ is larger than InAs for all compositions, we know that tensile strain can cause profound changes in semiconductor band structure [71, 45, 68, 3]. We were therefore interested to see whether for specific compositions, the tensile strain could reduce the InGaAs/InAs(111)A QDs band gap sufficiently to produce carrier confinement.

We therefore calculated the bulk band alignments of $In_{1-x}Ga_xAs$/InAs(111)A as a function of composition (Fig. 5.7). Our model accounts for the effects of tensile strain on the InGaAs band structure by using two different components, an in-plane hydrostatic term and an axial term. The hydrostatic strain acts on the band gaps of the system, while the axial component modifies the valence bands. We then calculate the energy of any confined states in the QDs by solving the Schrödinger equation for the envelope function in the effective mass approximation. For a more detailed

description of our model see Ref. schuck2019.

For $In_{1-x}Ga_xAs$ compositions $x = 0.25 - 0.75$, we obtain a type-II band structure, with a barrier in the valence band (Figs. 5.7(a)–(c)). QDs with a type-II band alignment are of interest for various optoelectronic applications due to their enhanced carrier lifetimes and the fact that their emission wavelength is tunable with excitation density [57, 89]. In contrast, for the case where $x = 1.0$, the band gap of the GaAs is too large for the tensile strain to lower the conduction band edge below that of the InAs(111)A barriers. According to these calculations, the tensile-strained GaAs forms "anti-dots" with respect to the InAs(111)A, with barriers in both the conduction and valence bands and no confined states (Fig. 5.7(d)).

For $x = 0.25$, our calculations suggest a weakly confined electron ground state in the tensile-strained QW (Fig. 5.7(a)). In the coupled WL-QD systems formed when $x = 0.5 - 0.75$, the electron ground state appears to be close to or just above the continuum of states of the InAs barriers (Fig. 5.7(b)–(c)).

We used PL spectroscopy to test these predictions of weakly confined electron states in at least some of our samples. In particular we looked for evidence of recombination between electrons confined within the $In_{1-x}Ga_xAs$ QWs or QDs and holes localized outside of the QDs in the InAs(111)A barriers. However, despite exploring a range of measurement temperatures and excitation densities, we were unable to detect any obvious light emission from the QDs. This lack of a PL signal confirms either the limitations of our model's ability to capture the effect of tensile strain on band structure, or the fact that even at 7 K, the thermal broadening of the confined states was sufficient for the electrons to escape. To overcome this issue in future, we will use this work as the basis for synthesizing these tensile-strained $In_{1-x}Ga_xAs(111)A$

QDs on barriers such as AlGaSb for which even a modest increase in band gap will ensure robust electron confinement.

5.3 Conclusions

We have established that tensile-strained $In_xGa_{1-x}As$ forms either QWs (for $x = 0.25$) or self-assembled QDs (for $x \geq 0.5$) when deposited on InAs(111)A in the range of $T_{sub} = 410 - 500$ °C. For a composition of $In_{0.5}Ga_{0.5}As$, the critical thickness for the SK-growth mode formation of these QDs lies between 2 and 3 ML. The accumulated tensile strain energy from 4 ML $In_{0.5}Ga_{0.5}As$ coverage exceeds the barrier to dislocation nucleation and glide and so plastic strain relief occurs. We can control both the density and size of the InGaAs QDs as a function of the MBE growth conditions. Our band structure calculations predict a type-II band alignment with weak electron confinement for $In_xGa_{1-x}As$(111)A QWs and QDs where $x \leq 0.75$. We anticipate that the future use of wider band gap barrier materials will allow us to demonstrate highly tunable light emission from these tensile-strained $In_xGa_{1-x}As$(111)A QDs for various IR applications.

Author Contributions

Kevin D. Vallejo was the lead grower for this study: designing, programming and growing the samples. In addition he contributed the literature review, sample preparation and shipping, XRD, as well as data gathering, analysis, and manuscript preparation.

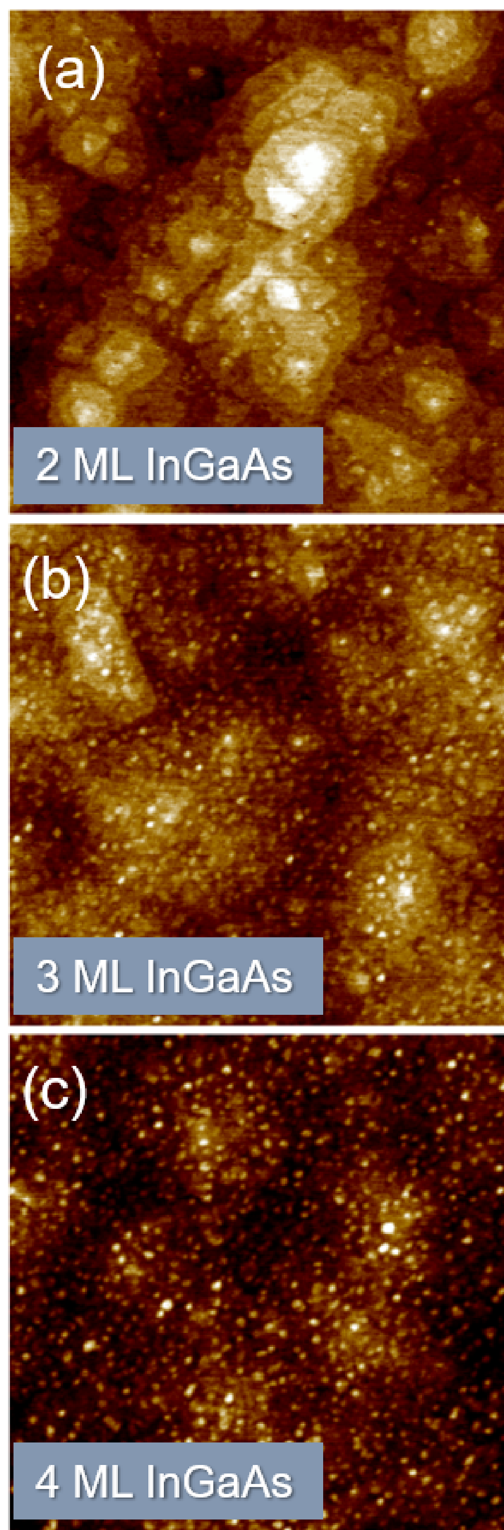

Figure 5.2: 1 μm $\times$ 1 μm AFM micrographs showing the evolution of surface morphology after deposition of (a) 2 ML, (b) 3 ML, and (c) 4 ML $In_{0.5}Ga_{0.5}As$. All samples were grown at $T_{sub} = 410$ °C. The z-scale is 3 nm for all images.

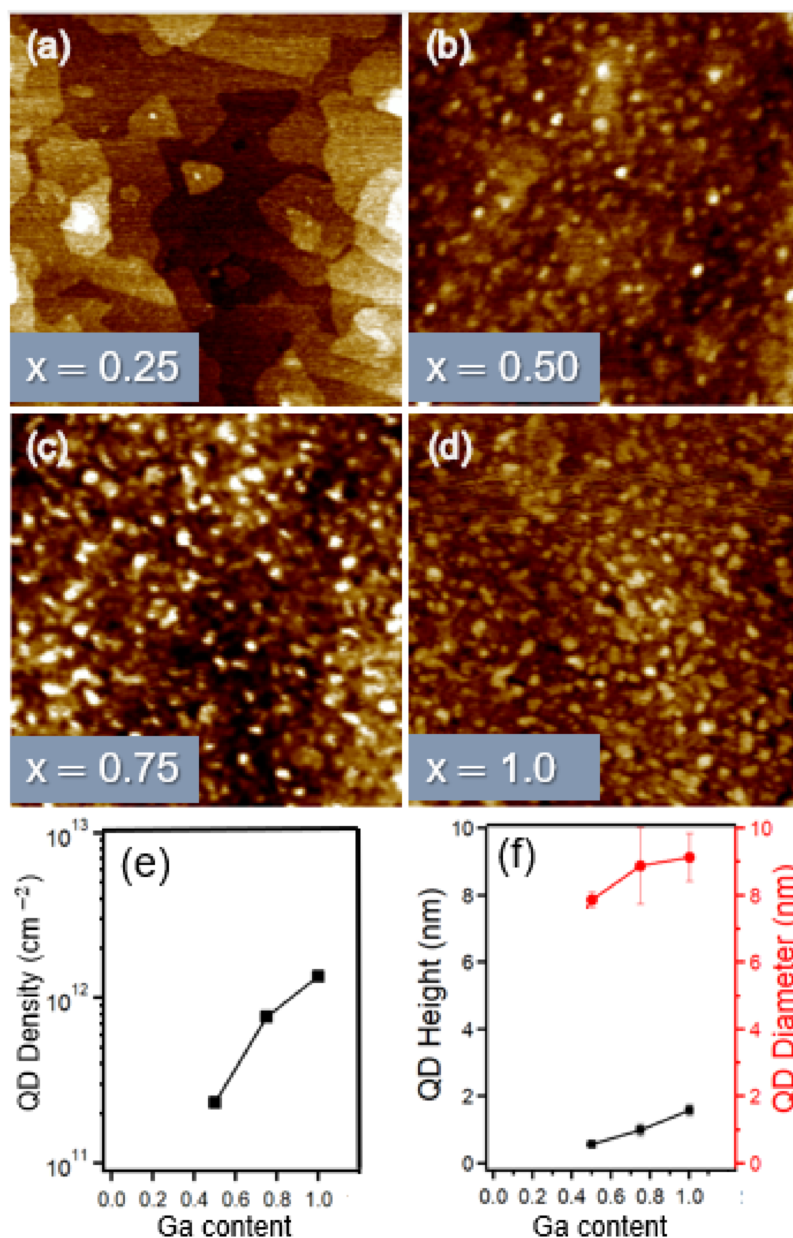

Figure 5.3: (a)-(d) 500 nm × 500 nm AFM micrographs showing the effect of Ga content on the morphology of 3 ML $In_{1-x}Ga_xAs/InAs(111)A$. (a) For $x = 0.25$, the InGaAs forms a smooth 2D layer with formation of only occasional QDs. (b) Self-assembled QDs appear for $x \geq 0.50$. As the Ga concentration is increased to (c) $x = 0.75$, and (d) $x = 1.00$, we see QD size and density increase. (e) Areal density of $In_{1-x}Ga_xAs/InAs(111)A$ QDs as a function of x. (f) Average QD height (left axis) and diameter (right axis) against x. All samples grown at $T_{sub} = 410$ °C, from a coverage of 3 ML InGaAs. The z-scale for AFM images (a)-(c) is 2 nm, and 5 nm for (d) for clarity. The z-scale for AFM images is 4 nm

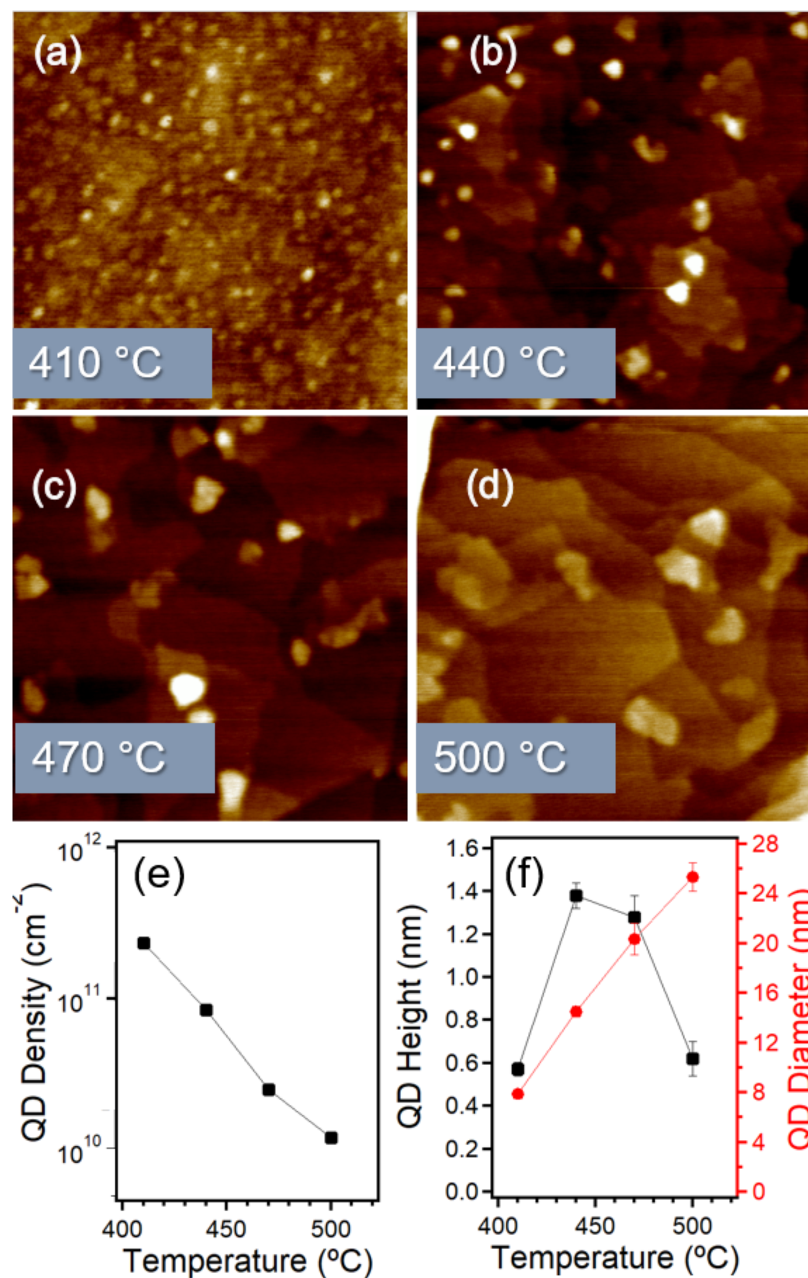

Figure 5.4: 500 nm × 500 nm AFM micrographs showing how the morphology of 3 ML $In_{0.5}Ga_{0.5}As$/InAs(111)A changes as T_{sub} is increased: (a) 410 °C, (b) 440 °C, (c) 470 °C, and (d) 500 °C. QD size increases as we raise T_{sub}, accompanied by a decrease in QD areal density. (e) Areal density of 3 ML $In_{0.5}Ga_{0.5}As$/InAs(111)A QDs versus T_{sub}. (f) Graph of average QD height (left axis) and diameter (right axis) versus T_{sub}.

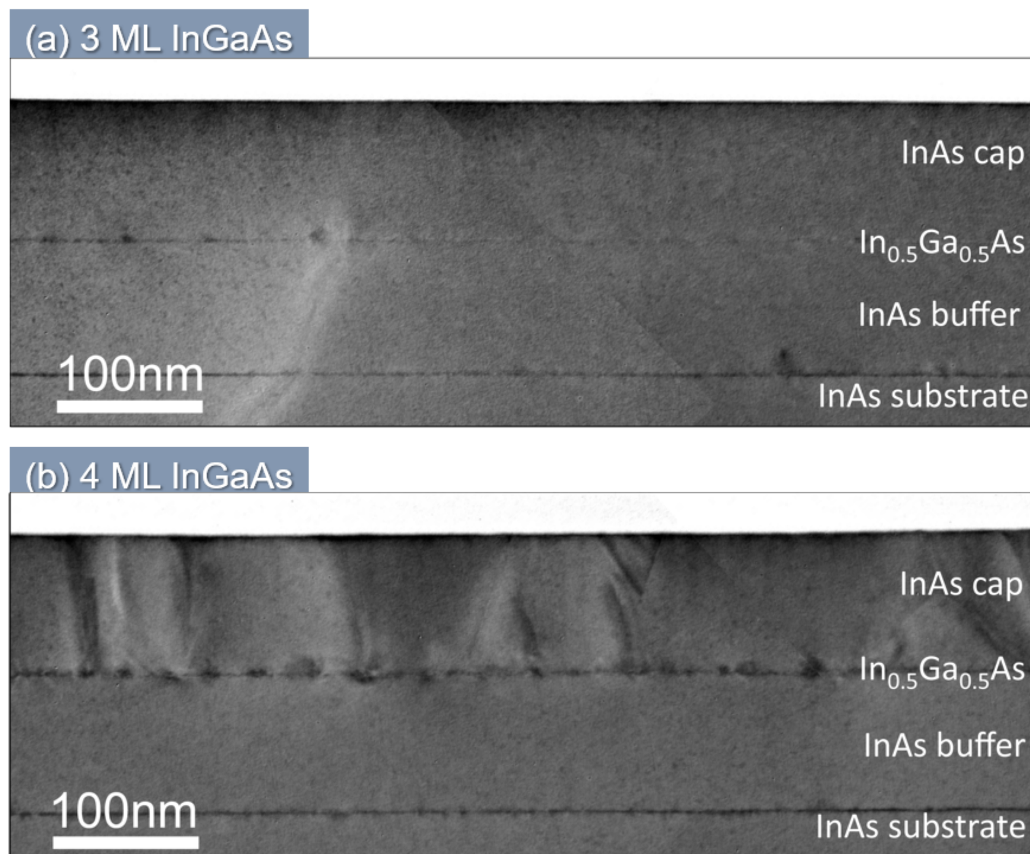

Figure 5.5: Cross-sectional TEM image montages taken at low magnification of $In_{0.5}Ga_{0.5}As$/InAs(111)A samples containing (a) 3 ML and (b) 4 ML InGaAs layers. In (a) we can resolve two distinct strained regions: at the interface between the substrate and the homoepitaxial InAs(111)A, and in the 3 ML InGaAs QD layer. In (b) we see the same features, but the contrast for the $In_{0.5}Ga_{0.5}As$ layer is enhanced due to the larger 4 ML QDs in this sample. In addition, dislocations in the InAs cap indicate tensile strain relaxation in these larger 4 ML InGaAs QDs.

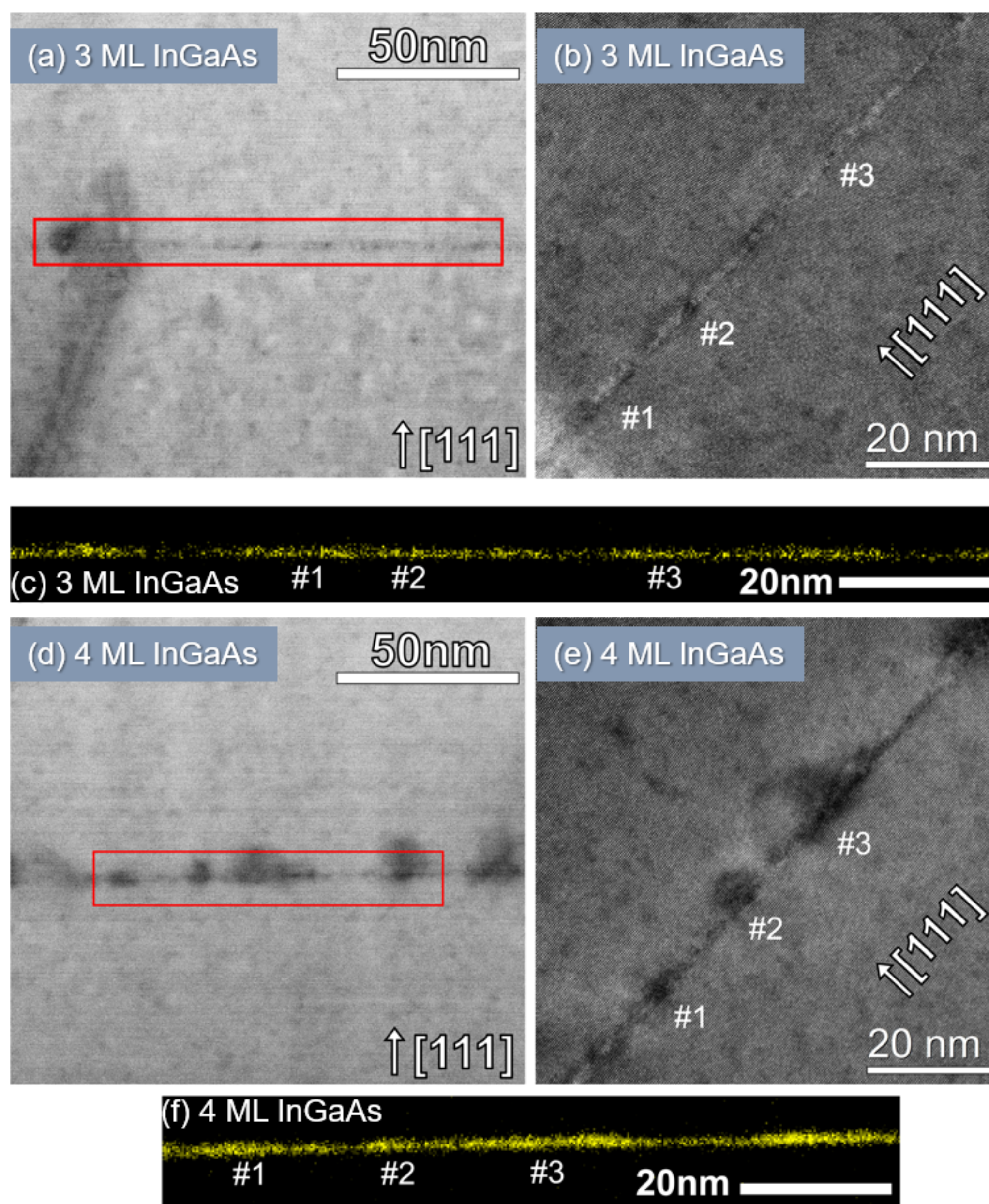

Figure 5.6: Cross-sectional TEM characterization of capped QD samples grown at 410 °C and containing (a)–(c) 3 ML or (d)–(f) 4 ML $In_{0.5}Ga_{0.5}As$. BF STEM images of the (a) 3 ML and (d) 4 ML InGaAs QD layers, and corresponding Ga L-edge EELS maps taken from the boxed areas for 3 ML (c) and 4 ML (f). High-resolution TEM images of (b) 3 ML and (e) 4 ML InGaAs QDs from the same area as the EELS maps in (a) and (c), respectively. For ease of comparison, we have numbered corresponding QD locations in the EELS maps and high-resolution TEM images.

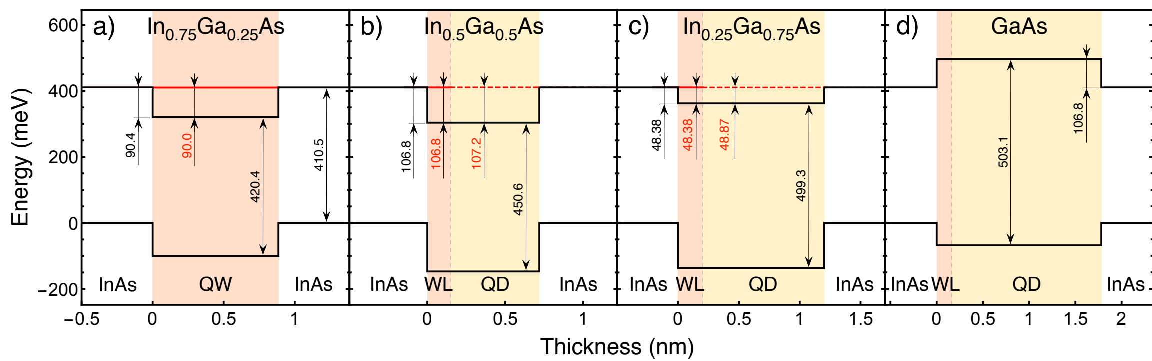

Figure 5.7: Simulation of the bulk band gap of $In_{1-x}Ga_xAs$ (black curves) under biaxial tensile strain on InAs(111)A substrates. The darker orange color signifies the experimentally derived thickness of the 2D wetting layer, showing its reduction with increasing strain. For samples with $x \geq 0.5$, the lighter yellow color represents the average QD height measured with AFM. The red lines show the electron ground states for the wetting layer (solid line) and QDs (dashed line), calculated by solving the Schrödinger equation in the effective mass approximation.

CHAPTER 6:
TENSILE-STRAINED INDIUM GALLIUM ARSENIDE QUANTUM DOTS ON GALLIUM ANTIMONIDE (111)A

Kevin D. Vallejo, Trent. A. Garrett, Madison D. Drake, Baolai Liang, Kevin Grossklaus, Carlos I. Cabrera, and Paul J. Simmonds

Reproduced with permission from MDPI Nanomaterials, *Nanomaterials 2021, 10(10), XXXX*

6.1 Introduction

The opportunities provided by III-V semiconductors grown on high-index planes has increased in recent years. Recent results on self-assembled structures with photonics applications on the (111) surface greatly drive this interest [45]. In addition to developing optimal conditions for homoepitaxy of these materials and self-assembly of these materials [80, 90], integration with 2D materials is a growing field of study. Some of the directions research is taking in regards to this integration include IV-VI rocksalt semiconductors such as PbSe [91],V_2–VI_3 topological insulators [46, 47], and transition metal dichalcogenides [48, 49]. The (111)-oriented quantum dots (QDs) that have been reported to be optically active [11] have negligible fine-structure split-

ting, making them ideal entangled photon sources [44, 45]. Integrating thin films of these materials and nanostructures into transistors with a (111) orientation have the advantage of ballistic electron transport in both Γ and L valleys allowing them to overcome the density of states bottleneck [43].

We employ a combination of surface orientation along the (111) direction and tensile strain between substrate and epilayer to provide an energy landscape where QDs can nucleate defect-free [56, 57, 3]. In optically active materials, the presence of strain even in already self-assembled QDs produces a split in the valence band degeneracy separating the light from the heavy hole bands [69]. This strain is also responsible for the reduction of the semiconductor band gap energy (E_g), which produces a red-shift in the luminal properties of these QDs [71, 45, 72, 11, 92].

Light emission in the infrared (IR) coming from these QDs is ideal for future applications of light-emitting devices (LEDs) based on them. Engineering the band gap of materials that already emit in the IR, we can further reduce their emission spectra. These laser structures are potentially faster, cheaper, and less complicated to grow than quantum cascade laser (QCL) based structures [93, 73].

In the present study we explore the self-assembly of tensile-strained $In_{1-x}Ga_xAs$ QDs by molecular beam epitaxy (MBE) on GaSb(111)A. These materials offer several advantages in combination, as increasing the Ga content in the $In_{1-x}Ga_xAs$ alloy increases the band gap of the QDs while also increasing the tensile strain experienced by the epilayer. The combination of these two factors offers a phase space to study all the possible combination for tuning the light emission and properties of the QDs. Furthermore, the barrier height of GaSb can be increased by adding Al, without significantly increasing the strain values [94].

Previous studies have shown that $In_{0.5}Ga_{0.5}As$ embedded in GaSb(001) as quantum wells are capable of light emission due to the type II or III band alignment where holes are confined in GaSb and electrons in $In_{0.5}Ga_{0.5}As$ [95]. These QWs were shown to emit light in the 0.45 to 0.7 eV range as a function of amount of $In_{1-x}Ga_xAs$ deposited. Gassenq *et al.*demonstrated light emission from a series of thin $In_{1-x}Ga_xAs$ QWs grown on GaSb(001) in the 0.551 to 0.597 eV range [75]. Lower In concentrations have also been shown to form tensile-strained QW and QDs able to emit light in the 0.57 to 0.72 eV range by Terent'ev *et al.* [96], Ledentsov *et al.*, [97] and Toropov *et al.* [74].

Taking advantage of (111) substrates gives us more flexibility in QD tunability, as we get fewer dislocations and a larger space of band gaps between the materials [56, 57]. Building on the work done for this system on InAs(111) substrates [90] we investigate the relation of size and areal density of the self-assembled $In_{1-x}Ga_xAs$ QDs with MBE growth conditions. The properties of these TSQDs will set the stage for device engineering with light emission in the mid-IR.

Reference	Substrate	Epitaxial Structure	Wavelength
Taliercio [95]	GaSb(001)	$In_{0.5}Ga_{0.5}As$ QW	1.7 to 2.7 μm
Gassenq [75]	GaSb(001)	$In_{0.5}Ga_{0.5}As$ SL	2.075 to 2.25 μm
Terent'ev [96]	GaSb(001)	GaAs QW and QD	1.72 to 2.175 μm
Toropov [74]	GaSb(001)	GaAs QD on GaAsSb	1.72 to 2.175 μm

Table 6.1: Light emission studies of InGaAs on GaSb

Demonstrating light emission from $In_{0.5}Ga_{0.5}As$ TSQDs on a GaSb barrier would confirm the effects of tensile strain on band gap reduction by pushing the states towards confinement. In contrast, were we to find that there is not enough confinement for the tensile-strained islands to behave like quantum dots, increasing the barrier

height using $Al_xGa_{1-x}Sb$ provides large room for band gap increase without changing the strain levels significantly.

GaSb requires a lower beam equivalent pressure to grow than GaAs (3×10^{-6} Torr vs. 1×10^{-5} Torr). In addition, the (111) surface has a lower group V sticking coefficient thatn the (001) surface. Because of these considerations we paid special attention to the time at which different group V elements where present in the chamber.

6.2 Methods

We grew all samples using solid-source MBE on Wafer Tech. unintentionally doped, p-type nominally on-axis (±0.1 °), 0.5 mm thick GaSb(111)A substrates. We use high-purity indium metal to mount our GaSb(111)A substrates onto molybdenum blocks in order to accomodate the unsual cleaving geometry of the substrate and ensure temperature uniformity. We monitored the substrate temperature (T_{sub}) using a BandiT temperature monitoring tool and a thermocouple located behind the substrate, calibrated by reflection high-energy electron diffraction (RHEED) against known reconstructions of the GaSb surface. We calculate growth rates in monolayers per second (ML/s) on (111)A from RHEED intensity oscillations (RIOs) performed on the GaAs (001) surface and calculating the difference in atomic deposition amount based on the difference in lattice constant. We calibrate the composition of the $In_{1-x}Ga_xAs$ layers using RIOs and calculating the corresponding beam equivalent pressures (BEP).

Following the scarce literature resources available for this orientation we attempted the GaSb hompepitaxial growth with a T_{SUB} = 450 °C, a growth rate of 570 nm/hr (0.45 ML/s), and a V/III BEP flux ratio of 1.7 during growth [61]. We determined

that while growth rate and substrate temperature were well tuned in this work, a much higher V/III BEP ratio offers a better quality surface prior to QD deposition (V/III$\geqslant$ 15). We studied the morphology of the surface using AFM (Fig. 6.1). The As-for-Sb exchange is the most important group V interaction within InAs- and GaSb-based material systems. For mixed group alloys, group III elements determine the growth rate. Ga-As bonds are stronger than Ga-Sb bonds and there is a thermodynamic driving force to replace the Sb atoms with As atoms. For this system, we calculated the tensile strained levels at different concentrations (caused by the larger lattice constant of GaSb compared to InGaAs) of Ga in the $In_{1-x}Ga_xAs$ alloy to both ensure care when growing thick films and for us to use in our calculations of band gap size, being careful we do not exceed the Matthews-Blakeslee limit. The tensile-strained values for 25%, 50%, and 75% Ga concentration are 2.27%, 3.93%, and 5.6% respectively. We included computational modelling to calculate the confined energy levels for electrons and holes in the TSQDs using the Schrödinger equation for the envelope function in the effective mass approximation. The axial component of strain modifies the valence bands while the hydrostatic strain acts on the band gaps of the system. The model we used for these calculations is a more sophisticated version of that explained in Ref. [68].

6.3 Results and Discussion

6.3.1 GaSb Homoepitaxy

Prior to the deposition of $In_{1-x}Ga_xAs$, we needed a smooth GaSb buffer layer free of hillocks or other detrimental features for QD nucleation. Following the approach of Dura *et al.*[61] we optimized the procedure and determined the ideal conditions for

a highly uniform surface with step flow terraces of about 100 nm are T_{sub}= 450°C, growth rate of 0.45 ML/s, and a V/III BEP ratio of 16 (Fig. 6.1). The films we optimized are free of hillocks and other imperfections reported in previous studies. We reduced the growth rate to 0.225 ML/s and increased significantly the V/III ratio (as seen in the progression of figure 6.1 (a)-(d)) to ensure a smooth surface with values of root-mean-square roughness (Rq) as low as 3 Å. The Rq value decreased as we increased the V/III by increasing the BEP flux of Sb, and kept the Ga (growth limiting element) constant (Fig. 6.1(e)). These Rq values will be the lowest reported so far in the literature.

Features on the surface are largely gone when the Sb BEP pressure is 3.1×10^{-6} Torr . The inset on Fig. 6.1(d) shows an interesting coalescence of atoms along the line of symmetry of each triangular terrace. We believe this structural feature corresponds to high energy barriers near the edges of terraces. Ga antisites (Ga_{Sb}) form when the Sb lattice site is occupied by a Ga atom, resulting in the p-type conducting nature of GaSb [98]. The high quality of this GaSb film was confirmed by the optical activity measure using photoluminesce (PL) and discussed below.

6.3.2 $In_{1-x}Ga_xAs$ Quantum Dots

We used as a starting point the conditions for $In_{1-x}Ga_xAs$ nucleation we achieved on InAs(111)A substrates that we optimized in chapter 4. We studied several variables in order to optimize the structural integrity of the QDs, which we then analyzed using different characterization techniques. The variables we studied include deposition amount, substrate temperature, alloy composition, and interval between group V overpressure.

The structure is made of a 250 nm GaSb buffer layer we grew at the optimized

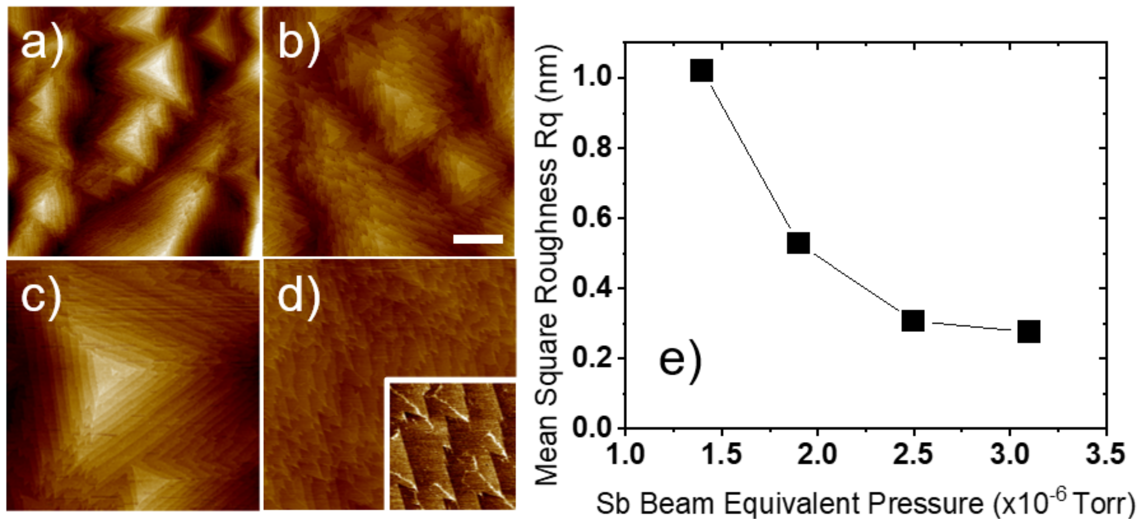

Figure 6.1: 5 μm x 5μm AFM micrographs showing the evolution of the surface quality of GaSb with varying quantities of Sb overpressure. The images have a vertical scale of 6 nm. We grew (a) at 1.5x10^{-6} Torr BEP and several large "wedding cake" structures are visible, the structures are significantly flattened in (b) which we grew at 1.9x10^{-9} Torr. (c) shows a large structure with step-flow growth product of its 2.5$\times 10^{-6}$ Torr BEP Sb overpressure, and finally (d) shows large terraces of 500 nm, which we grew at 3.1x10^{-6} Torr. Inset is a 1 μm x 1 μm section with a vertical scale of 1 nm. (e) shows the relationship between Rq and Sb overpressure where we obtained a significant improvement of the surface by increasing the V/III ratio.

conditions stated in section 6.3.1. On this smooth surface we deposit 0.5 to 3.0 ML of $In_{1-x}Ga_xAs$ at different compositions, growth rates, and substrate temperatures. In order to protect these QDs from the atmosphere and allow us to carry out PL measurements, we covered them with a 75 nm layer of GaSb grown at the same conditions as the buffer, and finally deposited an identical layer of $In_{1-x}Ga_xAs$ on the surface for study using AFM. The final structure is shown in Fig. 6.2. During QD growth we explored ranges in temperature from 610° to 670° °C as measured by our thermocouple (presumably 380° to 450°C), for growth rate 0.1 to 0.4 ML/s, and

0.5-3.0 ML InGaAs QD
640-670 °C | 0.1-0.4 ML/s

75 nm GaSb buffer
670 °C | 0.45 ML/s

0.5-3.0 ML InGaAs QD
640-670 °C | 0.1-0.4 ML/s

250 nm GaSb buffer
670 °C | 0.45 ML/s

GaSb(111)A substrate

Figure 6.2: Sample growth structure. Buried QD layer is used for PL studies, while the top layer is used for AFM characterization.

V/III BEP ratios of approximately 12.

RHEED Pattern Evolution

We studied the evolution of the RHEED diffraction pattern during each step of sample growth in order to map sample quality to visible RHEED features. Figure 6.3 details patterns for each step in the sequence. Steps (a)-(d) of figure 6.3 show the evolution of the homoepitaxial GaSb. We determined a transition in the surface reconstruction at 650 °C from seemingly (2x4) to a (12x1), in accordance with Proessdorf *et al.*. [99].

Deposition of $In_{1-x}Ga_xAs$ caused an evident shift in the RHEED pattern potentially due to the quick onset of self-assembled structures. A spotty pattern substitutes the streaky reconstruction and it is only further enhanced as the sample is brought

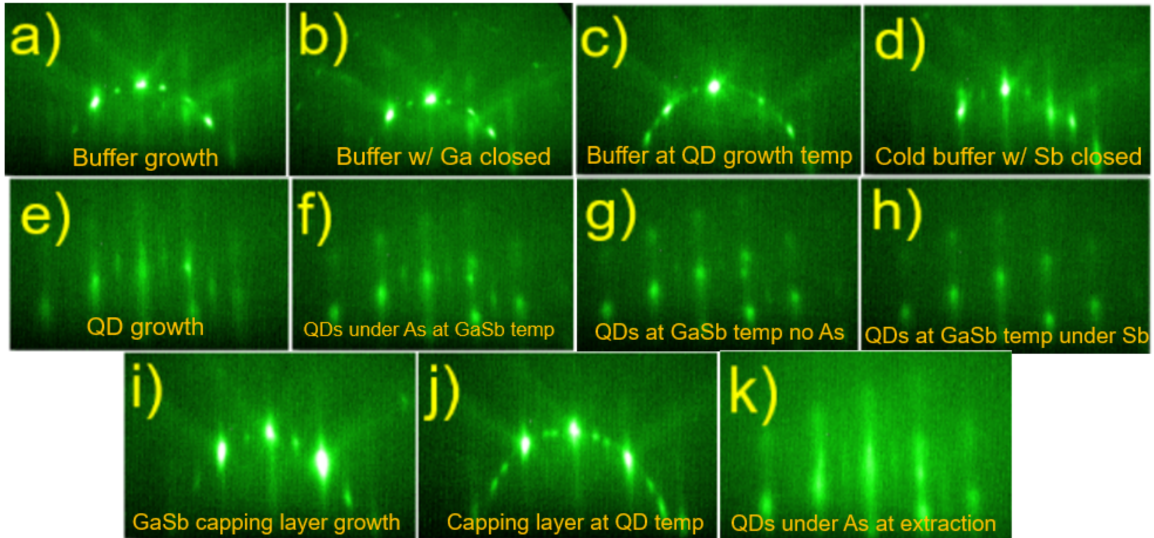

Figure 6.3: RHEED patterns obtained during the various stages of growth of buffer, QD layer, capping layer, and top QD layer.

back to the GaSb growth temperature under an As overpressure (Fig. 6.3(e)-(h)). It is not until the As is purged from the chamber, Sb is reintroduced, and we grow several monolayers of GaSb that the streaky pattern returns, indicating a high-quality interface despite the 5% lattice mismatch between GaSb and $In_{1-x}Ga_xAs$(Fig. 6.3(i)-(j)).

Group V Presence Effects

During the critical pause between the first layer of $In_{1-x}Ga_xAs$ QDs and the GaSb capping layer (Fig. 6.2 bottom) the As to Sb transition is a critical step in determining the quality of the resulting sample.

We measured the time and amount of GaSb required for the transition between spotty pattern formed during QD deposition (Fig. 6.3h) to a streaky pattern (Fig. 6.3i) to happen (Fig. 6.4(b)). This time varies from 7 to 120 seconds, depending

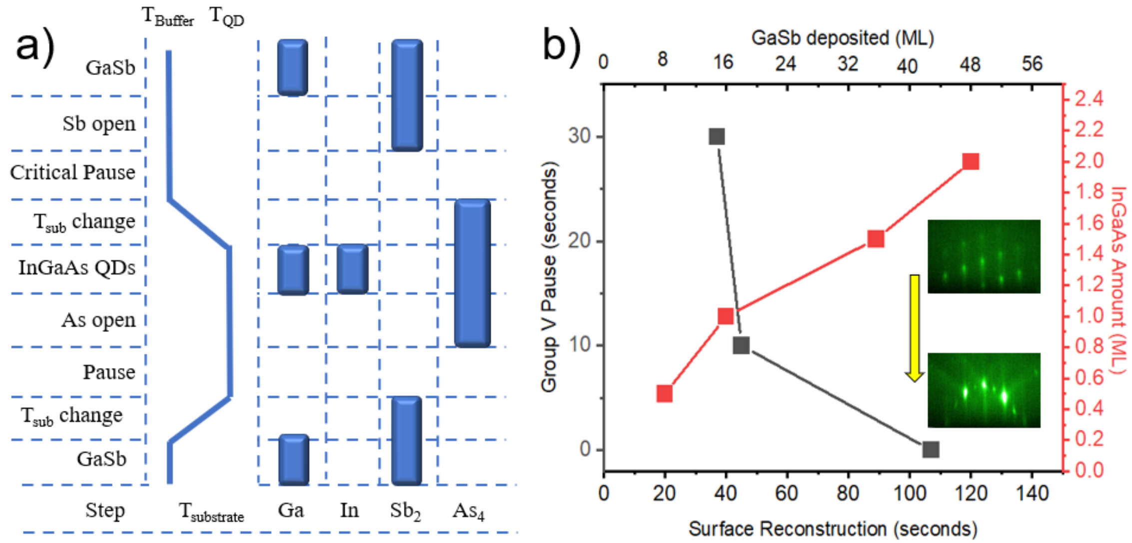

Figure 6.4: (a) Shutter sequence during growth of samples. (b) Relation between GaSb capping layer surface reconstruction time as a function of InGaAs deposition amount, and As-to-Sb time pause during growth.

on the time between closing the As overpressure and allowing Sb to flow in, and the amount of InGaAs deposited on the surface. The sequence of shutter opening and closings is illustrated on Fig. 6.4(a).

Figure 6.2 shows the trends for these changes as functions of thickness of $In_{1-x}Ga_xAs$ and the pause between group V elements. The time it takes for the surface to reach "smoothness" (defined as a streaky RHEED pattern) increases almost linearly with the thickness of deposited $In_{1-x}Ga_xAs$. In contrast, the longer the pause between group V elements the sooner the surface reaches this state. It should be noted that a pause of 0 seconds is in actuality detrimental to the overall morphology of the QD samples: the presence of too much As when the GaSb capping layer begins to grow produced large pits on the surface of the samples, almost identical to those that occur in pauses of 30 seconds.

Low Temperature TSQD Growth

Having identified all the conditions for successful nucleation of TSQDs, we grew a series of samples with $In_{1-x}Ga_xAs$ QDs grown at 420 °C (670 °C on our thermocouple) at 0.1 ML/s. We skipped the pause between As and Sb – essentially setting a pause of 0 seconds- to observe the effect in the sample characteristics. We characterized this samples using AFM and PL looking for a relation between QD morphology and light emission (Fig. 6.5)

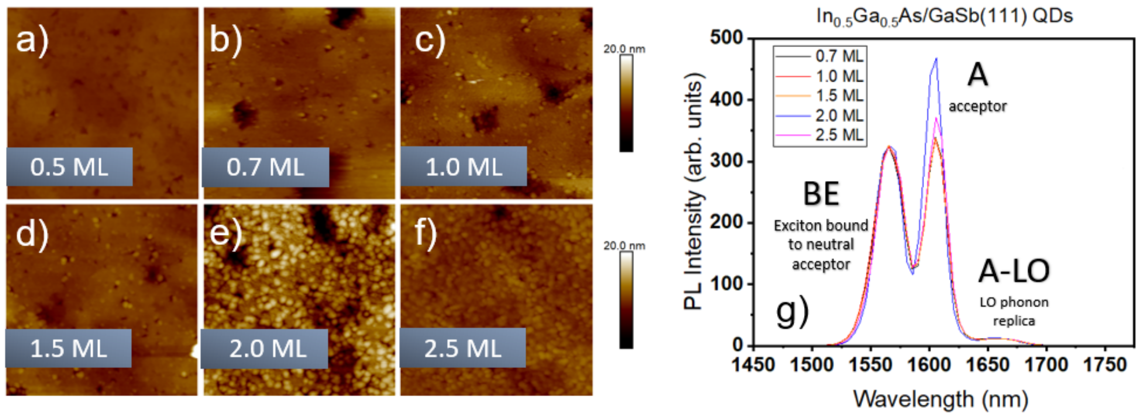

Figure 6.5: (a)-(f) 1 μm x 1 μm AFM scans of $In_{1-x}Ga_xAs$QDs grown at 420 °C (640 °C on our thermocouple) at 0.1 ML/s. The pause between group V switch was 0 seconds (no pause). (g) Photoluminescence spectra obtained from samples with 0.7 to 2.5 ML using an InGaAs detector. The three emission peaks are identified with their corresponding transitions in the GaSb buffer layer.

We can appreciate an absence of islands at a deposition of 0.5 ML, instead only a series of pits we believe to be the result of Sb/As atomic substitution (Fig. 6.5(a). At higher deposition amounts the number and size of islands increases, while the big valleys in the samples remain relatively unchanged (Fig. 6.5(b)-(f)).

Figure 6.5(g) shows the PL spectra of the first series of QD samples. All the peaks

present in this graph correspond to different transitions in the GaSb substrate (Table A.1).

Table 6.2 lists the three different PL peaks and their corresponding transitions. We identified these emission labels following the study from Lee *et al.*(Ref. [100]). The absence of light from the TSQDs can be an indication of these structures being highly relaxed and full of defects – which would limit prevent light emission due to a high occurrence of scattering events- or they simply emit light at a longer wavelength than our current InGaAs detector is able to measure. We currently have samples from the high temperature series being analyzed by one of our collaborators to verify the quality of the InGaAs layer. At the same time our collaborator at UCLA is trying to detect light emission from these samples using a Fourier-transform IR PL setup. We hope to receive results in the weeks leading up to the oral defense date. A third possibility can be the band alignment of this system, which I will discuss below in section 6.3.2.

Table 6.2: GaSb PL Peaks

Peak	Center Wavelength	Transition [100]
1	792 meV	Bound Exciton
2	774 meV	Acceptor
3	753 meV	LO phonon acceptor replica

High Temperature TSQD Growth

After analyzing the data, we determined the optimal time for the critical pause between As/Sb switch. Once the InGaAs layer of TSQDs finishes, we heat the substrate back to the GaSb growth temperature (or stay at the same temperature if the TSQDs were grown there) under As overpressure. We then close the As shutter and wait 10

seconds. After this we open the Sb shutter and after quickly checking the Ga temperature stability for 5 seconds, we begin to grow the GaSb capping layer.

In addition to the critical pause, we also decided to halve the GaSb growth rate to 0.225 ML/s, and increase the InGaAs growth rate to 0.4 ML/s. This effectively doubles the Sb overpressure during the buffer and capping layer growth, and limits the time for InGaAs to interact with the GaSb layers, which are the potential cause for the pits and valleys observed in previous series.

Figure 6.6(a)-(c) shows the AFM scans of TSQDs grown with these optimized conditions.

Transmission Electron Microscopy

We used TEM to inspect the structural integrity of our InGaAs/GaSb QDs grown at high temperature. Fig. 6.7 shows increasing magnifications of the buried $In_{0.5}Ga_{0.5}As$ QD layer. Figure 6.7(a-b) show the high level of epitaxial integration between the layers, evidenced by the lack of defects present. Figures 6.7(c-e) show micrographs increasingly focused on individual QDs which show how highly confined the strain is in the $In_{0.5}Ga_{0.5}As$ layer.

Electronic Structure

Our model for this system predicts a the InGaAs/GaSb band alignment to be type III (Fig. 6.8). This is in agreement with previous reports from Taliercio *et al.*[95].

If these TSQDs really have a type-III band alignment, we may not have an effective band gap across which we obtain recombination and photon emission. Even in this type of band alignment, there can be confined states in the InGaAs region which could

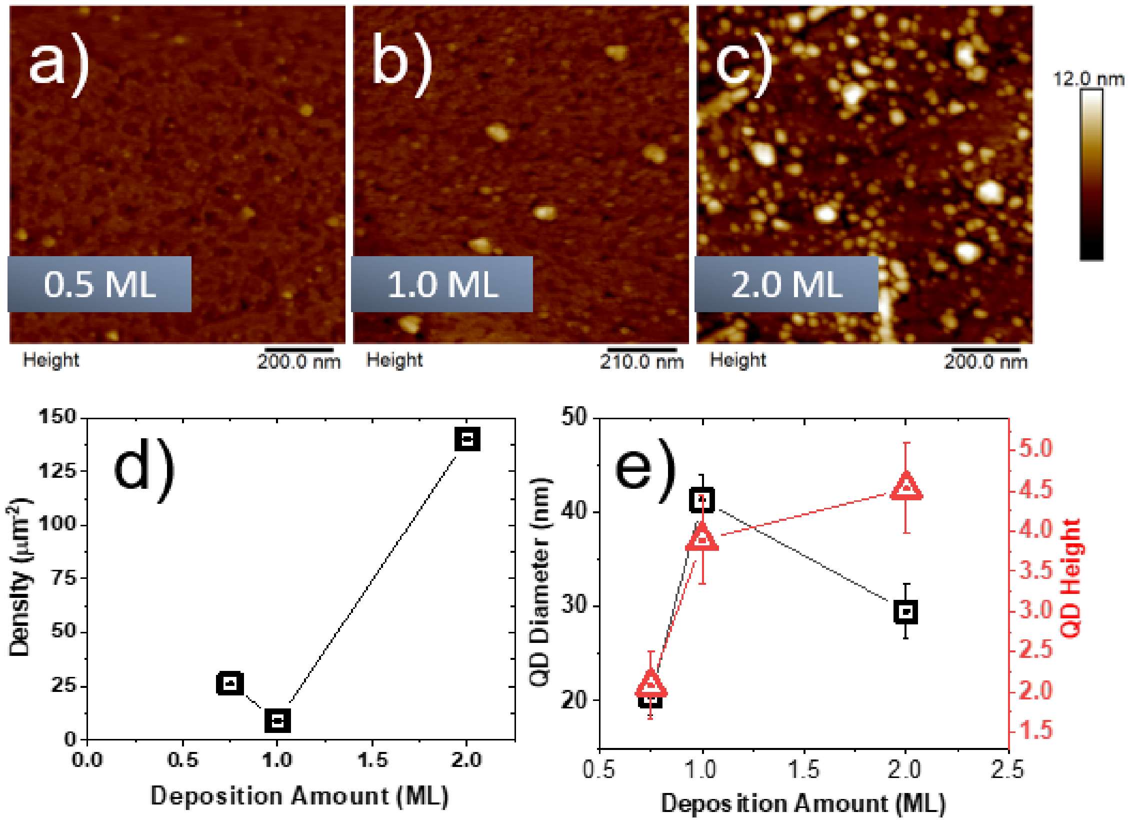

Figure 6.6: (a)-(c) 1 μm x 1 μm AFM scans of $In_{1-x}Ga_xAs$QDs grown at 450 °C (670 °C on our thermocouple) at 0.4 ML/s. The pause between group V switch was 10 seconds. (d) Shows the density of these TSQDs as a function of deposition amount. (e) Plot of diameter and height of TSQDs as a function of deposition amount.

potentially generate a virtual type-II band alignment and generate photon emission. Further calculations and PL studies will help us elucidate the nature of the electronic structure.

6.4 Conclusions

In this chapter we developed a reproducible set of conditions for high quality GaSb(111)A homoepitaxy. The quality of these samples is currently the best to date. In addi-

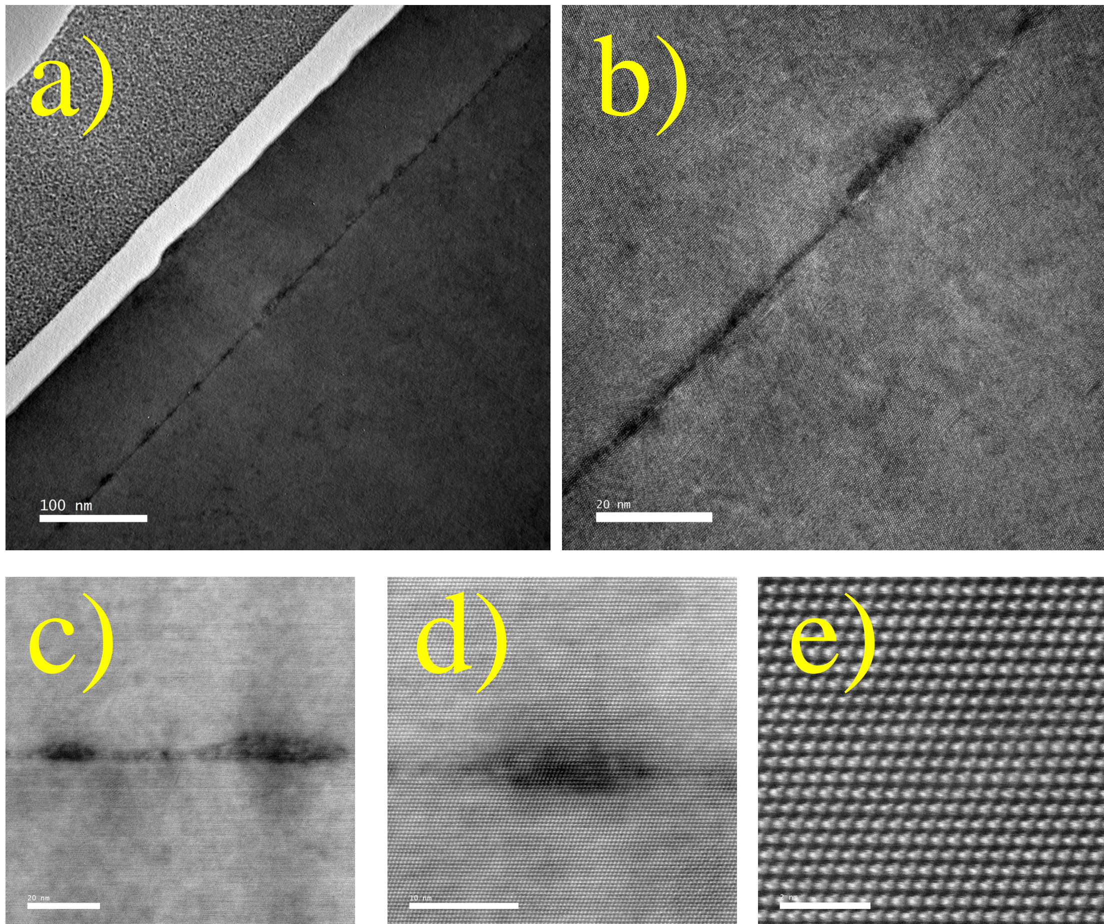

Figure 6.7: Transmission electron microscopy images of an $In_{0.5}Ga_{0.5}As$ QD layer, 3 ML in thickness buried under 75 nm of GaSb. (a) shows the strain to be focused to the $In_{0.5}Ga_{0.5}As$ layer with no directly visible defects forming. (b) Shows a series of individual QDs evidenced by the strain contrast. (c) Closer images of two differently sized QDs. (d) Single QD seen with atomic resolution, and (e) shows the atomic arrangement in the QD.

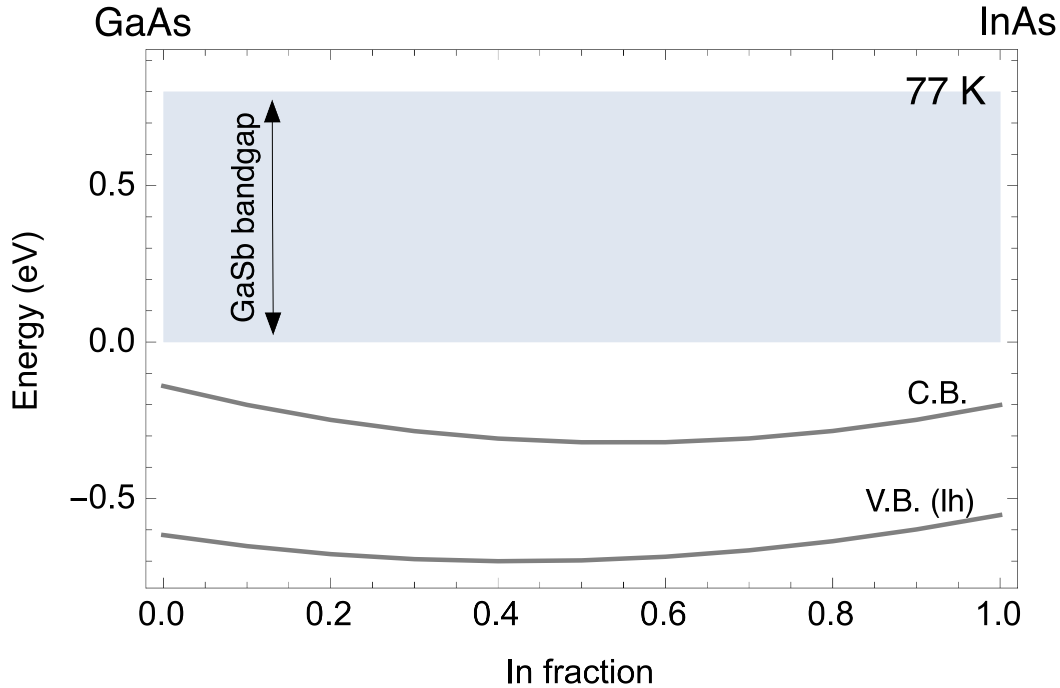

Figure 6.8: Schematic of band alignment in the InGaAs/GaSb TSQD system with biaxial strain. It is notable that at all concentrations this system exhibits a type III band alignment.

tion, we confirmed the self-assembly of $In_{0.5}Ga_{0.5}As$ TSQDs on GaSb(111)A, and the excellent optical quality of the GaSb buffer layer on which we grew them. We currently have TEM, FTIR-PL, and computer-aided modelling studies undergoing to shine light on the photonic nature of these structures.

Author Contributions

Kevin D. Vallejo was the lead grower for this study: designing, programming and growing the samples. In addition he contributed the literature review, sample preparation and shipping, XRD, as well as data gathering, analysis, and manuscript preparation.

CHAPTER 7:
COLLABORATIONS AND FUTURE WORK

Kevin D. Vallejo

A fundamental advantage of focusing on the growth and optimization of structures using MBE is the ease with which collaborations can be established. The material selection and sample quality of our laboratory has been recognized by national and international teams who reached out to us to fabricate samples for their projects. In the first part of this chapter I summarize some of the work I performed for these projects and the main results obtained so far at the time of writing. In the second part, I summarize what the next steps for some of the projects in this dissertation could be. Very interesting fundamental science and applications will no doubt derive from the results summarized so far.

7.1 Collaboration Efforts

7.1.1 Tensile-Strained Quantum Dots on InAlAs

The pioneering efforts on the self-assembly of TSQDs offered me the insights on how to establish the optimal growth methodology for this tensile-strained systems. The project focused on GaAs/InAlAs TSQDs aimed to write a recipe book for the self-assembly of these nanostructures, and produce a photonic structure able to produce

highly entangled photons with very small fine-structure splitting. The project focused on Ge/InAlAs had the objective of turning Ge from an indirect band gap semiconductor to a direct band gap one. The change in the band configuration due to strain offers the possibility to create photonic devices based on Ge. I helped develop the recipes for the growth of several samples used in these projects, in addition to do XRD characterization checking for alloy composition and strain values. We produced several publications from these projects: an initial work on GaAs/InAlAs [11], Ge/InAlAs [3], and anomalous wetting layer growth on GaAs/InAlAs [92].

7.1.2 Review of Self-Assembled Quantum Dots via MBE

As part of the team that leads the global effort on self assembly of tensile strained semiconductor QDs, I was part of crafting a tutorial on how to utilize MBE to grow self-assembled QDs. We summarized the entire history of the field since the 1990s until now, and showed how our TSQDs on (111) have the potential to duplicate the amount of nanostructures available for self-assembly. This is due mainly to vast majority of systems being compressive-strain materials grown on (001) surfaces. It is considerably more difficult to identify the growth conditions for the (111) surface, hence the allure of doing research on lower index surfaces. In addition to my own original research, I contributed the review of the most significant advances in the field of self-assembled II-VI and III-nitride QDs [101].

7.1.3 Superconduction of Al on InAs(111) Quantum Well

This project aims to take advantage of the high quality InAs developed in Chapter 4 and use it as substrate on which to deposit thin layers of epitaxial Al. There are few studies on the behavior of electron gases on surfaces other than (001) [102, 103]. Our work focuses on having a superconductor (Al) in proximity to a high spin orbit

material. Research in quantum computing has identified Majorana zero modes as a potential vehicle for qubits [104]. The interface between superconductors and one-dimensional semiconductors are a promising are where these MZM can be found [105]. My contribution to this project so far includes the growth of high quality InAs substrates covered in amorphous As, plus safe shipping for subsequent deposition of Al. Current study shows the Al layer forms interesting patterns on the InAs substrate as shown in Fig. 7.1.

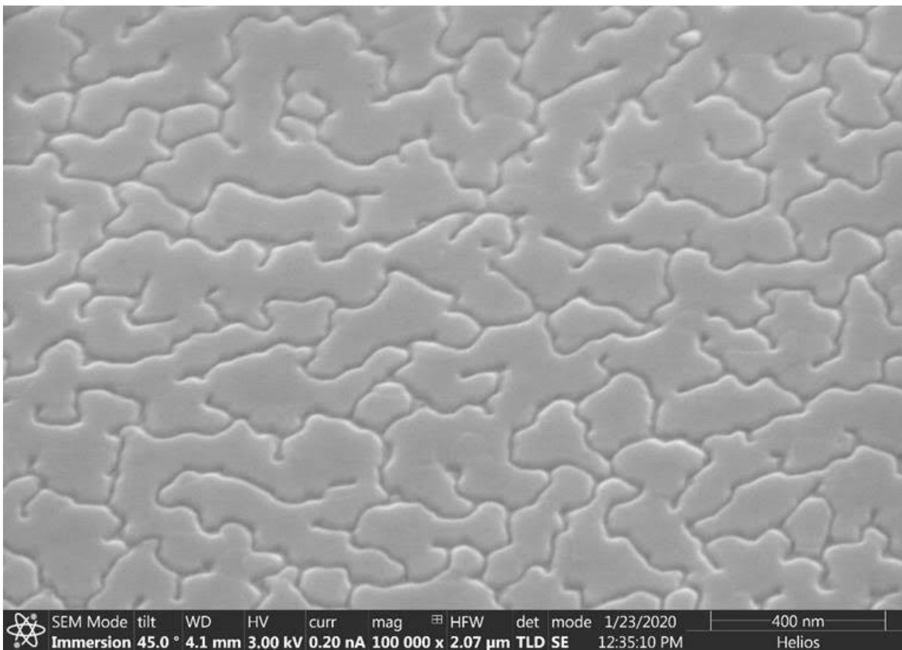

Figure 7.1: SEM of the surface of an Al epilayer deposited on InAs(111) grown homoepitaxially on InAs(111)A.

Our collaboration in this project includes a team of researchers at New York University, who are among the lead experts in this area.

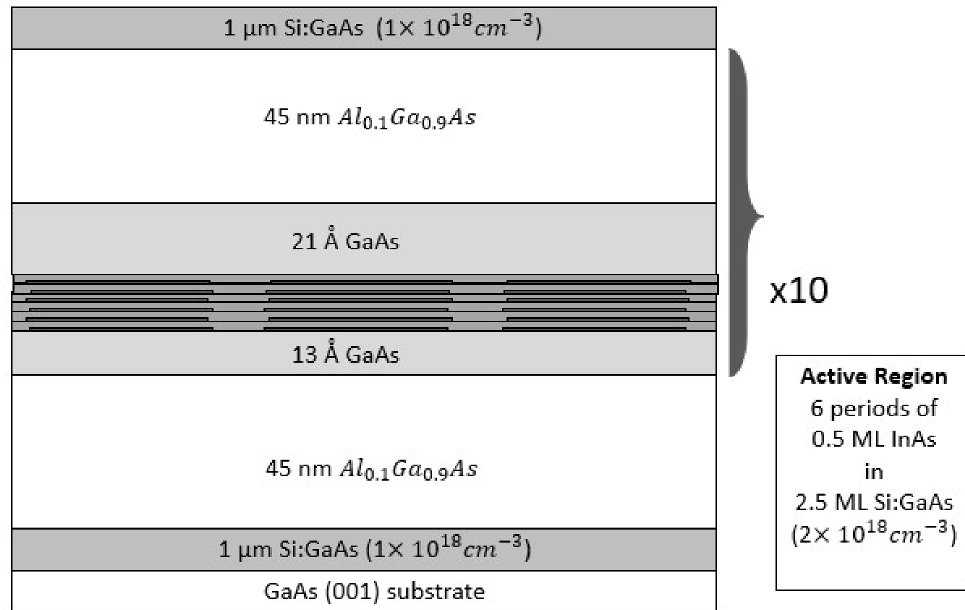

Figure 7.2: Schematic of sub-monolayer quantum dot superlattice structure for infrared photodetectors. The active region is marked as the substructure that repeats six times.

7.1.4 Influence of the arsenic flux on the performance of infrared photodetectors based on InAs submonolayer quantum dots

In collaboration with a group from the University of Sao Paulo we grew a series of samples of sub-monolayer quantum dot photodetectors (SMLQDIPs). The structure for these samples involved the programming of nested loops in the growth software to accomplish superlattices of sub-monolayer quantum dots (SMLQDs) within larger superlattices that act as electronic barriers (see Fig. 7.2).

These structures present in principle a more controllable and uniform structure and composition when compared to traditional SK grown dots. The samples show high optical quality evidenced by their PL response (Fig. 7.3(a)). In addition, pre-

liminary results show a record value of detectivity for this type of devices, which have been submitted for publication in the journal Sensors and Actuators A: Physical.

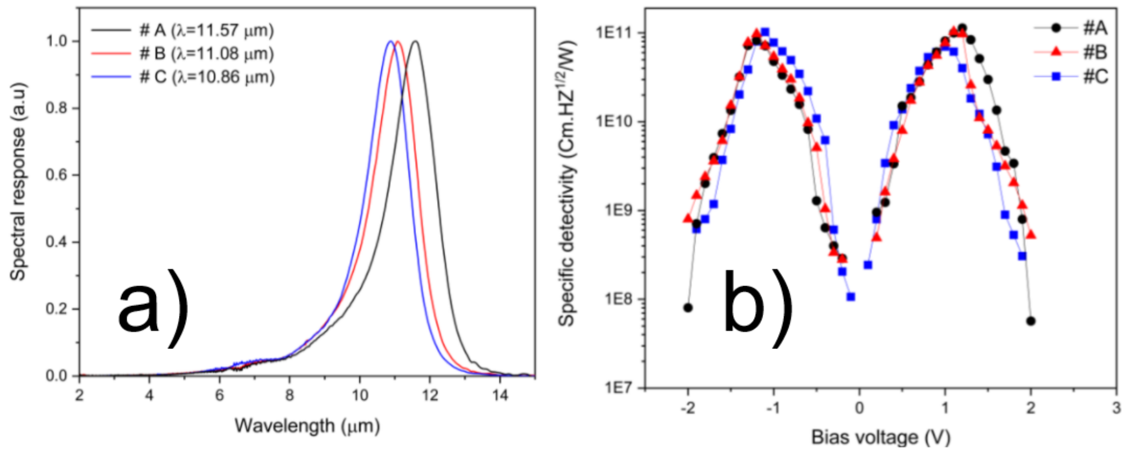

Figure 7.3: (a) Photoluminescence spectra of the different SMLQDIP samples. (b) Plot of the specific detectivity of the samples. The samples are A (2 × 4 with low As), B (c(4 ×4 with low As), and C (c(4 ×4 with high As) grown with different surface reconstructions prior to the SMLQDs deposition.

My contribution to this project was the calibration, growth software programming, growth, XRD characterization, and shipping of about a dozen different samples with variations in the structure shown in Fig. 7.2.

7.1.5 Interfacial structure and luminescence properties of epitaxial PbSe films on (111)A InAs

Integration of rocksalt IV-VI materials on III-V semiconductors offers new research directions in infrared photonics. This project aims to provide a route for the monolithic integration of these materials with nearly lattice matched MBE growth of PbSe on InAs (Fig. 7.4). Integration of IV-VI rocksalt materials has been reported in the (001) directions, however the preferential dislocation direction for this system

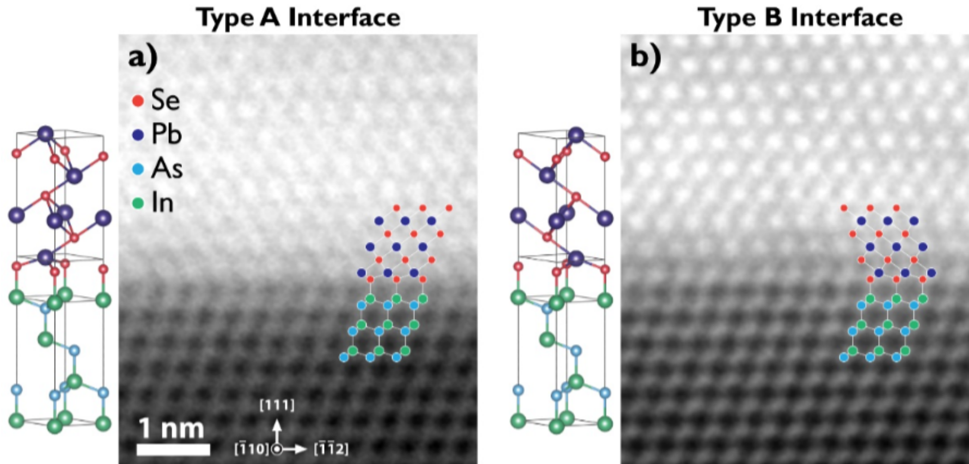

Figure 7.4: PbSe/InAs interfacial structures: High-resolution HAADF-STEM cross sections of two PbSe/InAs interfaces with proposed structures.

prevents the relaxation of thermal stress when grown in this orientation, resulting in cracked samples. For this reason it is optimal to grow on the (111) direction, where strain can be relaxed via glide planes and provide structural integrity even at cryogenic temperatures.[91] My contribution to this study was the growth of homoepitaxial InAs substrates that were capped with amorphous As and shipped to the NYU team, where subsequent PbSe deposition and characterization gave rise to a joint publication (Ref. [67]).

7.2 Future Work

There are many new research directions that can be pursued based on the work I presented in this dissertation. With the optimized surfaces of InAs(111)A and GaSb(111)A on the (111)A surface from chapters 4 and 6, integration of materials like metals and IV-VI semiconductors is possible as discussed in this chapter. On the basis of the highly encouraging initial results discussed here, I anticipate that

other low-dimensional structures can be designed and grown to greatly increase our understanding of transport in materials with this unusual (111)A orientation. As an example, developing an InAs/GaSb quantum well in this crystallographic orientation, or a series of quantum wires in higher index surfaces is not too far in the future. These studies can be used to understand the behavior of the electron accumulation layer that is often formed in InAs(111) [106]. Self-assembled quantum wires with low defect density are highly sought structures for their light emission properties (just like QDs) [107].

More closely in line with this work, exploring different composition for the InGaAs self-assembled structures on GaSb is a natural step to increase our understanding of this system (for which only a 50% stochiometric alloy was characterized). In addition, following the detection of light from these QDs, measuring the fine-structure splitting between orthogonal bright exciton states would help understand the degree of correlation and entanglement among the emitted photons. To date, the only optically active TSQDs system is the GaAs/InAlAs developed by Simmonds [56] and Schuck [11]. Furthermore, light emission is potentially still able to be optimized by exploring changes in the QD morphology, which has been demonstrated to have effects on QD-emitted light [11].

With respect to work developed in chapter 3, the obvious next step should be to complete and optimize the TGS PL setup to provide the SAW spectra for a proof of concept study. The light detection and sample fabrication expertise is already planned to be focused in the same work space. Optimizing the alignment in the relatively complex TSG PL setup shown in Fig. 2.13 will be the first step.

Author Contributions

Each subsection of this chapter contains the contributions of Kevin D. Vallejo for each project. This chapter was entirely designed and drafted by Kevin D. Vallejo.

REFERENCES

[1] Jeffrey Y Tsao. *Materials fundamentals of molecular beam epitaxy*. Academic Press, 2012.

[2] Dragan Manasijević, Duško Minić, Ljubiša Balanović, Milena Premović, and Milan Gorgievski. Experimental investigation and thermodynamic extrapolation of the ga-ge-sb phase diagram. *Journal of Phase Equilibria and Diffusion*, 40(1):34–44, 2019.

[3] Kathryn E Sautter, Kevin D Vallejo, and Paul J Simmonds. Strain-driven quantum dot self-assembly by molecular beam epitaxy. *Journal of Applied Physics*, 128:031101, 2020.

[4] Włodzimierz Nakwaski. Effective masses of electrons and heavy holes in gaas, inas, a1as and their ternary compounds. *Physica B: Condensed Matter*, 210(1):1–25, 1995.

[5] Keith S Taber. The atom in the chemistry curriculum: Fundamental concept, teaching model or epistemological obstacle? *Foundations of Chemistry*, 5(1):43–84, 2003.

[6] SM Newstead, RAA Kubiak, and EHC Parker. On the practical applications of mbe surface phase diagrams. *Journal of Crystal Growth*, 81(1-4):49–54, 1987.

[7] Iwan N Stranski. Zur theorie des kristallwachstums. *Zeitschrift für physikalische Chemie*, 136(1):259–278, 1928.

[8] JW Matthews and AE Blakeslee. Defects in epitaxial multilayers: I. misfit dislocations. *Journal of Crystal growth*, 27:118–125, 1974.

[9] PB Joyce, TJ Krzyzewski, GR Bell, BA Joyce, and TS Jones. Composition of inas quantum dots on gaas (001): Direct evidence for (in, ga) as alloying. *Physical Review B*, 58(24):R15981, 1998.

[10] David J Griffiths and Darrell F Schroeter. *Introduction to quantum mechanics*. Cambridge University Press, 2018.

[11] Christopher F. Schuck, Robin A. McCown, Ashlie Hush, Austin Mello, Simon Roy, Joseph W. Spinuzzi, Baolai Liang, Diana L. Huffaker, and Paul J. Simmonds. Self-assembly of (111)-oriented tensile-strained quantum dots by molecular beam epitaxy. *Journal of Vacuum Science & Technology B*, 36(3):031803, 2018.

[12] Charles Kittel. Introduction to solid state physics. 1976.

[13] Douglas Walton and Nanning Zhang. The epistemology of scientific evidence. *Artificial Intelligence and Law*, 21(2):173–219, 2013.

[14] Fiora Salis and Roman Frigg. Capturing the scientific imagination. *The scientific imagination*, pages 17–50, 2020.

[15] Andreas Tolk, Martin Ihrig, Ernest H Page, Claudia Szabo, Brian L Heath, Jose J Padilla, E Dante Suarez, Paul Weirich, and Levent Yilmaz. Epistemology

of modeling and simulation. In *2013 Winter Simulations Conference (WSC)*, pages 1152–1166. IEEE, 2013.

[16] Christopher J.B. Ford. Transporting and manipulating single electrons in surface-acoustic-wave minima. *Physica Status Solidi (B) Basic Research*, 254(3), 2017.

[17] Per Delsing, Andrew N. Cleland, Martin J.A. Schuetz, Johannes Knörzer, Géza Giedke, J. Ignacio Cirac, Kartik Srinivasan, Marcelo Wu, Krishna Coimbatore Balram, Christopher Baüerle, Tristan Meunier, Christopher J.B. Ford, Paulo V. Santos, Edgar Cerda-Méndez, Hailin Wang, Hubert J. Krenner, Emeline D.S. Nysten, Matthias Weiß, Geoff R. Nash, Laura Thevenard, Catherine Gourdon, Pauline Rovillain, Max Marangolo, Jean Yves Duquesne, Gerhard Fischerauer, Werner Ruile, Alexander Reiner, Ben Paschke, Dmytro Denysenko, Dirk Volkmer, Achim Wixforth, Henrik Bruus, Martin Wiklund, Julien Reboud, Jonathan M. Cooper, Yong Qing Fu, Manuel S. Brugger, Florian Rehfeldt, and Christoph Westerhausen. The 2019 surface acoustic waves roadmap. *Journal of Physics D: Applied Physics*, 52(35), jul 2019.

[18] Jared Kirschner. Surface Acoustic Wave Sensors (SAWS): Design for Application. Technical report, 2010.

[19] A. Violante, K. Cohen, S. Lazić, R. Hey, R. Rapaport, and P. V. Santos. Dynamics of indirect exciton transport by moving acoustic fields. *New Journal of Physics*, 16, 2014.

[20] Yousun Chung, Hangtian Hou, Seok-Kyun Son, Tzu-Kan Hsiao, Ateeq Nasir, Antonio Rubino, Jonathan P Griffiths, Ian Farrer, David A Ritchie, and

Christopher JB Ford. Quantized charge transport driven by a surface acoustic wave in induced unipolar and bipolar junctions. *Physical Review B*, 100(24):245401, 2019.

[21] Kristen Kaasbjerg, Kristian S. Thygesen, and Antti Pekka Jauho. Acoustic phonon limited mobility in two-dimensional semiconductors: Deformation potential and piezoelectric scattering in monolayer MoS2 from first principles. *Physical Review B - Condensed Matter and Materials Physics*, 87(23), jun 2013.

[22] J. F. Nye. *Physical Properties of Crystals: their representation by tensors and matrices*. Oxford University Press, 1985.

[23] D. Royer, M.-H. Noroy, and M. Fink. Optical generation and detection of elastic waves in solids. *Le Journal de Physique IV*, 04(C7):C7–673–C7–684, jul 1994.

[24] C. Rocke, S. Zimmermann, A. Wixforth, J. P. Kotthaus, G. Böhm, and G. Weimann. Acoustically driven storage of light in a quantum well. *Physical Review Letters*, 78(21):4099–4102, 1997.

[25] Mats Powlowski, Francois Sfigakis, and Na Young Kim. Temperature dependent angular dispersions of surface acoustic waves on GaAs. *Japanese Journal of Applied Physics*, 58(3), mar 2019.

[26] Qing Li, Kathleen Hoogeboom-Pot, Damiano Nardi, Margaret M. Murnane, Henry C. Kapteyn, Mark E. Siemens, Erik H. Anderson, Olav Hellwig, Elizabeth Dobisz, Bruce Gurney, Ronggui Yang, and Keith A. Nelson. Generation and control of ultrashort-wavelength two-dimensional surface acoustic waves

at nanoscale interfaces. *Physical Review B - Condensed Matter and Materials Physics*, 85(19), may 2012.

[27] J. Rudolph, R. Hey, and P. V. Santos. Long-range exciton transport by dynamic strain fields in a GaAs quantum well. *Physical Review Letters*, 99(4):1–4, 2007.

[28] Arthur G. Every, Sara E. Ferry, Penghui Cao, Alejandro Vega-Flick, Michael P. Short, Alexei A. Maznev, Keith A. Nelson, and Cody A. Dennett. Bridging the gap to mesoscale radiation materials science with transient grating spectroscopy. *Physical Review B*, 94(21):1–10, 2016.

[29] Peter Agre, Landon S. King, Masato Yasui, Wm B. Guggino, Ole Petter Ottersen, Yoshinori Fujiyoshi, Andreas Engel, and Søren Nielsen. Aquaporin water channels - From atomic structure to clinical medicine. *Journal of Physiology*, 542(1):3–16, 2002.

[30] Aymeric Ramiere, Ryoto Yanagisawa, Masahiro Nomura, Roman Anufriev, Jeremie Maire, and Sebastian Volz. Heat conduction tuning by wave nature of phonons. *Science Advances*, 3(8):e1700027, 2017.

[31] G. W. Farnell. Properties of Elastic Surface Waves. In *Physical Acoustics*, pages 109–166. 1970.

[32] Y. Sugawara, O. B. Wright, O. Matsuda, M. Takigahira, Y. Tanaka, S. Tamura, and V. E. Gusev. Watching ripples on crystals. *Physical Review Letters*, 88(18):1855041–1855044, 2002.

[33] Lord Rayleigh. On waves propagated along the plane surface of an elastic solid. *Proceedings of the London mathematical Society*, 1(1):4–11, 1885.

[34] Michael A. Stroscio and Mitra Dutta. *Phonons in Nanostructures*. 2009.

[35] H. S. Kim, J. Y. Lin, H. X. Jiang, W. W. Chow, A. Botchkarev, and H. Morkoç. Piezoelectric effects on the optical properties of GaN/AlxGa1-xN multiple quantum wells. *Applied Physics Letters*, 73(23):3426–3428, 1998.

[36] K. Hirakawa and H. Sakaki. Energy relaxation of two-dimensional electrons and the deformation potential constant in selectively doped AlGaAs/GaAs heterojunctions. *Applied Physics Letters*, 49(14):889–891, 1986.

[37] Wenshen Wang, Datong Chen, Harold R. Fetterman, Yongqiang Shi, William H. Steier, Larry R. Dalton, and Pei Ming D. Chow. Optical heterodyne detection of 60 GHz electro-optic modulation from polymer waveguide modulators. *Applied Physics Letters*, 67:1806, 1995.

[38] Cody A. Dennett and Michael P. Short. Time-resolved, dual heterodyne phase collection transient grating spectroscopy. *Applied Physics Letters*, 110(21):0–5, 2017.

[39] David H. Hurley, Ken L. Telschow, and David Cottle. Probing acoustic nonlinearity on lengths scales comparable to material grain dimensions. *Ultrasonics*, 40(1-8):617–620, 2002.

[40] A. R. Lang and Mai Zhen-Hong. Pendellosung interference in the bragg reflexion of x-rays from a crystal surface. *Proceedings of the Royal Society of London. Series A, Mathematical and Physical Sciences*, 368(1734):313–329, 1979.

[41] O. K. Kim and W. G. Spitzer. Infrared reflectivity spectra and Raman spectra

of Ga1-xAlxAs mixed crystals. *Journal of Applied Physics*, 50(6):4362–4370, 1979.

[42] Christopher D. Yerino, Baolai Liang, Diana L. Huffaker, Paul J. Simmonds, and Minjoo Larry Lee. Review Article: Molecular beam epitaxy of lattice-matched InAlAs and InGaAs layers on InP (111)A, (111)B, and (110). *Journal of Vacuum Science & Technology B*, 35(1):010801, 2017.

[43] Saumitra R. Mehrotra, Michael Povolotskyi, Doron Cohen Elias, Tillmann Kubis, Jeremy J.M. Law, Mark J.W. Rodwell, and Gerhard Klimeck. Simulation study of thin-body ballistic n-MOSFETs involving transport in mixed Γ-L valleys. *IEEE Electron Device Letters*, 34(9):1196–1198, 2013.

[44] A. Schliwa, M. Winkelnkemper, A. Lochmann, E. Stock, and D. Bimberg. In(Ga)As/GaAs quantum dots grown on a (111) surface as ideal sources of entangled photon pairs. *Physical Review B*, 80(16):161307(R), oct 2009.

[45] Christopher D. Yerino, Paul J. Simmonds, Baolai Liang, Daehwan Jung, Christian Schneider, Sebastian Unsleber, Minh Vo, Diana L. Huffaker, Sven Höfling, Martin Kamp, and Minjoo Larry Lee. Strain-driven growth of GaAs(111) quantum dots with low fine structure splitting. *Applied Physics Letters*, 105(25):251901, 2014.

[46] N. V. Tarakina, S. Schreyeck, T. Borzenko, C. Schumacher, G. Karczewski, K. Brunner, C. Gould, H. Buhmann, and L. W. Molenkamp. Comparative study of the microstructure of Bi_2Se_3 thin films grown on Si(111) and InP(111) substrates. *Crystal Growth and Design*, 12(4):1913–1918, 2012.

[47] Zhaoquan Zeng, Timothy A. Morgan, Dongsheng Fan, Chen Li, Yusuke Hirono, Xian Hu, Yanfei Zhao, Joon Sue Lee, Jian Wang, Zhiming M. Wang, Shuiqing Yu, Michael E. Hawkridge, Mourad Benamara, and Gregory J. Salamo. Molecular beam epitaxial growth of Bi_2Te_3 and Sb_2Te_3 topological insulators on GaAs (111) substrates: a potential route to fabricate topological insulator p-n junction. *AIP Advances*, 3(7):072112, 2013.

[48] Keiji Ueno, Toshihiro Shimada, Koichiro Saiki, and Atsushi Koma. Heteroepitaxial growth of layered transition metal dichalcogenides on sulfur-terminated GaAs{111} surfaces. *Applied Physics Letters*, 56(4):327–329, 1990.

[49] Suresh Vishwanath, Xinyu Liu, Sergei Rouvimov, Leonardo Basile, Ning Lu, Angelica Azcatl, Katrina Magno, Robert M. Wallace, Moon Kim, Juan-Carlos Idrobo, Jacek K. Furdyna, Debdeep Jena, and Huili Grace Xing. Controllable growth of layered selenide and telluride heterostructures and superlattices using molecular beam epitaxy. *Journal of Materials Research*, 31(7):900–910, 2016.

[50] Yoshimichi Okano, Mitsuhiro Shigeta, Hiroyuki Seto, Hisashi Katahama, Shiro Nishine, and Isao Fujimoto. Incorporation Behavior of Si Atoms in the Molecular Beam Epitaxial Growth of GaAs on Misoriented (111)A Substrates. *Japanese Journal of Applied Physics*, 29(8):L1357–L1359, 1990.

[51] D.A. Woolf, D.I. Westwood, and R.H. Williams. The homoepitaxial growth of GaAs(111)A and (111)B by molecular beam epitaxy: an investigation of the temperature-dependent surface reconstructions and bulk electrical conductivity transitions. *Semiconductor Science and Technology*, 8(6):1075, 1993.

[52] M R Fahy, K Sato, and B A Joyce. Reflection high-energy electron diffraction intensity oscillations during the growth by molecular beam epitaxy of GaAs(111). *Applied Physics Letters*, 64:190–192, 1994.

[53] Kenji Sato, Michael R. Fahy, and Bruce A. Joyce. The growth of high quality GaAs on GaAs(111)A. *Japanese Journal of Applied Physics*, 33:L905–L907, 1994.

[54] P Chen, K C Rajkumar, and A Madhukar. Growth control of GaAs epilayers with specular surface free of pyramids and twins on nonmisoriented (111)B substrates. *Applied Physics Letters*, 58:1771–1773, 1991.

[55] Christelle Guerret-Piecourt and Chantal Fontaine. Temperature effect on surface flatness of molecular beam epitaxy homoepitaxial layers grown on nominal and vicinal (111)B GaAs substrates. *Journal of Vacuum Science & Technology B*, 16:204–209, 1998.

[56] Paul J. Simmonds and Minjoo Larry Lee. Self-assembly on (111)-oriented III-V surfaces. *Applied Physics Letters*, 99(12):10–13, 2011.

[57] Paul J Simmonds and Minjoo Larry Lee. Tensile-strained growth on low-index GaAs. *Journal of Applied Physics*, 112:054313, 2012.

[58] H. Q. Hou and C. W. Tu. Homoepitaxial growth of InP on (111)B substrates by gas-source molecular beam epitaxy. *Applied Physics Letters*, 62(3):281, 1993.

[59] Ida Sadeghi, Man Chun Tam, and Zbigniew Roman Wasilewski. On the optimum off-cut angle for the growth on InP(111)B substrates by molecular beam epitaxy. *Journal of Vacuum Science & Technology B*, 37(3):031210, 2019.

[60] Koichi Sugiyama. Surface reconstruction and morphology of InAs grown by molecular beam epitaxy. *Journal of Crystal Growth*, 75(3):435–440, 1986.

[61] J. A. Dura, J. T. Zborowski, and T. D. Golding. Molecular beam epitaxy study of InAs/GaSb heteroepitaxy on the (111)A and (111)B orientations. *Materials Research Society Symposium Proceedings*, 263(1):35–40, 1992.

[62] J. Yang, C. Nacci, J. Martínez-Blanco, K. Kanisawa, and S. Fölsch. Vertical manipulation of native adatoms on the InAs(111)A surface. *Journal of Physics Condensed Matter*, 24(35), 2012.

[63] Kiyoshi Kanisawa. Correlation between adatom dynamics and electron accumulation at the epitaxial InAs(111)A surface. *Journal of Crystal Growth*, 378:8–12, 2013.

[64] A. Taguchi and K. Kanisawa. Stable reconstruction and adsorbates of InAs(1 1 1)A surface. *Applied Surface Science*, 252(15):5263–5266, 2006.

[65] Herbert Kroemer. The 6.1 Å family (InAs, GaSb, AlSb) and its heterostructures: A selective review. *Physica E: Low-Dimensional Systems and Nanostructures*, 20(3-4):196–203, 2004.

[66] Kristiaan Neyts. Microcavity effects and the outcoupling of light in displays and lighting applications based on thin emitting films. *Applied Surface Science*, 244(1-4):517–523, 2005.

[67] Brian B. Haidet, Leland Nordin, Aaron J. Muhowski, Kevin D. Vallejo, Eamonn T. Hughes, Jarod Meyer, Paul J. Simmonds, Daniel Wasserman, and

Kunal Mukherjee. Interface structure and luminescence properties of epitaxial PbSe films on InAs(111)A. *Journal of Vacuum Science & Technology A*, 39(2):023404, 2021.

[68] Christopher F. Schuck, Simon K. Roy, Trent Garrett, Qing Yuan, Ying Wang, Carlos I. Cabrera, Kevin A. Grossklaus, Thomas E. Vandervelde, Baolai Liang, and Paul J. Simmonds. Anomalous Stranski-Krastanov growth of (111)-oriented quantum dots with tunable wetting layer thickness. *Scientific Reports*, 9:18179, 2019.

[69] Y. H. Huo, B. J. Witek, S. Kumar, J. R. Cardenas, J. X. Zhang, N. Akopian, R. Singh, E. Zallo, R. Grifone, D. Kriegner, R. Trotta, F. Ding, J. Stangl, V. Zwiller, G. Bester, A. Rastelli, and O. G. Schmidt. A light-hole exciton in a quantum dot. *Nature Physics*, 10(1):46–51, 2013.

[70] Rutger Vrijen and Eli Yablonovitch. A spin-coherent semiconductor photodetector for quantum communication. *Physica E*, 10(4):569–575, 2001.

[71] Paul J Simmonds, Christopher D Yerino, Meng Sun, Baolai Liang, Diana L Huffaker, Vitaliy G Dorogan, Yuriy Mazur, Gregory Salamo, and Minjoo Larry Lee. Tuning Quantum Dot Luminescence Below the Bulk Band Gap Using Tensile Strain. *ACS Nano*, 7(6):5017–5023, 2013.

[72] Christopher D Yerino, Paul J Simmonds, Baolai Liang, Vitaliy G Dorogan, Morgan E Ware, Yuriy I Mazur, Daehwan Jung, Diana L Huffaker, Gregory J Salamo, and Minjoo Larry Lee. Tensile GaAs(111) quantum dashes with tunable luminescence below the bulk bandgap. *Applied Physics Letters*, 105:071912, 2014.

[73] Yu Yao, Anthony J. Hoffman, and Claire F. Gmachl. Mid-infrared quantum cascade lasers. *Nature Photonics*, 6(7):432–439, 2012.

[74] A. A. Toropov, O. G. Lyublinskaya, B. Ya. Meltser, V. A. Solov'ev, A. A. Sitnikova, M. O. Nestoklon, O. V. Rykhova, S. V. Ivanov, K. Thonke, and R. Sauer. Tensile-strained GaAs quantum wells and quantum dots in a GaAsxSb1-x matrix. *Physical Review B*, 70(20):205314, nov 2004.

[75] A. Gassenq, T. Taliercio, L. Cerutti, A.N. Baranov, and E. Tournié. Mid-IR lasing from highly tensile-strained, type II, GaInAs/GaSb quantum wells. *Electronics Letters*, 45(25):1320, 2009.

[76] T.C. Lin, Y.H. Wu, L.C. Li, Y.T. Sung, S.D. Lin, L. Chang, Y.W. Suen, and C.P. Lee. Electron delocalization of tensily strained GaAs quantum dots in GaSb matrix. *Journal of Applied Physics*, 108(12):123503, dec 2010.

[77] A. Lenz, E. Tournié, J. Schuppang, M. Dähne, and H. Eisele. Atomic structure of tensile-strained GaAs/GaSb(001) nanostructures. *Applied Physics Letters*, 102(10):102105, 2013.

[78] D Pachinger, H Lichtenberger, G Chen, J Stangl, G Hesser, and F Schäffler. MBE growth conditions for Si island formation on Ge (001) substrates. *Thin Solid Films*, 517(1):62–64, 2008.

[79] J. B. Rodriguez, P. Christol, L. Cerutti, F. Chevrier, and A. Joullié. MBE growth and characterization of type-II InAs/GaSb superlattices for mid-infrared detection. *Journal of Crystal Growth*, 274(1-2):6–13, 2005.

[80] Kevin D Vallejo, Trent A Garrett, Kathryn E Sautter, Kevin Saythavy, Baolai Liang, and Paul J Simmonds. InAs(111)A homoepitaxy with molecular beam epitaxy. *Journal of Vacuum Science & Technology B, Nanotechnology and Microelectronics: Materials, Processing, Measurement, and Phenomena*, 37(6):061810, 2019.

[81] Anthony A Clifford. *Multivariate error analysis: a handbook of error propagation and calculation in many-parameter systems*. Applied Science Publ., 1973.

[82] P. J. Simmonds, H. E. Beere, H. W. Li, P. See, A. J. Shields, and D. A. Ritchie. Growth by molecular beam epitaxy of self-assembled InAs quantum dots on InAlAs and InGaAs lattice-matched to InP. *Journal of Vacuum Science & Technology B*, 25(3):1044–1048, 2007.

[83] Hanxuan Li, Ju Wu, Bo Xu, Jiben Liang, and Zhanguo Wang. Ordered InAs quantum dots in InAlAs matrix on (001) InP substrates grown by molecular beam epitaxy. *Applied Physics Letters*, 72(17):2123–2125, 1998.

[84] D. Leonard, K. Pond, and P.M. Petroff. Critical layer thickness for self-assembled InAs islands on GaAs. *Physical Review B*, 50(16):11687, 1994.

[85] A.G. Cullis, D.J. Norris, T. Walther, M.A. Migliorato, and M. Hopkinson. Stranski-Krastanow transition and epitaxial island growth. *Physical Review B*, 66(8):081305(R), aug 2002.

[86] Yuhai Tu and J. Tersoff. Origin of Apparent Critical Thickness for Island Formation in Heteroepitaxy. *Physical Review Letters*, 93(21):216101, nov 2004.

[87] A. Madhukar, Q. Xie, P. Chen, and A. Konkar. Nature of strained InAs three-dimensional island formation and distribution on GaAs(100). *Applied Physics Letters*, 64(20):2727–2729, 1994.

[88] Sergio Bietti, Luca Esposito, Alexey Fedorov, Andrea Ballabio, Andrea Martinelli, and Stefano Sanguinetti. Characterization and Effect of Thermal Annealing on InAs Quantum Dots Grown by Droplet Epitaxy on GaAs(111)A Substrates. *Nanoscale Research Letters*, 10(1):247, 2015.

[89] Chi Kuang Sun, Jian Chin Liang, and Xiang Yang Yu. Coherent Acoustic Phonon Oscillations in Semiconductor Multiple Quantum Wells with Piezoelectric Fields. *Physical Review Letters*, 84(1):179–182, 2000.

[90] Kevin D Vallejo, Trent A Garrett, Carlos I Cabrera, Madison D Drake, Baolai Liang, and Paul J Grossklaus, Kevin A Simmonds. Tensile-strained self-assembly of InGaAs on InAs(111)A. *Journal of Vacuum Science & Technology B, Nanotechnology and Microelectronics: Materials, Processing, Measurement, and Phenomena*, Manuscript in Preparation, 2021.

[91] Brian B. Haidet, Leland Nordin, Aaron Muhowski, Kevin D. Vallejo, Eamonn T. Hughes, Jarod Meyer, Paul J. Simmonds, Daniel Wasserman, and Kunal Mukherjee. Interface structure and luminescence properties of epitaxial PbSe films on InAs(111)A. *Journal of Vacuum Science & Technology A*, In Review, 2020.

[92] Christopher F Schuck, Simon K Roy, Trent Garrett, Qing Yuan, Ying Wang, Carlos I Cabrera, Kevin A Grossklaus, Thomas E Vandervelde, Baolai Liang,

and Paul J Simmonds. Anomalous Stranski-Krastanov growth of (111)-oriented quantum dots with tunable wetting layer thickness. *Scientific Reports*, 9(1):1–10, 2019.

[93] Justin C. Norman, Daehwan Jung, Zeyu Zhang, Yating Wan, Songtao Liu, Chen Shang, Robert W. Herrick, Weng W. Chow, Arthur C. Gossard, and John E. Bowers. A review of high-performance quantum dot lasers on silicon. *IEEE Journal of Quantum Electronics*, 55(2):2000511, 2019.

[94] I. Vurgaftman, J. R. Meyer, and L. R. Ram-Mohan. Band parameters for III-V compound semiconductors and their alloys. *Journal of Applied Physics*, 89(11 I):5815–5875, 2001.

[95] T Taliercio, A Gassenq, E Luna, A Trampert, and E Tournié. Highly tensile-strained, type-ii, ga 1- x in x as/gasb quantum wells. *Applied Physics Letters*, 96(6):062109, 2010.

[96] Ya V Terent'ev, AA Toropov, B Ya Meltser, AN Semenov, VA Solov'ev, IV Sedova, AA Usikova, and SV Ivanov. Spin injection in gaas/gasb quantum-well heterostructures. *Semiconductors*, 44(2):194–197, 2010.

[97] N. N. Ledentsov, J. Böhrer, M. Beer, F. Heinrichsdorff, M. Grundmann, D. Bimberg, S. V. Ivanov, B. Ya. Meltser, S. V. Shaposhnikov, I. N. Yassievich, N. N. Faleev, P. S. Kop'ev, and Zh. I. Alferov. Radiative states in type-ii gasb/gaas quantum wells. *Phys. Rev. B*, 52:14058–14066, Nov 1995.

[98] KF Longenbach and WI Wang. Algasb/gasb diodes grown by molecular-beam epitaxy. *Applied physics letters*, 59(9):1117–1119, 1991.

[99] Andre Proessdorf, Frank Grosse, Wolfgang Braun, Ferhat Katmis, Henning Riechert, and Oleksandr Romanyuk. Analysis of GaSb and AlSb reconstructions on GaSb(111) A- and B-oriented surfaces by azimuthal-scan reflection high-energy electron diffraction. *Physical Review B - Condensed Matter and Materials Physics*, 83(15):1–11, 2011.

[100] M Lee, DJ Nicholars, KE Singer, and B Hamilton. A photoluminescence and hall-effect study of gasb grown by molecular beam epitaxy. *Journal of Applied Physics*, 59(8):2895–2900, 1986.

[101] Kathryn E Sautter, Christopher F Schuck, Trent A Garrett, Ariel E Weltner, Kevin D Vallejo, Dingkun Ren, Baolai Liang, Kevin A Grossklaus, Thomas E Vandervelde, and Paul J Simmonds. Self-assembly of tensile-strained Ge quantum dots on InAlAs(111)A. *Journal of Crystal Growth*, page 125468, 2020.

[102] Joon Sue Lee, Borzoyeh Shojaei, Mihir Pendharkar, Anthony P McFadden, Younghyun Kim, Henri J Suominen, Morten Kjaergaard, Fabrizio Nichele, Hao Zhang, Charles M Marcus, et al. Transport studies of epi-al/inas two-dimensional electron gas systems for required building-blocks in topological superconductor networks. *Nano letters*, 19(5):3083–3090, 2019.

[103] Natalia Olszowska, Jakub Lis, Piotr Ciochon, Łukasz Walczak, Enrique G Michel, and Jacek J Kolodziej. Effect of a skin-deep surface zone on the formation of a two-dimensional electron gas at a semiconductor surface. *Physical Review B*, 94(11):115305, 2016.

[104] Yuval Oreg, Gil Refael, and Felix Von Oppen. Helical liquids and majorana bound states in quantum wires. *Physical review letters*, 105(17):177002, 2010.

[105] Henri J Suominen, Morten Kjaergaard, Alexander R Hamilton, Javad Shabani, Chris J Palmstrøm, Charles M Marcus, and Fabrizio Nichele. Zero-energy modes from coalescing andreev states in a two-dimensional semiconductor-superconductor hybrid platform. *Physical review letters*, 119(17):176805, 2017.

[106] L. Olsson, C. B.M. Andersson, M. C. Håkansson, J. Kanski, L. Ilver, and U. O. Karlsson. Charge accumulation at InAs surfaces. *Physical Review Letters*, 76(19):3626–3629, 1996.

[107] Richard Nötzel and Klaus H Ploog. Mbe of quantum wires and quantum dots. *Journal of crystal growth*, 227:8–12, 2001.

[108] Claus F. Klingshirn. *Semiconductor Optics*. Springer-Verlag Berlin Heidelbeg, Berlin, 3rd edition, 2007.

[109] C. Weisbuch. Fundamental Properties of III-V semiconductor two-dimensional quantized structures. In *Semiconductors and Semimetals vol. 24*. 1987.

[110] DJ BenDaniel and CB Duke. Space-charge effects on electron tunneling. *Physical review*, 152(2):683, 1966.

[111] Arpan Deyasi and Swapan Bhattacharyya. Composite effect of bendaniel duke boundary condition and material composition on eigenenergy of multiple quantum well structure. *Int. J. Soft Comput. Eng.*, 1(4):67–71, 2011.

[112] Ashutosh Kumar Giri, Himanshu Kumar Pandey, Abhishek Ranjan Singh, and Pramendra Ranjan Singh. Size quantization and electron transport in quantum dots.

APPENDIX A:

DERIVATIONS AND PROGRAMMING CODE

A.1 Phonon Dispersion Relation Derivation

From Stroscio [34], the longitudinal displacements of a 1D chain of atoms with two different masses m and M are taken to be

$$u_{2r} = A_1 e^{i(2rqa - \omega t)} \tag{A.1}$$

and

$$u_{2r+1} = A_2 e^{i[(2r+1)qa - \omega t)]} \tag{A.2}$$

where q is the phonon wavevector and ω is its frequency. Recalling Newton's second law ($F = ma$) we can write

$$m\frac{d^2 u_{2r}}{dt^2} = -\alpha(u_{2r} - u_{2r-1}) - \alpha(u_{2r} - u_{2r+1}) \tag{A.3}$$

$$= \alpha(u_{2r+1} + u_{2r-1} - 2u_{2r}) \tag{A.4}$$

$$\tag{A.5}$$

and

$$M\frac{d^2 u_{2r+1}}{dt^2} = -\alpha(u_{2r+1} - u_{2r}) - \alpha(u_{2r+1} - u_{2r+2}) \tag{A.6}$$

$$= \alpha(u_{2r+2} + u_{2r} - 2u_{2r+1}) \tag{A.7}$$

Substituting the displacements into this equations we obtain

$$-m\omega^2 A_1 = \alpha A_2(e^{iqa} + e^{-iqa}) - -2\alpha A_1 \tag{A.8}$$

(A.9)

and

$$-M\omega^2 A_2 = \alpha A_1(e^{iqa} + e^{-iqa}) - -2\alpha A_2 \tag{A.10}$$

Combining these two equations to solve for ω^2 and eliminating A_1 and A_2 we obtain

$$\omega^2 = \alpha\left(\frac{1}{m} + \frac{1}{M}\right) \pm \alpha\left[\left(\frac{1}{m} + \frac{1}{M}\right)^2 - \frac{4\sin^2 qa}{mM}\right]^{1/2} \tag{A.11}$$

The higher frequency solution is known as the optical mode since for many semiconductors its frequency is in the terahertz range which happens to coincide with the infrared portion of the electromagnetic spectrum. The lower frequency solution is known as the acoutic mode. Since we only dealt with longitudinal displacements, these solutions correspond to the longitudinal optic and the longitudinal acoustic modes of the linear chain lattice.

Phonon confinement in quantum wells results from the reduction of the travel distance allowed for wave propagation. In superlattices, the Brillouin zone limits get reduced from $-\pi/a \leqslant k \leqslant \pi/a$ to $-\pi/l_z \leqslant k \leqslant \pi/l_z$ where l_z is the superlattice period. Acoustic phonon branches in this regime undergo backfolding.

Polar Semiconductor Dispersion In polar semiconductors the masses m and M carry opposite charges, e^* and $-e^*$ as a result of charge redistribution. When there is an electric field E present we need augment the previous force equation with terms describing the interaction with the charge. Using a long-wavelength limit for E the equations become

$$-m\omega^2 u_{2r} = m\frac{d^2 u_{2r}}{dt^2} = \alpha(u_{2r+1} + u_{2r-1} - 2u_{2r}) + e^*E \tag{A.12}$$

(A.13)

and

$$-M\omega^2 u_{2r+1} = m\frac{d^2 u_{2r+1}}{dt^2} = \alpha(u_{2r+2} + u_{2r} - 2u_{2r+1}) - e^*E \tag{A.14}$$

Also in this long wavelength approximation, the displacement of each atom with the same mass is the same. This implies that the wavevector q tends to zero ($q \to 0$). Denoting the displacement of even-numbered sites by u_1 and the odd-numbered ones by u_2 we obtain

$$-m\omega^2 u_1 = 2\alpha(u_2 - u_1) + e^*E \tag{A.15}$$

(A.16)

and

$$-M\omega^2 u_2 = 2\alpha(u_1 - u_2) - e^*E \tag{A.17}$$

from which it can be deduced that $mu_1 = -Mu_2$, thus

$$-(\omega^2 - \omega_0^2)u_1 = e^* \frac{E}{m} \tag{A.18}$$

$$\tag{A.19}$$

and

$$-(\omega^2 - \omega_0^2)u_2 = -e^* \frac{E}{M} \tag{A.20}$$

where $\omega_0 = 2\alpha(1/m + 1/M)$ is the resonant frequency squared in the absence of Coulomb effects. The electric polarization P produced in such a polar diatomic lattice is given by

$$P = \frac{Ne^*(u_1 - u_2)}{\epsilon} = \frac{1}{\epsilon} \frac{Ne^{*2}}{(\omega_0^2 - \omega^2)} \left(\frac{1}{m} + \frac{1}{M} \right) E \tag{A.21}$$

A.2 Surface Acoustic Wave Theory

From Klingshirn [108], let us consider a one-dimensional string. Two types of waves can propagate along it: ones where particle is parallel to the direction of wave propagation (longitudinal) and one where it is perpendicular to it (tranversal). The mass density of the string is ρ, the cross-section A and the infinitesimal displacement is dz. Using these parameters Newton's equation of motion becomes

$$F = dm \frac{\partial^2 u}{\partial t^2} = \rho A \cdot dz \cdot \frac{\partial^2 u}{\partial t^2} \tag{A.22}$$

Force is then connected to the elasticity modulus by

$$F = A \cdot E\frac{\partial^2 u}{\partial t^2}\ since\ \sigma(z) = E\frac{\partial u}{\partial z} \tag{A.23}$$

Putting these equations together yields

$$\rho\frac{\partial^2 u}{\partial t^2} = E\frac{\partial u}{\partial z} \tag{A.24}$$

known as the standard harmonic wave equation A more general -and rigorous- approach to deriving the wave equation is as follows: A body in which no gravitational or inertial forces act can have forces acting on it described by

$$F = \int_V f dV$$

In component form this would be

$$F_i = \int_V f_i dV$$

However, forces act on the surfaces of the body giving us

$$F_i = \oint \sigma_i dS$$

where σ_i is a force acting on a surface unit. The infinitesimally small area dS can be described by the normal vector to the surface $\bar{n}$, which turns our equation into

$$d\bar{S} = \bar{n}dS \rightarrow dS_k = n_k dS$$

In component form. Putting these expressions together we arrive to

$$\sigma_i = \sigma_{ik} n_k \rightarrow F_i = \oint \sigma_{ik} n_k dS = \oint \sigma_{ik} dS_k$$

It then follows that

$$\int_V f_i dV = \oint \sigma_{ik} dS_k$$

By virtue of Gauss' theorem, we recall

$$\begin{aligned} \oint \phi dS_k &= \int \frac{\partial \phi}{\partial x_k} dV \\ \rightarrow \oint \sigma_{ik} dS_k &= \frac{d}{dx_k} \sigma_{ik} dV \\ \rightarrow \int_V f_i dV = \frac{d}{dx_k} \sigma_{ik} dV \therefore f_i &= \frac{d\sigma_{ik}}{dx_k} \end{aligned}$$

Invoking d'Alambert's principle, all forces equaling zero serves as condition of equilibrium:

- Weigth per unit volume: ρg
- Inertial forces per unit volume: $\rho \frac{\partial^2 \bar{r}}{\partial t^2}$
- External forces per unit volume: f_i

Putting these forces together we obtain the equation of motion

$$\begin{aligned} \rho g - \rho \frac{\partial^2 \bar{r}}{\partial t^2} + f_i = 0 \\ \textit{or in component form} \quad \rho g - \rho \frac{\partial^2 x_i}{\partial t^2} + f_i = 0 \\ \rightarrow \rho g - \rho \frac{\partial^2 x_i}{\partial t^2} = f_i = \frac{d\sigma_{ik}}{dx_k} \end{aligned}$$

Now, taking the small forces to obey Hooke's Law for small deformations of the form

$$\sigma ik = \sigma_{ik}(\gamma_{lm})$$

We expand this as a function of γ_{lm} as a McLaurin series

$$\sigma_{ik} = \sigma_{ik}(0) + \frac{\partial \sigma_{ik}}{\partial \gamma_{lm}}\Big|_{\gamma_{lm=0}} \gamma_{lm} + \ldots$$

Keeping only the first term in the expansion to respect the linear theory of elasticity, and considering the boundary condition where no stress means no deformation we obtain

$$\begin{aligned} \sigma_{ik}(0) = 0 \\ \rightarrow \sigma_{ik} = c_{ijkl}\gamma_{lm} \\ \textit{where} \quad c_{ijkl} = \frac{\partial}{\partial \gamma_{lm}} \sigma_{ik}\Big|_{\gamma_{lm}=0} \end{aligned}$$

The elasticity equation is then formed by the stress tensor components T_{ij} defined

as

$$T_{ij} = c_{ijkl}\frac{\partial u_l}{\partial x_k}$$

Using x_2 as our depth dimension we obtain the condition

$$T_{i2} = c_{i2kl}\frac{\partial u_l}{\partial x_k} = 0$$

The elasticity equation is the

$$\rho\frac{\partial^2 u_i}{\partial t^2} = c_{ijkl}\frac{\partial^2 u_l}{\partial x_j \partial x_k}$$

and a proposed solution to this equation, having a displacement in the x_1 direction and an amplitude decaying exponentially in the depth direction takes the form

$$u_i = u_i' e^{-iqkx_2} e^{i(\omega t - kx_1)}$$

Substituting said solution onto the equation we obtain

$$\begin{aligned} \rho\frac{\partial^2}{\partial t^2}u_i &= c_{ijkl}\frac{\partial}{\partial x_j}\frac{\partial}{\partial x_k}u_l \\ \rightarrow \rho\frac{\partial^2}{\partial t^2}u_i' e^{-iqkx_2} e^{i(\omega t - kx_1)} &= c_{ijkl}\frac{\partial}{\partial x_j}\frac{\partial}{\partial x_k}u_i' e^{-iqkx_2} e^{i(\omega t - kx_1)} \\ \rho u_i' e^{-iqkx_2} e^{-ikx_1}\frac{\partial^2}{\partial t^2}e^{i\omega t} &= c_{ijkl}u_i' e^{i\omega t}\frac{\partial^2}{\partial x_k x_j}e^{-iqkx_2} e^{-ikx_1} \end{aligned}$$

At this point we can observe that all terms containing x_3 derivatives will become zero,

leaving us with a right hand side array of the form

$$\rho u_i' e^{-iqkx_2} e^{-ikx_1}(-\omega^2)e^{i\omega t} =$$
$$\Big(c_{i11l}\frac{\partial^2}{\partial x_1^2} + c_{i12l}\frac{\partial^2}{\partial x_1 \partial x_2} + c_{i21l}\frac{\partial^2}{\partial x_2 \partial x_1} + c_{i22l}\frac{\partial^2}{\partial x_2^2}\Big)u_i' e^{i\omega t} e^{-iqkx_2} e^{-ikx_1}$$

Taking the appropriate derivatives on the RHS we obtain the expression

$$= c_{i11l}(-ik)^2 u_i + c_{i21l}(-qk^2)u_i + c_{i12l}(-qk^2)u_i + c_{i22l}(-iqk)^2$$
$$= \Big[-k^2 c_{i11l} - qk^2(c_{i21l} + c_{i12l}) - q^2k^2 c_{i22l}\Big] u_i$$

And then regrouping on the LHS we obtain

$$-\omega^2 \rho u_i = -k^2 \Big[c_{i11l} + (c_{i21l} + c_{i12l})q + c_{i22l}q^2\Big] u_i$$
$$\frac{\omega^2}{k^2}\rho u_i = \Big[c_{i11l} + (c_{i21l} + c_{i12l})q + c_{i22l}q^2\Big] u_i$$

If we set $V = \frac{\omega}{k}$, $\zeta = \rho V^2$ and $\Gamma_{il} = c_{i11l} + (c_{i21l} + c_{i12l})q + c_{i22l}q^2$ we end up with the Christoffel equations

$$(\Gamma_{il} - \zeta\delta_{il})u_i = 0$$

These equations provide the wavevelocities in GaAs/$Al_xGa_{1-x}As$ and are given by

$$Along\ [100] \begin{cases} V_L = \sqrt{\frac{c_{11}}{\rho}} = 4.73 \times 10^5 \frac{cm}{s} \\ V_T = \sqrt{\frac{c_{44}}{\rho}} = 3.35 \times 10^5 \frac{cm}{s} \end{cases}$$

$$Along\ [110] \begin{cases} V_L = \sqrt{\frac{c_{11}+c_{12}+2c_{44}}{2\rho}} = 5.24 \times 10^5 \frac{cm}{s} \\ V_T = \sqrt{\frac{c_{44}}{\rho}} = 3.35 \times 10^5 \frac{cm}{s} \end{cases}$$

A.3 Energy Quantization in Quantum Wells

In this section I will explain how we can solve for the energy states of a charge carrier inside a quantum well. We begin with the description of the evolution of its wavefunction (a mathematical entity whose squared inner product produces the probability of finding the charge carrier within a certain value) as described by the Schrödinger equation. This description is valid as a mathematical description of the landscape created when there are two abrupt interfaces grown with atomically discrete steps, such as those created using MBE. Starting with the time-dependent Schrödinger equation

$$\Big(-\frac{\hbar^2}{2m}\nabla^2 + V(r,t)\Big)\Psi(r,t) = i\hbar\frac{\partial \Psi(r,t)}{\partial t} \tag{A.25}$$

We consider a time-independent potential barrier in each layer, i.e. $V(r,t) = V(r)$ for which the equation has a solution of the form

$$\Psi(r,t) = \mathbf{Re}[\psi(r)e^{\frac{-iEt}{\hbar}}]$$

Plugging this solution back into equation A.25 we obtain

$$-\frac{\hbar^2}{2m}\nabla^2\psi(r) + V(r)\psi(r) = E\psi(r) \tag{A.26}$$

which is known as the time-harmonic Schrödinger equation. In order to solve this new equation, we must realize the conditions of the potential experienced by the charge carriers at each point as they go across the material interface:

$$V = \begin{cases} V_0 & z < -\frac{L}{2} \\ 0 & -\frac{L}{2} < z < \frac{L}{2} \\ V_0 & z > \frac{L}{2} \end{cases} \tag{A.27}$$

We can then simplify equation A.26 to be a one-dimensional problem because the interfaces exist normal to the growth direction, and there is material isotropy on the planes parallel to the substrate. Our one-dimensional Schrödinger equation (equation A.26) then takes the form

$$-\frac{\hbar^2}{2m}\frac{d^2}{dz^2}\psi(z) + V(z)\psi(z) = E\psi(z) \tag{A.28}$$

and we can now begin to look for solutions in the different regions of our structure.

Inside the well In the region ($-\frac{L}{2} < z < \frac{L}{2}$) the potential $V(z) = 0$, and we can

simply write

$$-\frac{\hbar^2}{2m}\frac{d^2}{dz^2}\psi(z) + 0\cdot\psi(z) = E\psi(z)$$
$$-\frac{\hbar^2}{2m}\psi''(z) = E\psi(z)$$
$$\psi''(z) = -\frac{2mE}{\hbar^2}\psi(z)$$

We define

$$k^2 = \frac{2mE}{\hbar^2}$$
$$\rightarrow \psi''(z) = -k^2\psi(z)$$

and propose a solution of the form

$$\psi(z) = A\cos(kz) + B\sin(kz)$$

We then take this solution and verify that

$$\psi'(z) = -Ak\sin(kz) + Bk\cos(kz) \rightarrow \psi''(z) = -k^2(A\cos(kz) + B\sin(kz))\checkmark$$

We can now divide this solution into even and odd parts (our initial proposed solution

is itself a linear combination of these two) and take the same approach for the other regions in the structure.

Outside the well In this region the potential $V(z) \neq 0$. We can still use the same approach used for the center region, for the potential is a constant on the external regions of the structure.

For $z > \frac{L}{2}$

$$-\frac{\hbar^2}{2m}\frac{d^2}{dz^2}\psi(z) + V_0\psi(z) = E\psi(z)$$
$$-\frac{\hbar^2}{2m}\psi''(z) = (E - V_0)\psi(z)$$
$$\psi''(z) = -\frac{2m(E - V_0)}{\hbar^2}\psi(z)$$

we can then define

$$\alpha^2 = \frac{2m(V_0 - E)}{\hbar^2}$$
$$\rightarrow \psi''(z) = \alpha^2\psi(z)$$

The proposed solution by Weisbuch [109] is

$$\psi(z) = Be^{-\alpha(z-\frac{L}{2})}$$

for which we can verify that

$$\psi'(z) = -B\alpha e^{-\alpha(z-\frac{L}{2})} \rightarrow \psi''(z) = \alpha^2 B e^{-\alpha(z-\frac{L}{2})} \checkmark$$

The same procedure can be done for the other side of the well and obtain the solution

$$\psi(z) = Be^{\alpha(z+\frac{L}{2})}$$

Interfaces At the point where the heterojunction occurs, we must be aware of the different effective masses that exist on each side of the interface. The resistance to movement that carriers experience in each material have different values due to the crystal structure (atomic species and arrangement) they encounter on their path. A way of calculating the allowed energy states in these simple QW heterostructures is considering the boundary conditions and ensure the continuity of the matter and probability densities across the interfaces. This approach was first proposed by Ben-Daniel and Duke[110] and has been extensively cited in most approaches to solve this problem.[108, 110, 111, 109]

The two conditions stated above can be written in equation form as

$$\psi_{II}(\frac{L}{2}) = \psi_{III}(\frac{L}{2}) \tag{A.29}$$

$$\frac{1}{m_A^*}\frac{\partial \psi_{II}}{\partial z} = \frac{1}{m_B^*}\frac{\partial \psi_{III}}{\partial z} \tag{A.30}$$

Where we can then plug the wavefunctions we derived earlier for each region

$$A\cos(kz) = B \quad \because e^{-\alpha(\frac{L}{2}-\frac{L}{2})} = 1$$
$$-\frac{1}{m_A^*}kA\sin(\frac{kL}{2}) = -\alpha\frac{1}{m_B^*}B$$

Substituting B into our first boundary condition

$$\frac{k}{m_A^*}A\sin(\frac{kL}{2}) = \frac{-\alpha}{m_B^*}A\cos(\frac{kL}{2})$$
$$-\frac{k}{m_A^*}\sin(\frac{kL}{2}) = \frac{\alpha}{m_B^*}\cos(\frac{kL}{2})$$

Hence our even solution is

$$\rightarrow -\frac{\alpha}{m_B^*} + \frac{k}{m_A^*}\tan\left(\frac{kL}{2}\right) = 0 \tag{A.31}$$

And a similar treatment for the odd components of our solutions yields

$$\rightarrow \frac{k}{m_A^*}\cot(\frac{kL}{2}) = -\frac{\alpha}{m_B^*} \tag{A.32}$$

From Klingshirn [108], we have that the effective mass of electrons and holes is given

by

$$\frac{1}{m_{eff}} = \frac{1}{\hbar}\frac{\partial^2 E}{\partial k^2} \tag{A.33}$$

A generalization of this equation relates the effective mass tensor to the direction of propagation

$$\frac{1}{m_{eff}} = \frac{1}{\hbar}\frac{\partial^2 E}{\partial k_i \partial k_j};\ i,j = x,y,z \tag{A.34}$$

The bands of semiconductors tend to be parabolic in the vicinity of band extrema, which are the most important points for optical and transport properties. This leads to the effective mass approximation due to the effective masses being constant in these regions. An interesting result outside the scope of the present study is the polaron, defined as the entity of a charge carrier plus a "phonon cloud" resulting from the Coulombic interactions between the ionic cores and the free carrier.

Carrier	GaAs m_e^*	GaAs m_h^*	AlAs m_e^*	AlAs m_h^*
Value	0.0665 m_e	0.53 m_e	0.15 m_e	0.5 m_e

Table A.1: Effective masses used for calculation of energy levels, from Nakwaski[4]

We can solve these equations numerically using the Newton-Rhapson method, which applies to a polynomial function $f(x)$ upon which a Taylor expansion is done around the point $x = x_0 + \epsilon$ This approache takes the form

$$f(x_0 + \epsilon) = f(x_0) + f'(x_0)\epsilon + \frac{1}{2}f''(x_0)\epsilon^2 \cdots$$

Taking only the first order expansion we obtain an equation which is equivalent to a tangent line to the original function.

$$f(x_0+\epsilon) \approx f(x_0) + f'(x_0)\epsilon$$
$$\rightarrow \epsilon = -\frac{f(x_0)}{f'(x_0)}$$

which is equivalent to the iterative version

$$\epsilon_n = -\frac{f(x_n)}{f'(x_n)} \rightarrow x_{n+1} = x_n - \frac{f(x_n)}{f'(x_n)}$$

Using Mathematica's function *MethodaTangente*, which is an iterative function where the arguments are [*initialguess,precision*], we can grab a value close to the graphical zero and our result will be the energy above the GaAs base bandgap (see appendix section A.5).

A.3.1 Energy Levels in Quantum Dots

Similar to the confinement effects present in quantum wells, quantum dots have discrete energy levels associated with the effects of material band gap, size confinement, and the energy of the excitons present in the structure.[112] The confinement term can be calculated for an ideal, spherical QD surrounded by a matrix of finite potential V_0. The Bohr radius of this quasi-particle can be expressed as

$$a_B^* = \epsilon_r \left(\frac{m}{\mu}\right) a_B \tag{A.35}$$

with ϵ_r being the relative permitivity, μ the reduced mass of the system, and a_B is the Bohr radius. The confinement energy (which is added to the band gap) can be

expressed as

$$E_{conf} = \frac{\hbar^2\pi^2}{2a^2}\left(\frac{1}{m_e^*} + \frac{1}{m_h^*}\right) = \frac{\hbar^2\pi^2}{2\mu a^2} \tag{A.36}$$

Finally, the energy of the exciton generated inside a QD has energy of the form

$$-\frac{1}{\epsilon_r}\frac{\mu}{m_e}R_y = -R_y^* \tag{A.37}$$

which comes from the coulomb attraction between the electron and hole. In total, the energy of this ideal quantum dot can be expressed as

$$E_{QD} = E_g + \frac{\hbar^2\pi^2}{2\mu a^2} - R_y^* \tag{A.38}$$

A.3.2 Computational QD Energy Levels Calculation

To calculate the energy levels of our real QDs we use a different approach than that of an ideal sphere. The geometry of TSQDs grown on (111) oriented surfaces resembles more that of a pyramid with terraces and steps, and this geometry has much fewer symmetries as a consequence. We use a constantly refined model that deduces carrier confinement potentials U by adding the changes produced by strain to the QD and matrix heterostructures. We do this by taking the offset ratio from the difference between aboslute energy position of the average valence band and the ustrained bands.

By treaating the wetting layers of these materials as QWs, we can use the envelope function approximation to find the conduction band energy levels. The Schrödinger equation is enough to describe the behavior of electrons in the confuction band. However, the energy levels in the light and heavy hole bands requires a more sophisticated

approach, and we selected to use a 4×4 $k \cdot p$ Kohn-Luttinger hamiltonian, following preliminary work found in Ref. [92].

First we use a single-band constant potential Hamiltonian operator

$$H(r) = -\frac{\hbar^2}{2}\left(\nabla \frac{1}{m^*(r)} \nabla\right) + U(r) \tag{A.39}$$

In order to approximate the QD geometry more closely, a tetrahedron with a base in the shape of an equilateral triangle provides us with a close match. The dimensions we use for these models come from AFM scans (cf. **??**). The envelope function we use can then be expanded into a basis set made linear combination ($\psi(r)$ and ϕ, respectively). This is then applied to solutions to this "cuboidal" QD that has an infinite barrier height

$$\Psi(r) = \sum_{l,m,n} a_{l,m,n} \phi_{l,m,n}(r) \tag{A.40}$$

and the energy levels can be obtained from the matrix equation

$$\left(M_{l,m,n,l',m',n'} - E\delta_{l,l'}\delta_{m,m'}\delta_{n,n'}\right) a_{l,m,n} = 0 \tag{A.41}$$

where the orthonormality of the wavefunctions provides the Dirac delta factors. The matrix elements $M_{l,m,n,l',m',n'}$ are then

$$M_{l,m,n,l',m',n'} = \int \Psi^*_{l',m',n'} H(r) \Psi_{l,m,n} dr \tag{A.42}$$

$$= \left[\frac{\hbar^2 \pi^2}{2m_b^*}\left(\frac{l \cdot l'}{L_x^2} + \frac{m \cdot m'}{L_y^2} + \frac{n \cdot n'}{L_z^2}\right) + U\right] \delta_{l,l'}\delta_{m,m'}\delta_{n,n'} \tag{A.43}$$

$$+\frac{\hbar^2}{2}\left(\frac{1}{m_d^*} - \frac{1}{m_b^*}\right) \int_D \nabla \phi^*_{l',m',n'} \nabla \phi_{l,m,n} dr - U \int_D \phi^*_{l',m'n'} \phi_{l,m,n} dr \tag{A.44}$$

This matrix $M_{l,m,n,l',m',n'}$ can then be solved numerically using the Monte Carlo method.

A.4 Piezoelectric Tensor

Piezoelectricity is defined as the electric moment per unit volume, or the polarization charge per unit area. It is a component of the electrical displacement **D**.

$$\mathbf{D} = \epsilon_0 \mathbf{E} + \mathbf{P} \tag{A.45}$$

$$\tag{A.46}$$

and is defined as

$$\mathbf{P} = d\sigma \tag{A.47}$$

where **P** is the polarization, d is the piezoelectric modulus and σ is stress. We can think of polarization as the response of a material to an applied stress. In tensor notation, equation A.47 can be written as

$$P_i = d_{ijk}\sigma_{ij} \tag{A.48}$$

because each component of **P** is related to all the stress components σ_{ij}.

$$P_i = d_{ijk}\sigma_{jk} = \begin{cases} P_1 = d_{1jk}\sigma jk, \\ P_2 = d_{2jk}\sigma jk, \\ P_3 = d_{3jk}\sigma jk \end{cases}$$

for a total of 27 terms necessary to fully describe the polarization of a body. This is characteristic of third rank tensors. Considering the stress symmetry condition $\sigma_{ij} = \sigma_{ji}$[22] it follows that $d_{ijk} = d_{ikj}$. This reduces the amount of terms from 27 to 18, as we have $d_{112} = d_{121}$, reducing our three matrices in the following manner

$$\begin{Bmatrix} d_{i11} & d_{i12} & d_{i13} \\ d_{i21} & d_{i22} & d_{i23} \\ d_{i31} & d_{i32} & d_{i33} \end{Bmatrix} \rightarrow \begin{Bmatrix} d_{i11} & d_{i12} & d_{i13} \\ & d_{i22} & d_{i23} \\ & & d_{i33} \end{Bmatrix}$$

Writing the equation for P_i is now easier if we take the remaining six terms of each direction of P and put them in one row

$$d_{ij} = \begin{Bmatrix} d_{i11} & d_{i12} & d_{i13} \\ & d_{i22} & d_{i23} \\ & & d_{i33} \end{Bmatrix} = \begin{Bmatrix} d_{i11} & d_{i22} & d_{i33} & d_{i23} & d_{i13} & d_{i12} \end{Bmatrix}$$

and we can thus rewrite d_{ij} as

$$d_{ij} = \begin{Bmatrix} d_{11} & d_{12} & d_{13} & d_{14} & d_{15} & d_{16} \\ d_{21} & d_{22} & d_{23} & d_{24} & d_{25} & d_{26} \\ d_{31} & d_{32} & d_{33} & d_{34} & d_{35} & d_{36} \end{Bmatrix} \tag{A.49}$$

In order to further reduce the number of coefficients required to characterize the piezoelectricity of a material we look into the symmetries of its crystal structure. A crystal with a center of symmetry (i.e. a point from which all the elements can be inverted and the structure would remain unaltered) can begin feeling a stress and then undergo an inversion: the stress would remain the same yet its polarization should

change sign, but the crystal remains the same. The only value for which this is true is P=0. It follows that materials with centers of symmetry **are not piezoelectric**. The crystal structure for GaAs is represented by the group $F\bar{4}3m$. Part of the cubic family, it is defined by a 4-fold inversion axis, a 3-fold rotation axis and a mirror.
If we consider that one of its diad (2-fold) axis of symmetry is parallel to the x_3 direction, we can transform its piezoelectric modulus d_{123} by switching signs on the 1's and 2's. This means that coefficients that have only no 3's or two 3's will have to be transformed to their opposite sign $d_{211} = -d_{211}$ which necessarily means they are zero. Repeating this with the 3 diad axes of symmetry parallel to the cartesian axes leaves us with only 3 coefficients that are all equal: $d_{14} = d_{25} = d_{36}$

$$d_{ij} = \left\{ \begin{matrix} 0 & 0 & 0 & d_{14} & 0 & 0 \\ 0 & 0 & 0 & 0 & d_{14} = d_{25} & 0 \\ 0 & 0 & 0 & 0 & 0 & d_{14} = d_{36} \end{matrix} \right\}$$

indicating that the direction [110] is the piezoelectrically active direction in GaAs/AlGaAs.

A.5 Quantum Well Energy Calculation Code

For the work performed on chapter 3, and to give me and my collaborators a sense of where the luminescence from the TSQDs in chapter 6 would come, I wrote the following code to solve for the energies of confined states within a simple quantum well.

```
ClearAll;
```

```
planckconstantreduced = 6.582119514*^-16 ; (*h bar in eV s *)
mo = 9.10938188 10^-31;
echarge = 1.60218  10^-19(* C *);

MetodaTangente[x0_, eps_] := Block[{p0, p1, dp, k}, p0 = N[x0];
   p1 = p0;
   dp = 1;
   k = 0;
   While[dp > eps, p0 = p1;
    p1 = p0 - (funimpar[p0]/funimpar'[p0]);
    dp = Abs[p1 - p0];
    k = k + 1;];
   Print[p1];];

(* 300K *)
Upot = 0.3781 ; (*Difference in bandgaps of Al and GaAs*)
massAlGaAs1[
   x_] := (0.063 + 0.083 x ) mo; (*Effective mass of electrons*)
massAlGaAs = massAlGaAs1[0.3];
massGaAs = 0.063 mo; (*Effective mass of GaAs electrons*)
lwell = 5;

funimpar[z_] :=
  Sqrt[massAlGaAs/massGaAs] Tan[z] -
```

```
   Sqrt[(lwell/2 Sqrt[(2*massAlGaAs*Upot)/
      planckconstantreduced^2])^2 - z^2]/z;
funpar[z_] :=
  z/Sqrt[(lwell/2 Sqrt[(2*massAlGaAs*Upot)/
      planckconstantreduced^2])^2 - z^2] +
   Sqrt[(massAlGaAs/massGaAs)^-1] Tan[z];


(*For 5 nm well*)
MetodaTangente[0.65, 0.001]
Show[Plot[{funpar[z]}, {z, 0, 3}, PlotStyle -> Red,
  Exclusions -> True, AxesLabel -> {eV, Arb}],
 Plot[{funimpar[z]}, {z, 0, 3}, PlotStyle -> Blue ],
 Plot[{(funimpar[z]*funpar[z])}, {z, 0, 3}, PlotStyle -> Green,
  AxesLabel -> {eV, Arb}]]
(*For 7 nm well*)
lwell = 7
MetodaTangente[0.65, 0.001]
Show[Plot[{funpar[z]}, {z, 0, 3}, PlotStyle -> Red,
  AxesLabel -> {eV, Arb}],
 Plot[{funimpar[z]}, {z, 0, 3}, PlotStyle -> Blue] ,
 Plot[{(funimpar[z]*funpar[z])}, {z, 0, 3}, PlotStyle -> Green,
  AxesLabel -> {eV, Arb}]]
(*For 10 nm well*)
lwell = 10
```

```
MetodaTangente[0.8, 0.001]
Show[Plot[{funpar[z]}, {z, 0, 3}, PlotStyle -> Red,
  AxesLabel -> {eV, Arb}],
 Plot[{funimpar[z]}, {z, 0, 3}, PlotStyle -> Blue ],
 Plot[{(funimpar[z]*funpar[z])}, {z, 0, 3}, PlotStyle -> Green]]
```

A.6 XRD Simulation and Fitting Code

For work done for projects to which I contributed very little, I wrote a code to turn data from the Dynamical x-ray diffraction GID_SL tool from Argonne National Lab. [Source: GID_SL on the Web]

A.6.1 Code for XRD simulation

```
period=20
 t=20 code=InAs sigma=2 da/a=a
 t=30 code=InAs x=0.75 code2=InSb sigma=2 da/a=a
 end period

 t=450 code=AlAs x=0.11 code2=AlSb sigma=2 da/a=a

 period=600
 t=20 code=InAs sigma=2 da/a=a
 t=30 code=InAs x=0.75 code2=InSb sigma=2 da/a=a
 end period
```

A.6.2 Code for Scaling and Plotting Data

```
    ClearAll;
importdata1 = Import["G:\\InGaAs Paper\\nBn XRD\\simulation.dat"];
importdata2 = Import["G:\\InGaAs Paper\\nBn XRD\\M448scan.dat"];
importdata1[[All, 1]] = 2*importdata1[[All, 1]];
importdata1[[All, 2]] = 10000000*importdata1[[All, 2]];
ListLogPlot[{importdata1, importdata2}, Joined -> {True, False},
 Frame -> True,
 PlotStyle -> {{{Red}, PointSize[0.01]}, {{Blue}, PointSize[0.01],
    Opacity[0.5]}}, GridLines -> Automatic,
 FrameLabel -> {"2\[Theta] (degrees)", "Intensity (arb. units"},
 PlotLegends ->
  Placed[PointLegend[{"Simulation", "Data"},
    LegendFunction -> "Frame",
    LegendLayout -> "Column"], {{0.25, 0.8}, {1.7, 0.05}}],
 PlotRange -> {{55, 65.5}, Automatic}]
dataset1 = importdata1;
```